AEDC-TR-94-18

DRAKES

NEDANA,
A Three-Dimensional Thermochemical
Nonequilibrium Chimera-Based Flow Solver

S. G. Rock, R. W. Tramel, and S. L. Keeling
Micro Craft Technology/AEDC Operations

July 1995

Final Report for Period October 1990 — September 1994

**ARNOLD ENGINEERING DEVELOPMENT CENTER
ARNOLD AIR FORCE BASE, TENNESSEE
AIR FORCE MATERIEL COMMAND
UNITED STATES AIR FORCE**

This report has been reviewed by the Office of Public Affairs (PA) and is releasable to the National Technical Information Service (NTIS). At NTIS, it will be available to the general public, including foreign nations.

APPROVAL STATEMENT

This report has been reviewed and approved.

[signature]

KEVIN L. KILPATRICK, Capt, USAF
Flight Dynamics Technology
Applied Technology Division
Test Operations Directorate

Approved for publication:

FOR THE COMMANDER

[signature]

ROBERT T. CROOK
Asst Chief, Applied Technology Division
Test Operations Directorate

REPORT DOCUMENTATION PAGE

Form Approved
OMB No. 0704-0188
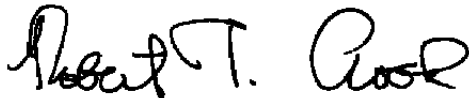
1. AGENCY USE ONLY (Leave blank)	2. REPORT DATE	3. REPORT TYPE AND DATES COVERED
	July 1995	Final - October 1990 - September 1994

4. TITLE AND SUBTITLE

NEDANA, A Three-Dimensional Thermochemical Nonequilibrium Chimera-Based Flow Solver

5. FUNDING NUMBERS

PN 0118

6. AUTHOR(S)

S. G. Rock, R. W. Tramel, and S.L. Keeling
Micro Craft Technology/AEDC Operations

7. PERFORMING ORGANIZATION NAME(S) AND ADDRESS(ES)

Arnold Engineering Development Center/DO
Air Force Materiel Command
Arnold Air Force Base, TN 37389-9010

8. PERFORMING ORGANIZATION (REPORT NUMBER)

AEDC-TR-94-18

9. SPONSORING/MONITORING AGENCY NAMES(S) AND ADDRESS(ES)

Arnold Engineering Development Center/DO
Air Force Materiel Command
Arnold Air Force Base, TN 37389-9010

10. SPONSORING/MONITORING AGENCY REPORT NUMBER

11. SUPPLEMENTARY NOTES

Available in Defense Technical Information Center (DTIC).

12A. DISTRIBUTION/AVAILABILITY STATEMENT

Approved for public release; distribution is unlimited.

12B. DISTRIBUTION CODE

13. ABSTRACT (Maximum 200 words)

A new three-dimensional nonequilibrium diagonal approximate Newton's algorithm (NEDANA) has been developed for flows with thermal and chemical nonequilibrium. Changing chemistry and thermal models is straightforward because the flow solver receives chemical, thermodynamic, and transport properties from the NEQPAK library of subroutines. The flow solver is developed in the chimera domain decomposition architecture in order to incorporate complex multiple-body configurations and moving grids. Excellent agreement was obtained in comparisons of the new flow solver with steady-state experimental data and solutions from existing state-of-the-art flow solvers.

14. SUBJECT TERMS

thermodynamic   flow solver

15. NUMBER OF PAGES

135

16. PRICE CODE

17. SECURITY CLASSIFICATION OF REPORT	18. SECURITY CLASSIFICATION OF THIS PAGE	19. SECURITY CLASSIFICATION OF ABSTRACT	20. LIMITATION OF ABSTRACT
UNCLASSIFIED	UNCLASSIFIED	UNCLASSIFIED	SAME AS REPORT

PREFACE

CONTENTS

ILLUSTRATIONS

<u>Figure</u>   <u>Page</u>

TABLES

APPENDICES

1.0 INTRODUCTION

1.1 GENERAL

This work is motivated by the need to understand high-speed continuum flow which occurs within the flight envelope of many of the vehicles of current interest, including single-stage-to-orbit vehicles, aero-assisted orbit-transfer vehicles, and particularly interceptor missiles. Personnel at the Arnold Engineering Development Center (AEDC) are now engaged in efforts to build/upgrade various test facilities to make them capable of testing the new generation of vehicle systems in the high velocity regime (Refs. 1–5). These facilities include the hypersonic tunnels, the ballistic ranges, and the arc heater tunnels. For example, the hypersonic tunnels can be used to perform jet interaction and staging studies for the interceptors. The ballistic ranges can be used for testing the lethality of these missiles. The arc heater tunnels can be used to test materials for interceptor nose tips. However, it is important to emphasize that these facilities will be used to generate conditions that only simulate flight conditions. In some cases there may be significant differences between the simulated and actual flight conditions. Flight testing can be used to obtain data that are free of the simulation errors but at great expense. On the other hand, computational simulations are not subject to the limitations specific to ground testing. Therefore, computations can be used together with ground testing to accurately capture the phenomena under investigation. Thus a synergistic, truly integrated combination of computations, ground testing, and flight testing is required for hypersonic systems development (Ref. 6).

To support this synergism, an effort has been initiated to develop the computational capability to simulate flows in the test facilities with high accuracy. Based on recent scaling studies, it is assumed that a flow solver which accurately predicts the fluid dynamics of the test cells can be used to extrapolate to free flight conditions with the same accuracy, provided valid physical models are available for the conditions of interest.

To establish the proper context for the present effort, note that the high-speed flows mentioned above are characterized by nonequilibrium thermochemical processes. Such effects are significant because the transition time for a fluid particle through a region of interest is shorter than the time required for particle-particle collisions to bring the gas into equilibrium. Therefore, the development of a flow solver to study these flows necessarily involves the modeling of thermo–chemical nonequilibrium. Furthermore, the geometric complexities inherent in the simulation of the flows around the vehicles mentioned require the use of domain decomposition techniques which have reached maturity in the chimera methodology (Ref. 7).

1.2 BACKGROUND

Computational fluid dynamics has matured to a stage where it is possible to compute transonic flow fields about complex three–dimensional bodies and bodies in relative motion (Refs. 8 and 9). However, there is a need to develop algorithms for complex three–dimensional bodies and bodies

7

in relative motion in hypersonic flow fields which require reasonable computational resources (Ref. 10). Some important features of a good computational algorithm are: (1) computational efficiency to minimize the arithmetic operation count and computer memory requirements, (2) adaptability to computational domains consisting of either blocked or non–structured grids, (3) fast convergence, (4) high accuracy which does not degrade readily because of a sensitivity to the choice of parameter settings, and (5) flexibility to allow transport equations (i.e., species, energy, or turbulence) to be added or deleted with minimal effort.

Solution algorithms can generally be categorized as either explicit or implicit methods. Explicit methods have low arithmetic operation counts because they do not require matrix inversions in their solution procedures. These methods are limited to small computational time steps for numerical stability. Hence, a large number of iterations is required for convergence to a steady–state solution. Implicit methods are stable for much larger computational time steps and generally require fewer iterations to converge. Unfortunately, implicit methods require matrix inversions, which are computationally intensive.

Recently, several investigators have proposed numerical algorithms which are globally explicit and locally implicit. These algorithms are called locally implicit methods (LIM) or point–implicit methods. Locally implicit algorithms have demonstrated the best features of both explicit and implicit algorithms. Reddy and Jacocks (Ref. 11) developed a two–dimensional, finite–volume, locally implicit scheme for solution of the Euler equations. The scheme uses a relaxation method based on a modification to the one-step Gauss–Seidel–Newton iteration and does not require the solution of any matrix equations. The scheme was applied to the two–dimensional Navier–Stokes equations by Nayani (Ref. 12) and Towne (Ref. 13). Reddy and Benek (Ref. 14) developed a three–dimensional thin–layer Navier–Stokes LIM algorithm which incorporates the chimera domain decomposition procedure developed by Benek et al. (Ref. 7). Hwang and Liu (Ref. 15) developed a two–dimensional finite–element LIM scheme. Tramel (Ref. 16) developed a stable shock–capturing locally implicit scheme using a modified one-step red/black Jacobi–Newton iteration. This procedure was extended to reacting flows by Tramel, et al. (Ref. 17), and applied to vibrationally relaxing flows in nozzles by Limbaugh et al. (Ref. 18). Bussing and Murman (Ref. 19) used a point–implicit treatment of the chemical source terms for compressible flow problems with finite–rate chemistry. Eberhardt and Imlay (Ref. 20) developed a diagonal treatment of the chemical source term Jacobian for the computation of nonequilibrium flow fields. Gnoffo (Ref. 21) developed a finite–volume, point–implicit relaxation algorithm for the Navier–Stokes equations, and extended this algorithm to flows with chemical and thermal nonequilibrium (Ref. 22).

1.3 OVERVIEW

In this report, a three–dimensional, time–accurate, locally implicit algorithm for the solution of compressible viscous flow problems with thermo–chemical nonequilibrium is described. The algorithm is known as the nonequilibrium diagonal approximate Newton's algorithm (NEDANA). The new scheme is designed for vectorization in all coordinate directions. The scheme incorporates

the chimera domain decomposition procedure. This allows the scheme to be applicable to both complex configurations as well as bodies in relative motion. The code also incorporates the AEDC–developed chemistry package NEQPAK (Ref. 23). NEQPAK provides the necessary chemical, thermodynamic, and transport properties that are required to simulate the flow of a gas in thermo–chemical nonequilibrium. The details of the thermo–physical models and the numerical method are presented in this report along with the results from a sequence of test problems.

2.0 MODELING EQUATIONS

2.1 CONSERVATION EQUATIONS

The NEDANA code solves the conservation equations which describe the motion of a compressible viscous fluid in thermo–chemical nonequilibrium (Refs. 23, 24, 25). A more general development of these equations is contained in Appendix A. These equations are one mass conservation equation for each of the ns chemical species present in the flow,

$$\frac{\partial \rho_s}{\partial t} + \frac{\partial(\rho_s u_j)}{\partial x_j} = -\frac{\partial(\rho_s u_{js}^d)}{\partial x_j} + \omega_s,$$ (1)

and three mass–averaged momentum equations, $(i = 1, 3)$,

$$\frac{\partial(\rho u_i)}{\partial t} + \frac{\partial(\rho u_i u_j + p\delta_{ij})}{\partial x_j} = -\frac{\partial \tau_{ij}}{\partial x_j},$$ (2)

and a total energy equation,

$$\frac{\partial E}{\partial t} + \frac{\partial((E+p)u_j)}{\partial x_j} = -\frac{\partial(u_i \tau_{ij})}{\partial x_j} - \frac{\partial q_j}{\partial x_j} - \frac{\partial}{\partial x_j}\sum_{s=1}^{ns} u_{js}^d \rho_s h_s,$$ (3)

where

$$E = E_I + \frac{1}{2}\rho u_i u_i,$$ (4)

and E_I is the internal energy of the mixture.

The above equations are applicable to any fluid for which a continuum description is appropriate. If the collision rate among the individual particles in the fluid is high enough to ensure

that the species internal degrees of freedom are in thermal equilibrium with the translational temperature of the fluid, then the above equation set, plus certain constituent relations described in Sec. 2.2, provides a complete description of the fluid. This equation set is referred to as a one-temperature model. However, if the internal degrees of freedom are not in thermal equilibrium, then additional conservation equations must be solved. In the present work, a two-temperature model is assumed. In this model, the distribution of the rotational degrees of freedom is assumed to be given by a Boltzmann distribution whose Boltzmann temperature is equal to the translational temperature of the fluid, while the vibrational/electronic excitation degrees of freedom are characterized by a separate Boltzmann temperature T_V (Ref. 26). This leads to the specification of an additional conservation equation for the vibrational–electronic energy, E_V. In the absence of ionization and radiation, this equation takes the form

$$\frac{\partial E_V}{\partial t} + \frac{\partial(E_V u_j)}{\partial x_j} = -\frac{\partial q_{V_j}}{\partial x_j} - \frac{\partial}{\partial x_j}\sum_{s=1}^{n_s} u_{j_s}^d \rho_s h_{V_s} + \omega_V. \tag{5}$$

In this case, the internal energy of the mixture, E_I, is the sum of a translational/rotational part, E_{tr}, and a vibrational/electronic portion, E_V, i. e.,

$$E_I = E_{tr} + E_V, \tag{6}$$

where

$$E_{tr} = \sum_{s=1}^{n_s} \rho_s e_{tr,s}. \tag{7}$$

and

$$E_V = \sum_{s=1}^{n_s} \rho_s e_{V,s}. \tag{8}$$

2.2 AEROTHERMAL MODELS

In order to completely specify the fluid being simulated, certain constituent relations are required: (1) the thermal equation of state of the gas, $p = p(\rho_s, \mathcal{M}_v, T)$; (2) the caloric equation of state for each species, $h_s = h_s(T, T_V) = e_s(T, T_V) + p_s/\rho_s$; (3) the shear stress tensor, τ_{ij}; (4) the conductive heat flux, q_j; (5) the diffusion velocity of species s, $u_{j_s}^d$; (6) the chemical source term of species s, ω_s; and (7) the vibrational/electronic energy source term, ω_V. NEQPAK is used to provide

10

these quantities. NEQPAK has the capability to apply many thermo–chemical models. Only those portions of NEQPAK relevant to the present work will be discussed below. In particular, if ionization was present while the gas was in a state of thermal nonequilibrium, then some of the formulas presented below would need to be modified. A detailed description of NEQPAK is found in Ref. 23.

The gas is assumed to be composed of a mixture of thermally perfect gases. The static pressure of the mixture is then the sum of the partial pressures of the constituent gases (Dalton's law of partial pressures),

$$p = \sum_{s=1}^{ns} p_s,\tag{9}$$

where

$$p_s = \rho_s R_s T,\tag{10}$$

and R_s is the species gas constant. The species gas constant is defined in terms of the universal gas constant, $\mathcal{R}$, and the species molecular weight, $\mathcal{M}_s$, by the relationship

$$R_s = \frac{\mathcal{R}}{\mathcal{M}_s}.\tag{11}$$

For a gas in thermal equilibrium, the specific enthalpy for each species, h_s, is given by

$$h_s = \int_0^T C_p^{s} dT' + h_s^0,\tag{12}$$

where C_p^S is obtained from curve fits based on a combination of experimental data and theoretical modeling, while h_S^0 is the heat of formation of species s at $0K$. These curve fits are of the form

$$\frac{C_p^{s}}{R_s} = a_{1,s} + a_{2,s}T + a_{3,s}T^2 + a_{4,s}T^3 + a_{5,s}T^4,\tag{13}$$

and the coefficients $a_{i,s}$ are taken from Ref. 27. For the two–temperature model, h_s is written as

$$h_s = h_{tr,s} + h_{V,s},\tag{14}$$

where

.

$$h_{tr,s} = \int_0^T C_{p,tr}^s dT' + h_s^0 = e_{tr,s} + \frac{p_s}{\rho_s}, \tag{15}$$

and

$$h_{V,s} = \int_0^{T_V} C_{p,V}^{'s} dT' = e_{V,s}. \tag{16}$$

Here $C_{p,tr}^s$ is the constant translational/rotational portion of the specific heat ($C_{p,tr}' = 3.5R_s$ for diatomic species and $2.5R_s$ for monatomic species). The vibrational/electronic portion of the specific heat is calculated according to the formula

$$C_{p,V}^{'s} = C_p^{'s}(T_V) - C_{p,tr}^{'s}. \tag{17}$$

Here, $C_p^{'s}(T_V)$ means that the curve fits in Eq. (13) are evaluated using T_V. The temperatures T and T_V are determined from E_{tr} and E_V.

The stress tensor with the Stokes hypothesis is expressed as

$$\tau_{ij} = -\mu(\frac{\partial u_i}{\partial x_j} + \frac{\partial u_j}{\partial x_i}) + \frac{2}{3}\mu\frac{\partial u_k}{\partial x_k}\delta_{ij}, \tag{18}$$

and the components of the heat flux vector are given by

$$q_j = -\kappa_{tr}\frac{\partial T}{\partial x_j} - \kappa_V\frac{\partial T_V}{\partial x_j}. \tag{19}$$

The individual species viscosities, μ_s, are calculated using the following curve fits (Ref. 27):

$$\mu_s = 0.1\exp(b_{5,s} + b_{4,s}\mathcal{T} + b_{3,s}\mathcal{T}^2 + b_{2,s}\mathcal{T}^3 + b_{1,s}\mathcal{T}^4), \tag{20}$$

where $\mathcal{T} = \ln T$. The species conductivities are related to the species viscosities by the relations (Ref. 27)

$$\kappa_{tr,s} = 3.75\mu_s R_s + \rho \mathcal{D}_{s,s} C_{p,r}^{'s}, \tag{21}$$

and

$$\kappa_{V,s} = \rho \mathcal{D}_{s,s} C_{p,V}^{'s}. \tag{22}$$

12

where the binary diffusion coefficient is given by the following curve fit:

$$\mathcal{D}_{s,r} = \frac{10.1325}{p} \exp(d_{4,s,r} + d_{3,s,r}T + d_{2,s,r}T^2 + d_{1,s,r}T^3).$$ (23)

The mixture viscosity and mixture conductivity are computed using the semi–empirical methods of Armaly and Sutton (Refs. 28, 29).

The species diffusion velocities, u_{js}^d, are given by Fick's law,

$$\chi_s u_{js}^d = -D_s \frac{\partial \chi_s}{\partial x_j}.$$ (24)

The above equation is only rigorously valid for cases in which the following conditions hold (Ref. 30): (1) the gas is a binary mixture; (2) the molecular weights of the species in the binary mixture are equal, or the pressure is constant; (3) thermal diffusion is negligible; and (4) the body forces per unit mass acting on each species are equal. If these conditions are not satisfied, then the rigorous computation of the diffusion velocities involves the solution of a matrix equation. However, the complexity of this process has lead to the concept of an effective binary diffusion coefficient, D_s, (Ref. 30) defined to be

$$D_s = \frac{1 - Y_s}{\sum_{n \neq s} \frac{\chi_n}{\mathcal{D}_{n,s}}},$$ (25)

where D_s is obtained by treating $ns - 1$ of the species as if they were present in trace amounts and diffusing through a background of a predominate species. Here, D_s is defined to be an average of the binary diffusion coefficients $\mathcal{D}_{s,r}$ where $\mathcal{D}_{s,r}$ is the diffusion coefficient obtained for a mixture composed of only species s and r (Ref. 31). Note that in order to strictly enforce mass conservation, the diffusion velocities of the predominate species would have to be obtained from the relationship $\sum_{s=1}^{ns} Y_s u_{js}^d = 0, j = 1, 2,$ or 3. However, this expression is not employed in the present code. The diffusion velocities for all species are computed using Eq. (24). This expression is a reasonable approximation provided that the molecular weights of the species do not vary widely, which is the case for air.

The species source terms, ω_s, and vibrational/electronic energy source term, ω_v, are also provided by NEQPAK. The species source terms are constructed as follows. Let the rth reaction involving species s be written in the form

13

$$\sum_{n=1}^{ns} \nu_{r,n} M_n \rightleftharpoons \sum_{m=1}^{ns} \nu'_{r,m} M_m,$$

(26)

in which M_s represents one mole of species s and the $\nu_{r,s}$ and $\nu'_{r,s}$ are the stoichiometric coefficients. The rate of disappearance of a species s due to the rth reaction is

$$\mathcal{L}_{r,s} = \nu'_{r,s} k_r^r \prod_{n=1}^{ns} \gamma_n^{\nu'_{r,n}} + \nu_{r,s} k_r^f \prod_{n=1}^{ns} \gamma_n^{\nu_{r,n}},$$

(27)

while the production rate of a species s due to the rth reaction is

$$\mathcal{G}_{r,s} = \nu'_{r,s} k_r^f \prod_{m=1}^{ns} \gamma_m^{\nu_{r,m}} + \nu_{r,s} k_r^r \prod_{m=1}^{ns} \gamma_m^{\nu'_{r,m}}.$$

(28)

The net rate of change of species s due to all reactions is

$$\omega_s = \mathcal{M}_s \sum_{r=1}^{nr} (\mathcal{G}_{r,s} - \mathcal{L}_{r,s}),$$

(29)

where nr is the number of reactions. Like most aerothermochemical models, NEQPAK assumes the modified Arrhenius form (Ref. 32) for chemical reaction rates

$$k_r^f = A_r T^{B_r} exp(-C_r/T),$$

(30)

where T is the translational temperature of the gas. The rates defined in Eq. (30) were obtained from fits to experimental data that were collected under conditions of thermal equilibrium. However, when the reaction rate under question represents, for instance, a two-body dissociation reaction, then the reaction rate also depends on the vibrational temperature of the gas. One of the more popular approaches used to account for thermal nonequilibrium is that of Park (Ref. 33), who replaced the translational temperature in Eq. (30) with a generic temperature or average temperature, T_q. Park defined T_q by the relation

$$T_q = T_V^\alpha T^{1-\alpha}; 0 < \alpha < 1,$$

(31)

where α was chosen to reproduce experimental data.

14

The reverse reaction rate coefficient k_r^r is related to the forward rate by

$$k_r^r = k_r^f / K_r^c, \tag{32}$$

where

$$K_r^c = (p_{atm}/\mathcal{R}T)^{\delta_r} exp(-\frac{\Delta F}{\mathcal{R}T}), \tag{33}$$

is the equilibrium constant for the rth reaction and

$$\delta_r \equiv \sum_{s=1}^{n_s}(\nu_{r,s}' - \nu_{r,s});$$

$$\Delta F \equiv \sum_{s=1}^{n_s}(\nu_{r,s}' - \nu_{r,s})G_s^0. \tag{34}$$

In Eq. (33), $p_{atm} = 1.01325 \times 10^5$ Pa. Also G_S^0 is the Gibbs free energy for species s at the given temperature and a pressure of 1 atm. The Gibbs free energies are computed from curve fits taken from Ref. 27.

The vibrational source term, ω_v, is the sum of two terms. The first term, ω_V^{v-T}, models the relaxation of vibrational energy under collisions with heavy particles while the second term, ω_V^{v-c}, deals with the addition or removal of energy from the vibrational/electronic energy pool due to chemical reactions. The vibration–translation interaction is modeled according to the theory developed by Landau and Teller (Ref. 34). Landau and Teller showed that if the vibrational energy levels of a molecule are equally spaced (harmonic oscillator approximation) and only single–level transitions are allowed, then

$$\omega_V^{v-T} = \sum_{s=1}^{n_s} \rho_s \frac{(c_{v,s}^* - c_{v,s})}{\tau_s} \tag{35}$$

where the $e_{v,s}^*$ indicates the equilibrium value of the vibrational energy, and τ_s is the vibrational energy relaxation time. Here, $e_{v,s}$ represents the vibrational energy of the molecule rather than the vibrational/electronic energy. Strictly speaking, Eq. (35) was derived for a harmonic oscillator, but it is applied to anharmonic oscillators by using the polynomial curve fits defined in Eqs. (13) and (16) to calculate the vibrational energy as follows. First, the electronic excitation energy $e_{e,s}$ is computed from the formula

$$e_{e,s} = \mathcal{M}_s \frac{1}{Z} \sum_{l=1}^{n_{el}} \psi_l \exp(-\psi_l), \tag{36}$$

where $\Psi_l \equiv \varepsilon_l / k\, T_V$, and the electronic partition function is

$$Z \equiv \sum_{l=1}^{nel} g_l \exp(-\psi_l),\tag{37}$$

where nel is the number of electronic energy levels for species s; g_l is the degeneracy of the lth electronic level, and ε_l is its energy. $e_{v,s}$ is set equal to the difference of $e_{V,s}$ and $e_{e,s}$.

The relaxation time $\tau_{s,r}$ of species s in a bath of species r is calculated using the empirical correlations of Millikan and White (Ref. 35), where $\tau_{s,r}$ is defined to be

$$p\tau_{s,r} = \exp[A_{s,r} T^{-1/3} - 0.015 A_{s,r}\mu_{s,r}^{1/4} - 18.42],\tag{38}$$

where

$$A_{s,r} = 0.00116\mu_{s,r}^{1/2}\theta_s^{4/3};\tag{39}$$

p is the pressure in atmospheres, and $\mu_{s,r}$ is the reduced mass of the interacting molecules s and r. In Eq. (39), $\theta_s = h\nu_s/k$, where ν_s is the characteristic vibrational frequency of species s; h is the Planck constant, and k is the Boltzmann constant. The relaxation time employed in Eq. (35) is computed from the $\tau_{s,r}$ according to the formula

$$\tau_s = \sum_{r=1}^{ns} \chi_r \tau_{s,r} + \tau_s^P \tag{40}$$

where

$$\tau_s^P = C\sqrt{\frac{M_s}{T}}\frac{1}{\gamma_s}\tag{41}$$

is Park's high-temperature correction (Ref. 36) and

$$C = (\sigma_s N_A \sqrt{8\mathcal{R}/\pi})^{-1} = 2.898677 \times 10^{-7}$$

in SI units. The value $\sigma_s = 10^{-20}\,m^2$ for the effective cross section for vibrational relaxation is that suggested by Gnoffo et al. (Ref. 26). The second term in ω_V models the effect that chemical reactions have on the vibrational energy. Clearly, the dissociation of a molecule removes vibrational/electronic energy, while recombination of a molecule must add vibrational/electronic

16

energy to the species pool. In this work it is assumed that nonpreferential dissociation occurs. Under this assumption, ω_V^{v-c} takes the form

$$\omega_V^{v-c} = \sum_{s=1}^{ns} \omega_s e_{V,s}. \tag{42}$$

3.0 NUMERICAL FORMULATION

3.1 THREE-DIMENSIONAL FINITE-VOLUME FORMULATION

The following derivation is for the two–temperature model. However, the equations and numerical method are easily reduced to the one–temperature model. The integral formulation of a system of conservation equations over a finite region of space takes the general form (Ref. 37)

$$\frac{\partial}{\partial t} \iiint_V Q \, dV + \iint_S \vec{\mathcal{F}} \cdot d\vec{S} = \iiint_V \Omega \, dV, \tag{43}$$

where for flows in thermo-chemical nonequilibrium

$$Q = \begin{pmatrix} \rho_1 \\ \vdots \\ \rho_{ns} \\ E_V \\ \rho u \\ \rho v \\ \rho w \\ E \end{pmatrix} \quad ; \quad \Omega = \begin{pmatrix} \omega_1 \\ \vdots \\ \omega_{ns} \\ \omega_V \\ 0 \\ 0 \\ 0 \\ 0 \end{pmatrix} \quad ; \tag{44}$$

and the numerical flux vector is written as the sum of inviscid and viscous contributions;

$$\begin{aligned}
\vec{\mathcal{F}} &= \vec{\mathcal{F}}_I + \vec{\mathcal{F}}_v \\
&= (F_I + F_v)\hat{i}_x + (G_I + G_v)\hat{i}_y + (H_I + H_v)\hat{i}_z. \tag{45}
\end{aligned}$$

Q and Ω are the vectors of conserved quantities and source terms, respectively. F, G, and H are the inviscid flux vectors. They are equal to the flux of Q per unit area per unit time in the Cartesian coordinates x, y, and z, respectively, with unit vectors $\hat{i}_x$, $\hat{i}_y$, and $\hat{i}_z$. For the present, we will ignore the viscous flux vectors F_v, G_v, and H_v. The inviscid flux vectors may be written as

$$F_1 = \begin{pmatrix} \rho_1\,u \\ \vdots \\ \rho_{ns}\,u \\ E_V\,u \\ \rho u^2 + p \\ \rho v u \\ \rho w u \\ (E+p)\,u \end{pmatrix} \quad ; \quad G_1 = \begin{pmatrix} \rho_1\,v \\ \vdots \\ \rho_{ns}\,v \\ E_V\,v \\ \rho u v \\ \rho v^2 + p \\ \rho w v \\ (E+p)\,v \end{pmatrix} \quad ; \quad H_1 = \begin{pmatrix} \rho_1\,w \\ \vdots \\ \rho_{ns}\,w \\ E_V\,w \\ \rho u w \\ \rho v w \\ \rho w^2 + p \\ (E+p)\,w \end{pmatrix}. \tag{46}$$

In order to solve Eq. (43) numerically, the spatial domain of interest is broken into a set of disjoint control cells with volumes, V, and cell face areas, $\vec{\sigma}_i$. The flux into or out of a finite-cell volume, V, across a cell face $\vec{\sigma}_i$ is obtained by $\vec{F} \bullet \vec{\sigma}_i$. The equations are written in terms of the fluxes in the computational directions F, G, and H. These directions correspond to the integer indices j, k, and l.

An implicit finite–volume discretization of Eq. (43) is

$$V_{J,K,L}\frac{(Q_{J,K,L}^{n+1} - Q_{J,K,L}^{n})}{\Delta t}$$
$$+ \ (\tilde{F}_{j+1,K,L}^{n+1} - \tilde{F}_{j,K,L}^{n+1}) + (\tilde{G}_{J,k+1,L}^{n+1} - \tilde{G}_{J,k,L}^{n+1}) + (\tilde{H}_{J,K,l+1}^{n+1} - \tilde{H}_{J,K,l}^{n+1}) \tag{47}$$
$$= \ V_{J,K,L}\,\Omega_{J,K,L}^{n+1}.$$

Throughout this report, the notation of Gnoffo (Ref. 21) has been adopted where capital letters J, K, L indicate cell centers and j, k, l indicate cell faces. Also, unlike most finite–volume schemes, NEDANA stores the conserved quantities at the cell vertices. The difference between this technique and traditional finite-volume techniques is largely transparent (see Appendix B). Storing the conserved variables directly at mesh points allows for interaction with finite–difference algorithms without altering the computational grids or data.

The numerical flux function is based on the flux-limited, artificial dissipation model of Jameson (Ref. 38), and Yoon and Kwak (Ref. 39). This model combines the simplicity of artificial dissipation schemes with the total variation diminishing, (TVD), property. A discussion of the relevant numerical issues involved in the selection of this particular flux model, as well as a complete description of the numerical flux function, is included in Appendix C. The flux at the cell face $j + 1$ is calculated as the average of the fluxes from cell J and $J + 1$. This averaging requires the flux function to be evaluated twice and then averaged. An alternative approach would be to average the conserved variables to obtain values at the cell face and then perform the flux evaluation. The

18

former method was chosen for its flexibility in writing finite–difference-type schemes. The numerical flux in the ξ direction at the $j + 1$ face has the form

$$
\begin{aligned}
\tilde{F}^{n+1}_{1j+1,K,L} &= \frac{1}{2}(\vec{F}^{n+1}_{1J+1,K,L} + \vec{F}^{n+1}_{1J,K,L}) \cdot \vec{\sigma}_{\xi j+1,K,L} \\
&+ c_{\xi j+1,K,L}(\bar{\bar{\Psi}}(\Delta_\xi Q^{n+1}_{J+1,K,L}, \Delta_\xi Q^{n+1}_{J,K,L}) \\
&- 2.0\Delta_\xi Q^{n+1}_{J,K,L} \\
&+ \bar{\bar{\Psi}}(\Delta_\xi Q^{n+1}_{J,K,L}, \Delta_\xi Q^{n+1}_{J-1,K,L}))
\end{aligned}
\tag{48}
$$

where the cell face directed area is defined as

$$
\vec{\sigma}_\xi = \sigma^x_\xi \hat{\imath}_x + \sigma^y_\xi \hat{\imath}_y + \sigma^z_\xi \hat{\imath}_z,
\tag{49}
$$

and

$$
\Delta_\xi Q^{n+1}_{J,K,L} = Q^{n+1}_{J+1,K,L} - Q^{n+1}_{J,K,L}.
\tag{50}
$$

Here, $\bar{\bar{\Psi}}$ is defined for vectors P and Q to have components:

$$
\Psi_i(P,Q) = \tfrac{1}{2}[\text{sign}(P_i) + \text{sign}(Q_i)]\min(|P_i|,|Q_i|).
\tag{51}
$$

The scalar dissipation coefficient is defined by

$$
c_{\xi j+1,K,L} = 0.25[\lambda_{\xi J+1,K,L} + \lambda_{\xi J,K,L}][\kappa_2 + \kappa_4 \mu_{\xi J,K,L}],
\tag{52}
$$

and the spectral radius of the flux Jacobian is defined at the cell center by

$$
\lambda_{\xi J,K,L} = \left| \vec{u} \cdot \overline{\vec{\sigma}_\xi} \right|_{J,K,L} + a_{J,K,L} \left\| \overline{\vec{\sigma}_\xi} \right\|_{J,K,L},
\tag{53}
$$

and the cell area in the ξ direction evaluated at the cell center is

$$
\overline{\vec{\sigma}_\xi}_{J,K,L} = \frac{1}{2}(\vec{\sigma}_{\xi j+1,K,L} + \vec{\sigma}_{\xi j,K,L}).
\tag{54}
$$

The frozen speed of sound is defined as

$$
a^2 = \gamma_f \frac{p}{\rho}
\tag{55}
$$

19

where the frozen ratio of specific heats is expressed as

$$\gamma_f = (1 + \beta), \tag{56}$$

where $\beta = \partial p / \partial E$ (see Appendix D).

The dissipation is a function of the pressure sensor

$$\mu_{\xi\,J,K,L} = \max(\nu_{\xi\,J,K,L}, \nu_{\xi\,J-1,K,L}), \tag{57}$$

where

$$\nu_{\xi\,J,K,L} = \left| \frac{p_{J+1,K,L} - 2.0\,p_{J,K,L} + p_{J-1,K,L}}{p_{J+1,K,L} + 2.0\,p_{J,K,L} + p_{J-1,K,L}} \right|. \tag{58}$$

The numerical fluxes $\tilde{G}$, and $\tilde{H}$ are calculated similarly.

3.2 QUASI-ONE-DIMENSIONAL FORMULATION

The one-dimensional form of the conservation equations with area change is derived in Appendix E. This form of the equations is solved when performing numerical studies for shock tube and nozzle problems. The finite-difference form of the equations is presented below:

$$\left(AJ^{-1} \begin{bmatrix} \rho_1 \\ \vdots \\ \rho_{ns} \\ E_V \\ \rho u \\ E \end{bmatrix} \right)_t + \left(AJ^{-1} \begin{bmatrix} \rho_1 u\xi_x \\ \vdots \\ \rho_{ns} u\xi_x \\ E_V u\xi_x \\ (\rho u\, u + p)\xi_x \\ (E + p)u\xi_x \end{bmatrix} \right)_\xi = \begin{bmatrix} AJ^{-1}\omega_1 \\ \vdots \\ AJ^{-1}\omega_{ns} \\ AJ^{-1}\omega_V \\ A_x J^{-1}p \\ 0 \end{bmatrix}. \tag{59}$$

Note that the equation has been transformed to curvilinear coordinates. The Jacobian of the transformation $x \to \xi$ is $J = \partial\xi/\partial x$. For constant area problems such as shock tubes, A is set equal to 1.

3.3 VISCOUS TERMS

In this section the viscous contributions to the flux function will be discussed. These contributions include shear stress, heat conduction, and diffusion terms. The viscous Cartesian flux function for the x direction from Eq. (45) has the form

$$
F_v = \begin{pmatrix} \rho_1 \, u_1^d \\ \vdots \\ \rho_{ns} \, u_{ns}^d \\ \sum_{s=1}^{ns} \rho_s h v_s \, u_s^d \, + \, q v_x \\ \tau_{xx} \\ \tau_{xy} \\ \tau_{xz} \\ \sum_{s=1}^{ns} \rho_s h_s \, u_s^d \, + \, q_x \, + \, q v_x \\ + \, \tau_{xx} u \, + \, \tau_{xy} v \, + \, \tau_{xz} w \end{pmatrix}.
$$

(60)

Each component of Eq. (60) may be formulated in the context of a finite–volume scheme. A thin–layer approximation also is employed in the direction normal to the body surface, ζ. Recalling that $\vec{F} = \vec{F}_I + \vec{F}_v$, the viscous flux contribution for species continuity becomes,

$$
\left\{ \left(\vec{F}_v \right)_{J,K,l} \cdot \left(\vec{\sigma}_\zeta \right)_{J,K,l} \right\}_s = \left(\frac{-\rho_s D_s}{\chi_s} \right)_{J,K,l} \left(\frac{\partial \chi_s}{\partial \zeta} \right)_{J,K,l} \left(\vec{\sigma}_\zeta \cdot \vec{\nabla}\zeta \right)_{J,K,l},
$$

(61)

where

$$
\left(\frac{-\rho_s D_s}{\chi_s} \right)_{J,K,l} = \frac{1}{2} \left[\left(\frac{-\rho_s D_s}{\chi_s} \right)_{J,K,L-1} + \left(\frac{-\rho_s D_s}{\chi_s} \right)_{J,K,L} \right].
$$

(62)

The viscous flux contribution to the vibrational—electronic energy equation can be expressed as

$$
\left\{ \left(\vec{F}_v \right)_{J,K,l} \cdot \left(\vec{\sigma}_\zeta \right)_{J,K,l} \right\}_{ns+1} = \left(\vec{\sigma}_\zeta \cdot \vec{\nabla}\zeta \right)_{J,K,l} \left[q v_\zeta + \sum_{s=1}^{ns} \rho_s h_V^s \, \frac{-D_s}{\chi_s} \frac{\partial \chi_s}{\partial \zeta} \right]_{J,K,l},
$$

(63)

where

$$
q v_\zeta = - \left(\kappa_V \frac{\partial T_V}{\partial \zeta} \right)_{J,K,l}.
$$

(64)

The viscous flux contribution to the x–momentum equation in finite–volume form can be written as

$$
\left\{ \left(\vec{F}_v \right)_{J,K,l} \cdot \left(\vec{\sigma}_\zeta \right)_{J,K,l} \right\}_{ns+2} = -\mu \left[\frac{\partial u}{\partial \zeta} \vec{\sigma}_\zeta \cdot \vec{\nabla}\zeta + \frac{1}{3} \frac{\partial \vec{u}}{\partial \zeta} \cdot \vec{\sigma}_\zeta \zeta_x \right]_{J,K,l}.
$$

(65)

21

In a similar manner, the viscous flux contribution for all of the momentum equations can be written compactly as

$$\left\{ \left(\vec{\mathcal{F}}_v\right)_{J,K,l} \cdot (\vec{\sigma}_\zeta)_{J,K,l} \right\}_{ns+2, ns+3, ns+4} = - \begin{pmatrix} \mu B_1 \frac{\partial u}{\partial \zeta} & + & \mu B_2 \zeta_x \\ \mu B_1 \frac{\partial v}{\partial \zeta} & + & \mu B_2 \zeta_y \\ \mu B_1 \frac{\partial w}{\partial \zeta} & + & \mu B_2 \zeta_z \end{pmatrix}_{J,K,l}, \tag{66}$$

where

$$B_1 = \vec{\sigma}_\zeta \cdot \vec{\nabla}\zeta \tag{67}$$

and

$$B_2 = \frac{1}{3}\left[\frac{\partial u}{\partial \zeta}\sigma_\zeta^x + \frac{\partial v}{\partial \zeta}\sigma_\zeta^y + \frac{\partial w}{\partial \zeta}\sigma_\zeta^z\right]. \tag{68}$$

The viscous flux contribution to the total energy equation now can be easily written using the previously developed expressions. The equation becomes

$$\left\{ \left(\vec{\mathcal{F}}_v\right)_{J,K,l} \cdot (\vec{\sigma}_\zeta)_{J,K,l} \right\}_{ns+5} = \left(\vec{\sigma}_\zeta \cdot \vec{\nabla}\zeta\right)_{J,K,l} \left[q_{tr\zeta} + q_{V\zeta} + \sum_{s=1}^{ns} \rho_s h_s \frac{-D_s}{\chi_s}\frac{\partial \chi_s}{\partial \zeta} \right]_{J,K,l}$$

$$- \mu \left[B_1 \left(u\frac{\partial u}{\partial \zeta} + v\frac{\partial v}{\partial \zeta} + w\frac{\partial w}{\partial \zeta} \right) \right]_{J,K,L}$$

$$+ \mu \left[B_2 \left(u\zeta_x + v\zeta_y + w\zeta_z \right) \right]_{J,K,l}. \tag{69}$$

where

$$q_{tr\zeta} = -\left(\kappa_{tr}\frac{\partial T_{tr}}{\partial \zeta}\right)_{J,K,l}$$

$$q_{V\zeta} = -\left(\kappa_V\frac{\partial T_V}{\partial \zeta}\right)_{J,K,l}. \tag{70}$$

3.4 CHIMERA DOMAIN DECOMPOSITION

NEDANA has incorporated the chimera domain decomposition procedure developed by Benek, Steger, and their co–workers (Refs. 7, 40–43). The chimera scheme was developed to allow a system of simple grids with simple topologies to model complex aerodynamic configurations or bodies in relative motion.

The general concept behind chimera is illustrated in Fig. 1, which depicts two independently generated meshes representing a flapped airfoil. The flap mesh is embedded within the airfoil mesh. Clearly, the flap mesh outer boundary can receive flow–field information interpolated from appropriate mesh points of the airfoil mesh. However, a reverse process must occur as well; the airfoil mesh must receive flow–field information from the flap mesh. This transfer is achieved as

22

follows. A hole must be created within the airfoil mesh to remove the points within the airfoil mesh that are interior to the flap. The hole boundary points of the airfoil mesh can be updated by interpolation from the flap mesh. In general, any mesh can receive information from other meshes through both outer boundary and hole boundary points.
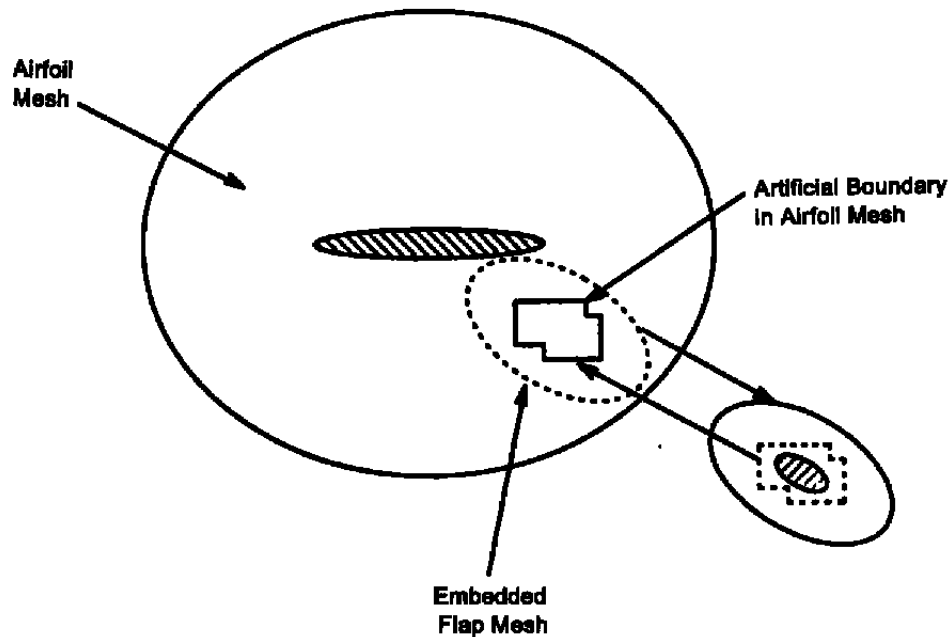
Figure 1. Mesh-to-mesh communication.

The interpolation process is further illustrated in Fig. 2, which depicts a portion of the overlap region between the airfoil and flap meshes. Airfoil mesh points inside the hole region surrounding the flap are blanked out of the computational domain of the airfoil mesh. In chimera terminology they are hole points. The hole region is defined by a hole creation boundary within the flap mesh. The points in the airfoil mesh surrounding the blanked points are hole boundary points, and they receive flow–field information interpolated from mesh points within the flap mesh. Correspondingly, points on the the outer boundary of the flap mesh receive flow–field information interpolated from mesh points within the airfoil mesh.

Application of the chimera scheme requires two steps: (1) a description of how each mesh is to communicate flow–field information to other meshes, and (2) execution of the flow solver (in this case, NEDANA) using the information generated in step 1. Step 1 is performed by PEGSUS (Ref. 44) developed at the AEDC. The processes accomplished by PEGSUS include establishing which boundary points in a mesh will be updated by interpolated flow variables from other meshes. Also, PEGSUS calculates the required interpolation coefficients for donor mesh points that provide interpolated information for recipient boundary points in another mesh. More information on the chimera scheme and the PEGSUS code can be found in the references.
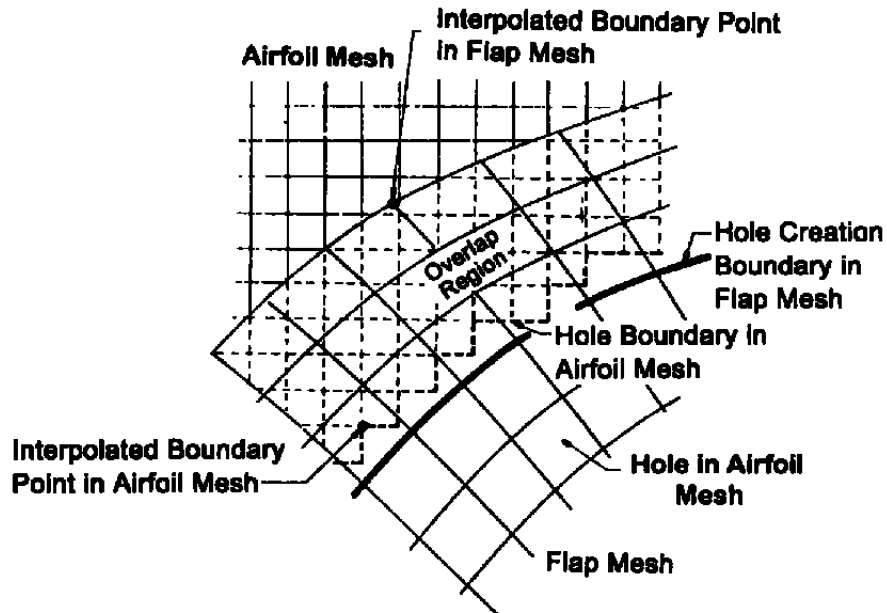
Figure 2. Overlap region between meshes.

3.5 SOLUTION PROCEDURE

Equation (47) is a set of nonlinear algebraic equations which is solved at each time step. A variety of techniques exists to solve such equations. An encyclopedic review of such techniques may be found in Ref. 45. Throughout this section, the nomenclature of Ref. 45 is used.

Newton's method is the classical procedure for solving nonlinear algebraic equations. For this, first define the residual vector, $R^n(Q)$, at time level n, as a function of a vector, Q, so that at a point J, K, L, R^n has components

$$
\begin{aligned}
R^n_{J,K,L}(Q) \;=\; & V_{J,K,L} \frac{(Q_{J,K,L} - Q^n_{J,K,L})}{\Delta t} \\
& + (\tilde{F}_{J+1,K,L}(Q) - \tilde{F}_{J,K,L}(Q)) \\
& + (\tilde{G}_{J,k+1,L}(Q) - \tilde{G}_{J,k,L}(Q)) \\
& + (\tilde{H}_{J,K,l+1}(Q) - \tilde{H}_{J,K,l}(Q)) \\
& - V_{J,K,L}\, \Omega_{J,K,L}(Q).
\end{aligned}
$$

The solution to Eq. (47) at time level $n + 1$ is the vector, Q^{n+1} that satisfies the residual equation,

$$
R^n(Q^{n+1}) = 0. \tag{71}
$$

24

An approximate Newton's method is used to solve this equation iteratively. The initial iteration is always Q^n, and after a sufficient number of iterations, Q^{n+1} is set equal to the last iteration. To simplify notation in the following, the dependence on n is suppressed. Let $Q^{(m)}$ denote the mth iterative approximation to the solution of Eq. (71). Also, let $R^{(m)}$ denote the residual vector evaluated at $Q^{(m)}$. Similarly, let the evaluation of the fluxes and the sources at $Q^{(m)}$ be denoted by the superscript, (m).

To motivate the development of the iterative techniques used in the NEDANA code, consider the use of a pure Newton's method approach to solving Eq. (71). First, the following linear system of equations is solved:

$$\left[\frac{\partial R^{(m)}}{\partial Q^{(m)}} \right] (Q^{(m+1)} - Q^{(m)}) = -R^{(m)}, \tag{72}$$

or

$$Q^{(m+1)} = Q^{(m)} - \left[\frac{\partial R^{(m)}}{\partial Q^{(m)}} \right]^{-1} R^{(m)}. \tag{73}$$

Next, the norm, $\|Q^{(m+1)} - Q^{(m)}\|$, is checked to see if it is less than some prescribed tolerance. If it is, then $Q^{(m)}$ is accepted as the solution to Eq. (47) at time level $n + 1$. If $\|Q^{(m+1)} - Q^{(m)}\|$ is greater than the prescribed tolerance, then m is incremented and Eq. (73) is solved again. This process is repeated until the norm is less than the prescribed tolerance or until a fixed number of iterations has been performed. When solving problems in two and three dimensions, Newton's method is computationally intensive since the Jacobian, $\partial R^{(m)}/\partial Q^{(m)}$, is a very large, sparse matrix. This makes direct inversion of the Jacobian impractical. Therefore, as described in detail below, the NEDANA code uses an alternative to Newton's method to solve Eq. (71). This method is referred to as a modified one-step, odd/even, Jacobi-Gauss-Seidel-Newton (JGSN) scheme. In the past, this iterative method was known as a variant of the LIM scheme.

To motivate the use of the JGSN method, first examine the Gauss-Seidel-Newton (GSN) and the Jacobi-Newton (JN) schemes. If a one-step GSN iteration were employed to solve Eq. (71), a Gauss-Seidel method would be applied as a primary iteration and Newton's method would be applied as a secondary iteration. Specifically, in the primary Gauss-Seidel iteration, for every grid point, J, K, L, the local residual equation,

$$R_{J,K,L}(..., Q^{(m^*)}_{J,K,L-1}, Q^{(m+1)}_{J,K,L}, Q^{(m^*)}_{J+1,K,L}, ...) = 0, \tag{74}$$

is solved for $Q^{(m+1)}_{J,K,L}$. Here, m^* indicates that the components of $Q^{(m+1)}$ are used in Eq. (74) if they are available, and otherwise, the components of $Q^{(m)}$ are used. Then, in the secondary iteration, Newton's method is used to solve Eq. (74) according to

$$Q^{(m+1)}_{J,K,L} = Q^{(m)}_{J,K,L} - \left[\frac{\partial R^{(m^*)}_{J,K,L}}{\partial Q^{(m)}_{J,K,L}}\right]^{-1} R^{(m^*)}_{J,K,L}. \tag{75}$$

In a one-step version of this scheme, only one iteration of Eq. (75) is implemented before proceeding to the next grid location. When all components of $Q^{(m+1)}$ are calculated, a sweep is said to be completed.

If a one-step JN iteration were employed to solve Eq. (71), a Jacobi method would be applied as a primary iteration and Newton's method would be applied as a secondary iteration. Specifically, in the primary Jacobi iteration, for every grid point, J, K, L, the local residual equation,

$$R_{J,K,L}(...,Q^{(m)}_{J,K,L-1}, Q^{(m+1)}_{J,K,L}, Q^{(m)}_{J+1,K,L}, ...) = 0, \tag{76}$$

is solved for $Q^{(m+1)}_{J,K,L}$. Note that here the fixed arguments of the local residual are written only in terms of the components of $Q^{(m)}$. Then, in the secondary iteration, Newton's method is used to solve Eq. (76) according to

$$Q^{(m+1)}_{J,K,L} = Q^{(m)}_{J,K,L} - \left[\frac{\partial R^{(m)}_{J,K,L}}{\partial Q^{(m)}_{J,K,L}}\right]^{-1} R^{(m)}_{J,K,L}. \tag{77}$$

Both methods described above involve only the inversion of an $nq \times nq$ matrix, where nq is the number of conserved variables. However, the GSN method is recursive and is not well suited for implementation on machines that employ vector processors (Ref. 46). In addition, Tramel (Ref. 16) has shown that a JN iteration is unstable for CFL numbers greater than one. Therefore, an odd/even JN iteration is proposed in Ref. 16 and is the basis for the solution technique used in NEDANA.

In NEDANA, an odd/even JN iteration is applied along lines of constant J, K, while a GSN iteration is applied in the other computational directions. As indicated above, this procedure is referred to as a Jacobi-Gauss-Seidel-Newton (JGSN) method. The odd/even JGSN iteration is implemented in NEDANA as follows. First, the following equation is solved for every point along a line of constant J, K, with $L = L_e$, an even value,

$$Q_{J,K,L_e}^{(m+1)} = Q_{J,K,L_e}^{(m)} - \left[\frac{\partial \mathbf{R}_{J,K,L_e}^{(0)}}{\partial Q_{J,K,L_e}^{(0)}}\right]^{-1} \mathbf{R}_{J,K,L_e}^{(m^*),e}. \tag{78}$$

Here,

$$
\begin{aligned}
\mathbf{R}_{J,K,L_e}^{(m^*),e} &= (\tilde{F}_{J+1,K,L_e}^{(m^*)} - \tilde{F}_{J,K,L_e}^{(m^*)}) \\
&+ (\tilde{G}_{J,k+1,L_e}^{(m^*)} - \tilde{G}_{J,k,L_e}^{(m^*)}) \\
&+ (\tilde{H}_{J,K,L_e+1}^{(m),e} - \tilde{H}_{J,K,L_e}^{(m),e}) \\
&+ V_{J,K,L_e} \frac{(Q_{J,K,L_e}^{(m)} - Q_{J,K,L_e}^{n})}{\Delta t} \\
&- V_{J,K,L_e} \Omega_{J,K,L_e}^{(m^*)}.
\end{aligned}
\tag{79}
$$

Again, m^* indicates that the components of $Q^{(m+1)}$ are used if they are available, and otherwise, the components of $Q^{(m)}$ are used. In addition, the superscript, e, in $R^{(m^*),e}$ emphasizes that $\tilde{H}^{(m),e}$ is evaluated entirely in terms of $Q^{(m)}$, as opposed to being evaluated as described below for the odd Jacobi iteration. Note that the Jacobian matrix, $\partial R_{J,K,L_e}^{(0)}/\partial Q_{J,K,L_e}^{(0)}$, is fixed over the course of a time step. Next, the following equation is solved for every point along a line of constant J, K, with $L = L_o$, an odd value,

$$Q_{J,K,L_o}^{(m+1)} = Q_{J,K,L_o}^{(m)} - \left[\frac{\partial \mathbf{R}_{J,K,L_o}^{(0)}}{\partial Q_{J,K,L_o}^{(0)}}\right]^{-1} \mathbf{R}_{J,K,L_o}^{(m^*),o}. \tag{80}$$

$$\mathbf{R}_{J,K,L_o}^{(m^*),o} = (\tilde{F}_{J+1,K,L_o}^{(m^*)} - \tilde{F}_{J,K,L_o}^{(m^*)})$$

Here,

$$
\begin{aligned}
&+ (\tilde{G}_{J,k+1,L_o}^{(m^*)} - \tilde{G}_{J,k,L_o}^{(m^*)}) \\
&+ (\tilde{H}_{J,K,L_o+1}^{(m),o} - \tilde{H}_{J,K,L_o}^{(m),o}) \\
&+ V_{J,K,L_o} \frac{(Q_{J,K,L_o}^{(m)} - Q_{J,K,L_o}^{n})}{\Delta t} \\
&- V_{J,K,L_o} \Omega_{J,K,L_o}^{(m)}.
\end{aligned}
\tag{81}
$$

Recall that $(\tilde{H}_{J,K,l+1} - \tilde{H}_{J,K,l})$ depends on $\{Q_{J,K,L-2}, Q_{J,K,L-1}, Q_{J,K,L}, Q_{J,K,L+1}, Q_{J,K,L+2}\}$. In this case, the superscript, o, in $R^{(m^*),o}$ emphasizes that $\tilde{H}^{(m),o}$ is evaluated in terms of $Q_{J,K,L}^{(m)}$ when L is odd, and in terms of $Q_{J,K,L}^{(m+1)}$ when L is even.

Once all points on the line of constant J and K have been updated, the iteration proceeds to the next line. When all components of $Q^{(m+1)}$ are calculated, a sweep is said to be completed. Typically, the total number of sweeps, m_s, is set to two or four, and $Q^{(m_s)}$ is accepted as the solution to Eq. (47) at time level $n + 1$.

Computational experience and theoretical analysis (Refs. 12–16) have shown that the use of the exact Jacobian, $\partial R_{J,K,L}^{(0)} / \partial Q_{J,K,L}^{(0)}$, leads to an unstable iteration scheme when large CFL numbers are used. In the past, several ad hoc formulations have been advocated on how to approximate the Jacobian with another matrix $B_{J,K,L}$. However, viewing the LIM scheme as a Diagonalized Approximate Newton's Algorithm (DANA), convergence of the method is guaranteed if the Jacobian of the iteration process has spectral radius less than or equal to one (Ref. 45). The importance of this new perspective of the LIM scheme is that a well-founded criterion is available to estimate under what conditions the scheme is convergent. This criterion allows the previous ad hoc formulations of $B_{J,K,L}$ to be readily checked.

In previous applications of the LIM scheme, the matrix B was taken to be

$$B_{J,K,L} = b_{J,K,L} \, I_{nq \times nq},$$

(82)

where

$$
\begin{aligned}
b_{J,K,L} = {} & \frac{V_{J,K,L}}{\Delta t} \\
& + \Big[0.125 \,(\lambda_{\xi\, J+1} + 2.0\,\lambda_{\xi J} + \lambda_{\xi J-1}) \\
& + 1.5\,(c_{\xi J+1} + c_{\xi J}) \Big]_{K,L} \\
& + \Big[0.125 \,(\lambda_{\eta\, K+1} + 2.0\,\lambda_{\eta K} + \lambda_{\eta K-1}) \\
& + 1.5\,(c_{\eta k+1} + c_{\eta k}) \Big]_{J,L} \\
& + \Big[0.125 \,(\lambda_{\zeta\, L+1} + 2.0\,\lambda_{\zeta L} + \lambda_{\zeta L-1}) \\
& + 1.5\,(c_{\zeta l+1} + c_{\zeta l}) \Big]_{J,K} + b_v,
\end{aligned}
$$

(83)

and

$$b_v = \alpha_v \frac{\mu}{\rho} \left(\vec{\sigma}_\zeta \cdot \vec{\nabla}\zeta \right)_{J,K,l},$$

(84)

28

where α_v is a relaxation parameter optimized for stability and convergence. However, in the present work the matrix B becomes

$$B_{J,K,L} = \begin{bmatrix} B_1 & 0 \\ 0 & B_2 \end{bmatrix}_{J,K,L}, \tag{85}$$

where

$$B_{1\,J,K,L} = \left[b\, I_{(ns+ne) \times (ns+ne)} - \frac{\partial \Omega}{\partial Q} V \right]_{J,K,L}, \tag{86}$$

and

$$B_{2\,J,K,L} = b_{J,K,L}\, I_{4 \times 4}. \tag{87}$$

Here ns and ne are the number of nonequilibrium species and energies, respectively. Note, this partitioning of B ignores the derivatives of w with respect to ρu, ρv, ρw, and E. However, it has been observed that this simplification does not affect the stability or accuracy of the scheme. In Appendix F, the complete derivation of the nonequilibrium source Jacobian, $\partial \Omega / \partial Q$, is included.

Thus, the nonequilibrium variables $(\rho_1, ..., \rho_{ns}, E_v)^T$ are solved for by a matrix inversion, and the variables $(\rho u, \rho v, \rho w, E)^T$ are solved for by a scalar inversion. Specifically, at the beginning of a given time step, an LU decomposition of $B_{IJ,K,L}$ is performed for every point. The decomposition is saved and not updated during a sweep. In fact, in the absence of significant temporal variations, the decomposition need not be updated at every time step. Once the higher order work of an LU decomposition is performed, sweepwise updates of the nonequilibrium variables can be computed with the lower order work associated with a simple back substitution.

4.0 RESULTS OF ONE-DIMENSIONAL COMPUTATIONS

Extensive one-dimensional numerical tests were performed with NEDANA to compare the results of the present numerical technique with the results of existing flow solvers. Three cases were chosen:

1. Shock tube problem.

2. Supersonic duct flow with area change.

3. Supersonic duct flow with area change and normal shock.

For all results presented in this section, the one-temperature model was assumed. One-dimensional computations using the two-temperature capabilities of NEDANA may be found in Ref. 18. These three cases are used to test the speed, accuracy, and stability of the present algorithm as compared with state-of-the-art flow solvers from other researchers.

In the comparisons presented in Figs. 3–8, variables are normalized by reference quantities. In all cases, the reference quantities are denoted by an * superscript. This should not be confused with the common usage of the * superscript to indicate sonic conditions. For the shock tube problem, these variables are normalized with the equilibrium properties of the high-pressure side of the diaphragm. The variables are normalized by the properties at the supersonic inlet for the two duct problems.

4.1 SHOCK TUBE

Shock tubes are long constant-area devices that are initially pressurized with two gases separated by a diaphragm. The gases are maintained in states of equilibrium that are very much different from one another. For instance, in the tube shown in Fig. 3, the left side of the tube is maintained at a pressure of 100 atm and a temperature of 9000 K. The right side is at 300 K and the pressure is 1 atm. The flow in the shock tube can be modeled as a one-dimensional inviscid wave propagation problem. At $t = 0$, the diaphragm is burst, and a strong compression wave (shock) moves to the right with velocity $\vec{C}$. As the shock wave propagates to the right, an expansion wave will propagate to the left as the mixture responds to the the adjacent fluid moving to the right. Also, a contact surface separating the two gases will follow the shock wave as the shock wave moves to the right compressing the fluid it encounters. The contact surface travels with velocity $\vec{V}$ where $\vec{V} < \vec{C}$. Figure 4 details the various structures present as they advance in time. Notice that the contact surface is maintained, since there is no mechanism to mix the gases. In the following shock-tube comparisons, relative to the distance the shock wave has traveled, time has not advanced far at all. Consequently, the contact surface is close behind (slightly to the left of) the shock wave. The double step is most noticeable in plots of the temperature. This is because the shock wave increases the temperature in advance of the contact surface. Most of the temperature increase then occurs across the contact surface for this particular case. Note that the contact surface does not compress and heat the gas like the shock wave. The changes across the contact surface are embedded in the fluid due to the initial differences in the states of the gas that existed across the diaphragm. Also, keep in mind that there is no velocity or pressure jump across the contact surface. Therefore, by observing the velocity and pressure curves, one can determine how well an algorithm is capturing shocks. Also, by observing the temperature and density plots, one can see both the shock and contact surface most clearly.

The shock-tube problem is ideal as a first case, because it is inherently unsteady. Spurious production of various constituents of the gas would indicate that the solver was unable to maintain time accuracy. To make a comparison, the conditions of the shock tube case performed by Shuen, Liou, and van Leer (Ref. 47) were used as starting conditions.

For $x \in [0.0, 5.0]$ cm $(p_L, T_L, u_L) = (100\ atm,\ 9000\ K,\ 0.0\ m/sec)$.

For $x \in [5.0, 10.0]$ cm $(p_R, T_R, u_R) = (1\ atm,\ 300\ K,\ 0.0\ m/sec)$.

Diaphragm

State L

State R

Initial State at $t = 0$

Initial Position
of Diaphragm

L

3

2

R

→
→ V

→
→ C

Expansion
Fan

Contact
Discontinuity
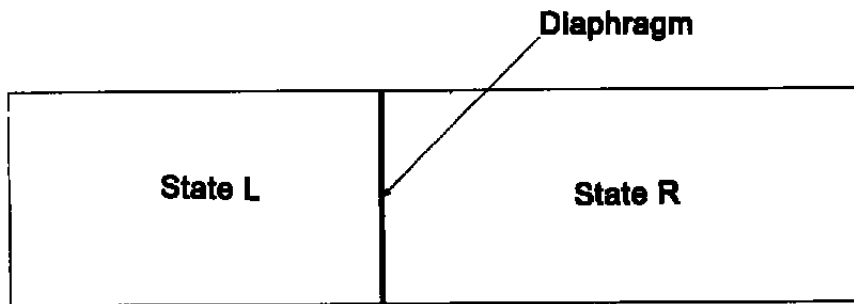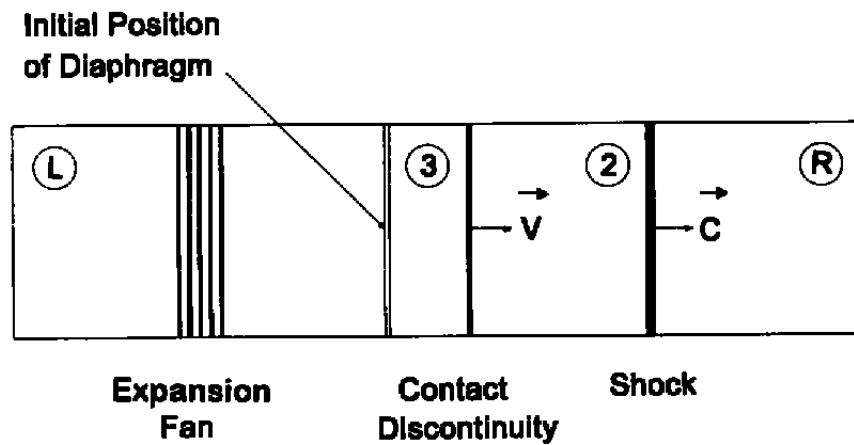
Shock

Flow State at $t > 0$

Figure 3. Shock tube schematic.

Figure 4. Wave structure of shock tube in time.
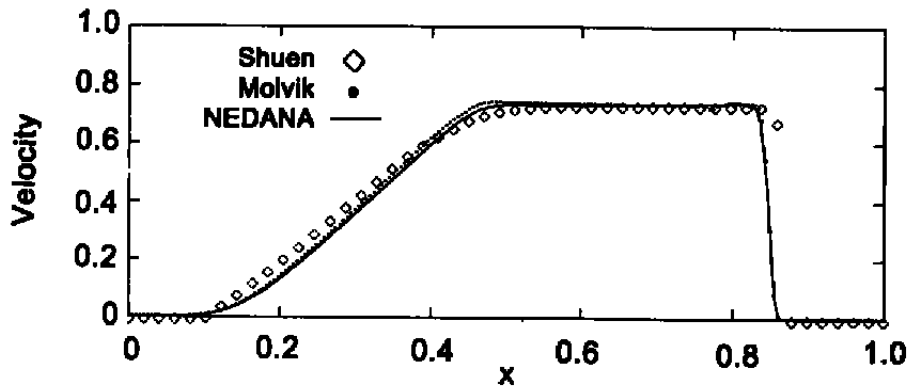
a. Velocity (normalized by a*)
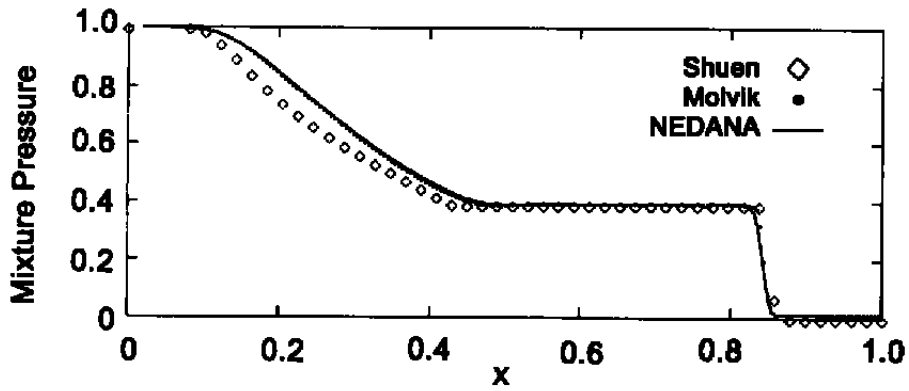
b. Mixture pressure (normalized by p*)
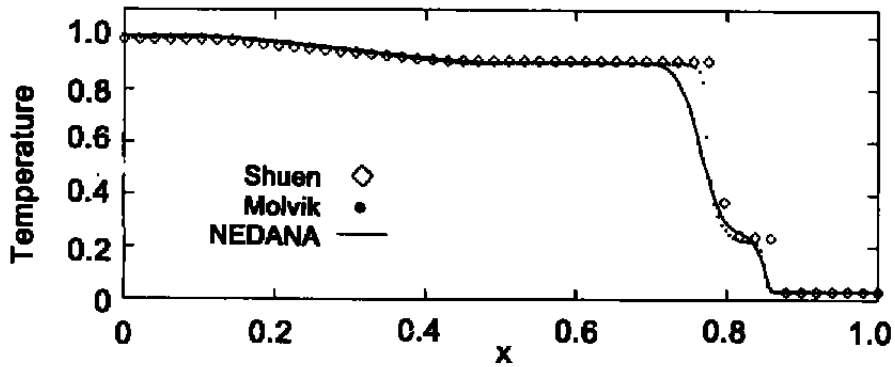
c. Temperature (normalized by T*)
Figure 5. Shock tube comparisons.

33
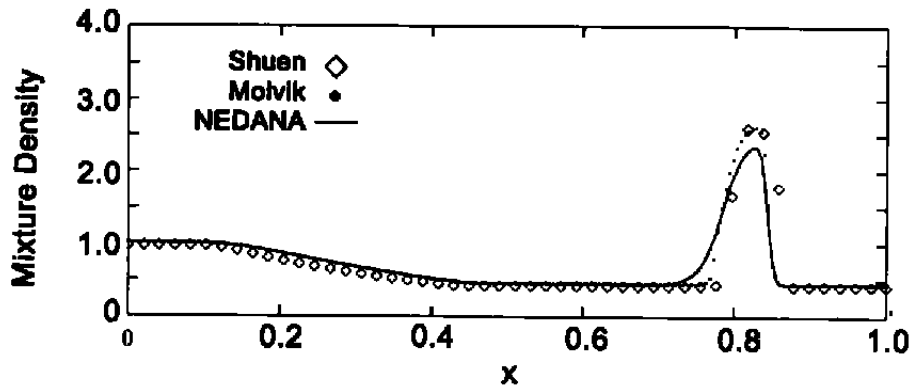
d. Mixture density (normalized by ρ^*)
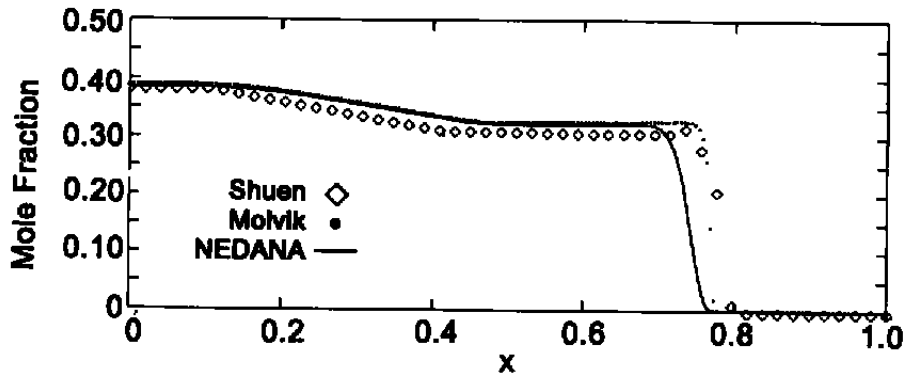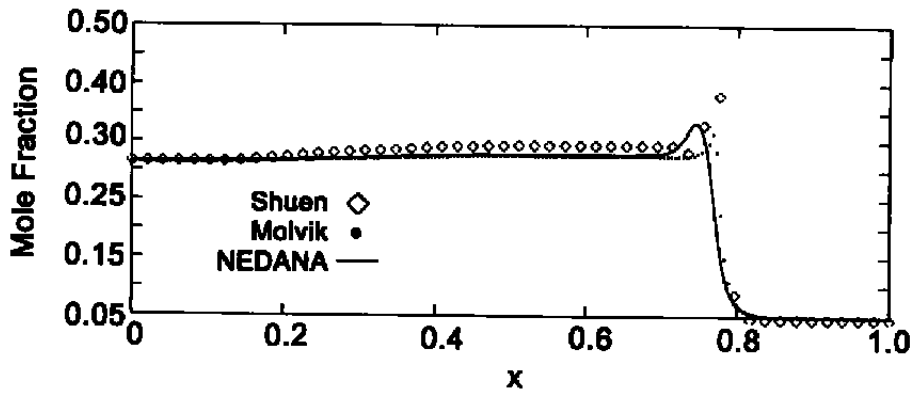
e. Atomic nitrogen

f. Atomic oxygen
Figure 5. Continued.
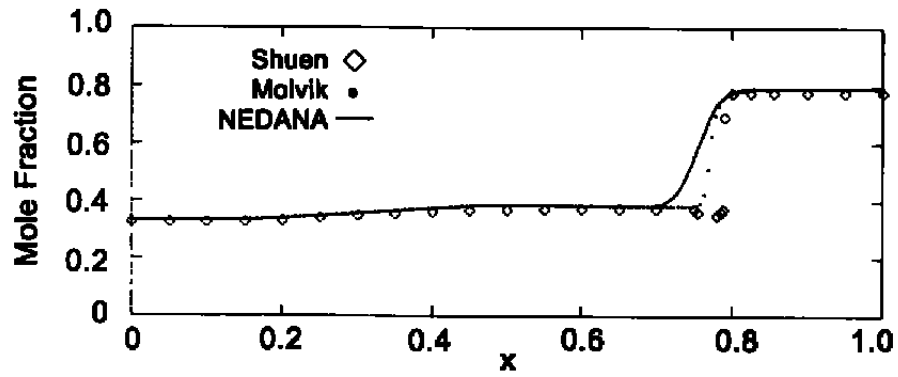
g. Molecular nitrogen and oxygen
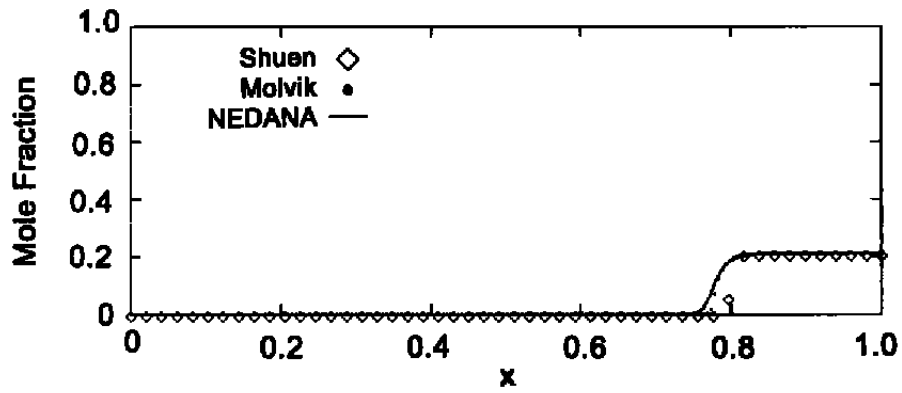
h. Nitric oxide
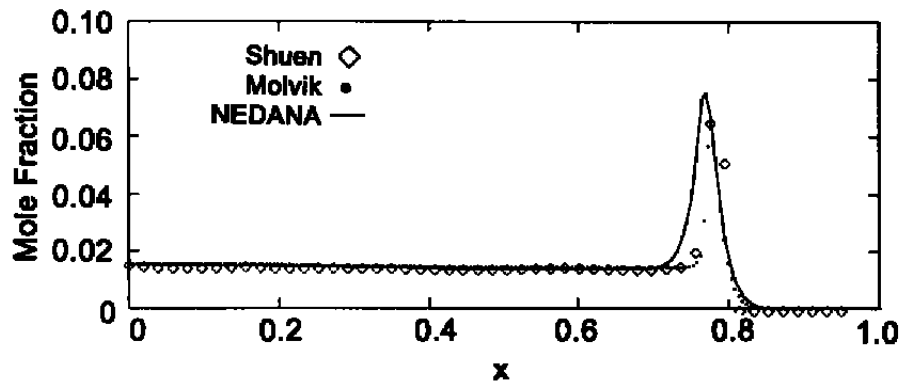
i. Electrons

Figure 5. Concluded.

The equilibrium air densities were computed using the curve fits of Prabhu and Erikson (Ref. 48) to be $\rho L = 2.627$ kg/m^3 for the high-pressure side and $\rho R = 1.1733$ kg/m^3 for the low-pressure side. In the following comparisons, all computations were performed on a grid consisting of 200 equally spaced nodes distributed over the interval [0.0, 10.0] cm. The comparison presented in Fig. 5 is made with Shuen's MUSCL-interpolated Roe upwind scheme (Ref. 47) and with Molvik's flow solver (Ref. 49). Both Molvik's flow solver and the present flow solver were run for 250 time steps at a CFL number of 0.5, which gave an absolute time of 0.167×10^{-5} sec. This number of steps was chosen so as to match the shock position of Shuen et al., who supplied no temporal data. Boundary conditions for this problem are unimportant, as the flow at both boundaries remains undisturbed. The results from NEDANA and the results from the Shuen et al. flow solver were computed using Dunn and Kang's (Ref. 50) reaction model (ionization reactions were not included). The results from Molvik's flow solver were obtained using Blottner's (Ref. 51) reaction model and were obtained at the AEDC by the authors. The results attributed to Shuen et al. were manually digitized from plots taken from the cited article. This accounts for waviness present in their results.

Similar results for the gas constituents and flow properties are presented in Fig. 5 for all three flow solvers. The pressure comparison, Fig. 5b, demonstrates that NEDANA produces shock fronts that are as sharp as those predicted by the flow solvers of both Molvik and Shuen et al. Figure 5c, however, shows that NEDANA does not reproduce the contact surface as well as the other codes.[1] This is because both the Molvik and Shuen et al. flow solvers are based on approximate Riemann solvers, which force the net flux to be modeled exactly across discontinuities in one dimension. In multi-dimensional flows in which the grid is not aligned with the discontinuity, much less favorable results are obtained using Roe's Riemann solver. It is encouraging that the present solver so cl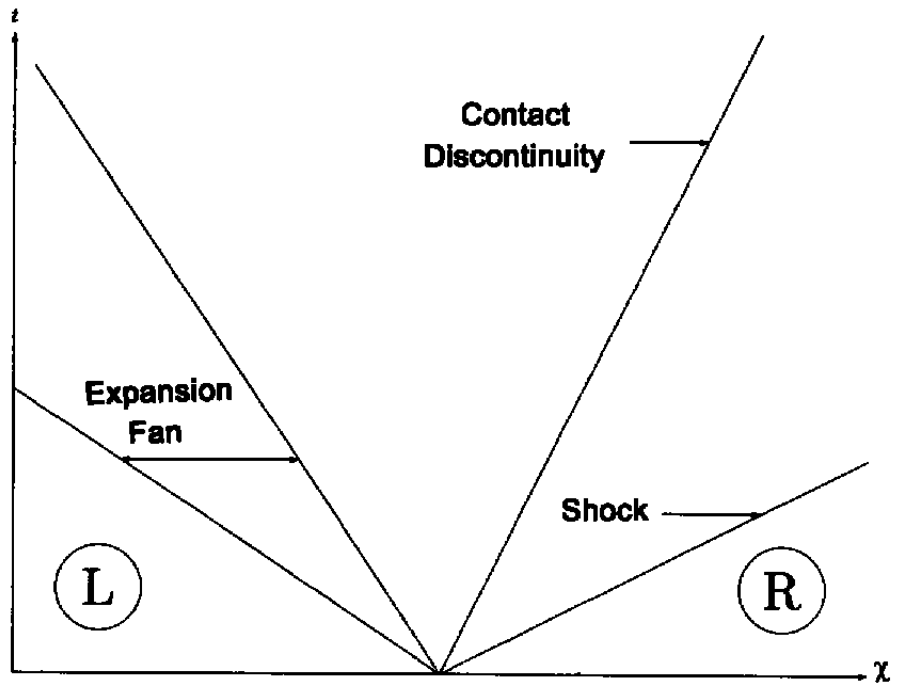osely follows the Molvik solution, as it is a well validated and widely used flow solver. The agreement in the expansion region between the NEDANA and the Molvik results on the one hand, and both disagreeing with the results of Shuen et al. on the other hand, would indicate that the solver of Shuen et al. does not handle the expansion correctly. Overexpansions are typical with flow solvers using higher order upwind schemes; but, since Molvik also uses a high order upwind method, it is not clear what mechanism is driving this disagreement.

Mole fractions for the species N, O, N_2, O_2, and NO as computed by the three flow solvers are plotted together in Figs. 5e–i. Again, the three flow solvers produce similar results, with the codes of Molvik and Shuen et al. producing sharper discontinuities and the results predicted by the Molvik and NEDANA flow solvers agreeing more closely, in general. Notice that the relative amount of the species changes greatly across the contact surface, but little across the shock. In particular, the mixture on the high-pressure side has little molecular oxygen, Fig. 5h. However,

---

1. Additional calculations have been made with NEDANA using a doubly finer mesh. The results show a much sharper contact surface, and the density comparison is nearly exact.

because of the temperature drop across the contact surface, the amount of molecular oxygen rises and remains nearly constant through the shock. This behavior illustrates the finite-rate nature of the chemical process. The motion of the shock is very rapid; thus, the chemical changes lag behind the shock. Consequently, changes in the species concentrations resulting from the shock are not observed until the changes resulting from the contact discontinuity begin. Changes across the contact surface then become dominant and obscure the much smaller changes initiated by the shock wave. By definition, the molar fractions of the constituents of the mixture must change discontinuously across the contact surface. This is not captured in the numerical simulation. Numerical smearing of the contact surface causes nonphysical intermediate temperatures that are conducive to the production of species not actually present at the contact surface. In particular, notice that all the flow solvers smear the contact surface and produce spurious overshoots in NO and O. This overshoot is related to the fact that the equilibrium mole fractions of NO and O as a function of temperature for a given pressure are non-monotone. This spurious production itself causes further smearing because there also is a lag in this nonphysical production of species. The numerical and nonequilibrium issues thus become entangled. By turning off the chemistry, NEDANA produces solutions with less smearing of the species mole fraction profiles across the contact surface; but with the chemistry enabled, the smearing is amplified.

4.2 SUPERSONIC DUCT

Supersonic ducts with area change, Fig. 6, are good model problems for testing a time-marching code's ability to achieve an accurate steady-state solution. Two cases were chosen for comparison: (1) a supersonic duct flow that remains supersonic to the exit; and (2) a supersonic duct flow that has had its exit pressure raised until a shock is standing approximately half-way down the duct, with subsonic flow in the remaining portion of the duct from the shock to the exit.

Results of the two nozzle flow problems are presented and compared with the results produced by Molvik's flow solver for the case with no shock. Both the flow solvers use the same reaction models used for the shock tube example. However, for the supersonic duct test cases, ionization reactions are included in the models. Results are also presented for the two test cases of equilibrium air solutions produced using curve fits taken from Ref. 48. The area distribution of the duct is taken as

$$A(x) = 5.5 + 4.5 \tanh(0.7x - 3.5); \quad x \in [0.0, \ 10.0] \ m,$$

which produces a nozzle with an area ratio of 10.0. Both grids consisted of 101 uniformly distributed points. The supersonic inflow conditions for both cases were:

$$T^* = 6000 \ K$$

$$p^* = 10 \ atm,$$

while the frozen Mach number at the inflow was 2.5.

In both of the supersonic duct test cases, convergence to steady state was assumed when the unsteady residual was driven to machine zero everywhere.
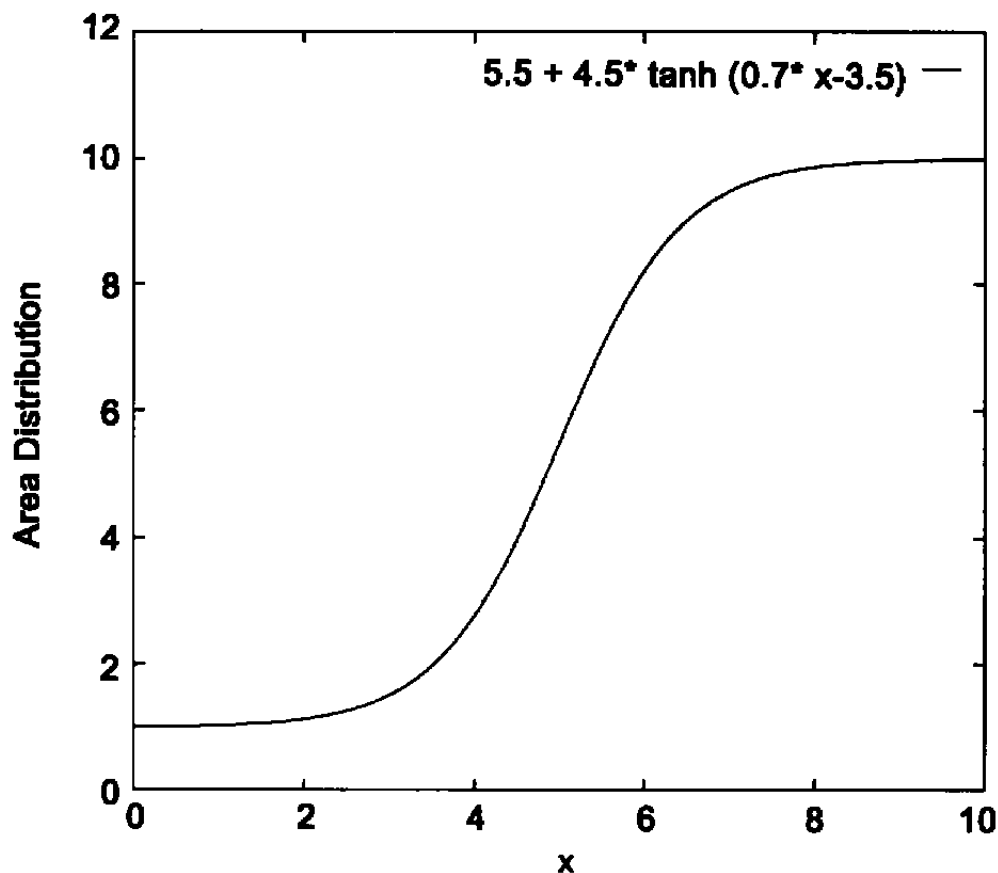
Figure 6. Duct schematic.

4.3 SUPERSONIC DUCT WITH AREA CHANGE

As this case is a pure supersonic expansion, the exit boundary conditions are those of supersonic outflow; i.e., the exit conditions are determined from a zeroth order extrapolation of the dependent variables at the j_{max} - 1 grid location. Initial conditions for this case were the uniform distribution of the dependent variables as determined from an equilibrium calculation of the inflow conditions.

The comparisons of the NEDANA results with results from Molvik's flow solver are presented in Fig. 7 along with the results from the author's equilibrium airflow solver. The distributions of the species and the flow properties are nearly indistinguishable among the three solutions, except for the NO comparison, Fig. 7h. Near the nozzle exit, where the density has dropped by an order of magnitude from the inflow value, the NO chemistry appears to be frozen.
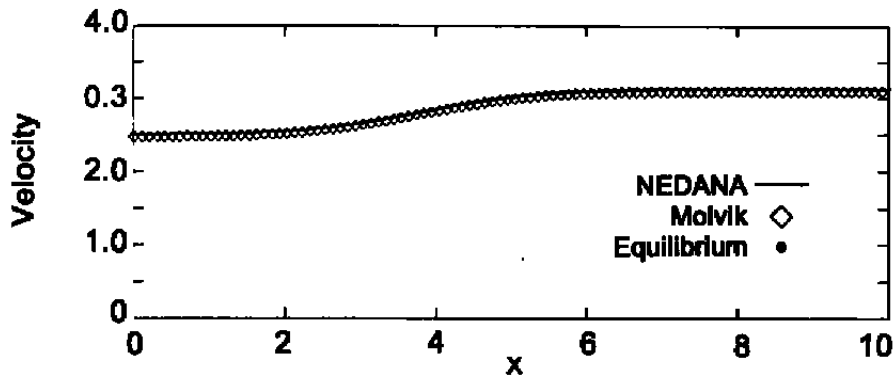
a. Velocity (normalized by a*)
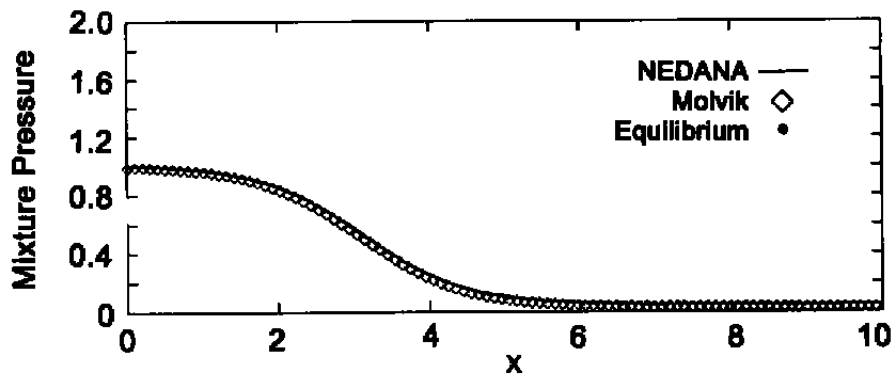
b. Mixture pressure (normalized by p*)
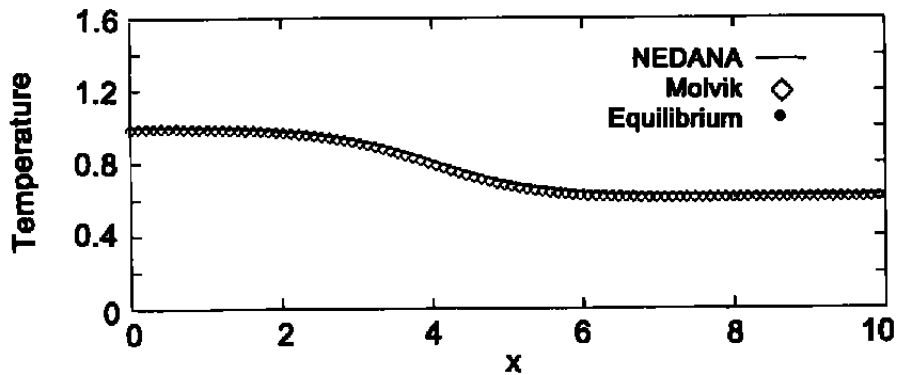
c. Temperature (normalized by T*)
Figure 7. Super duct.
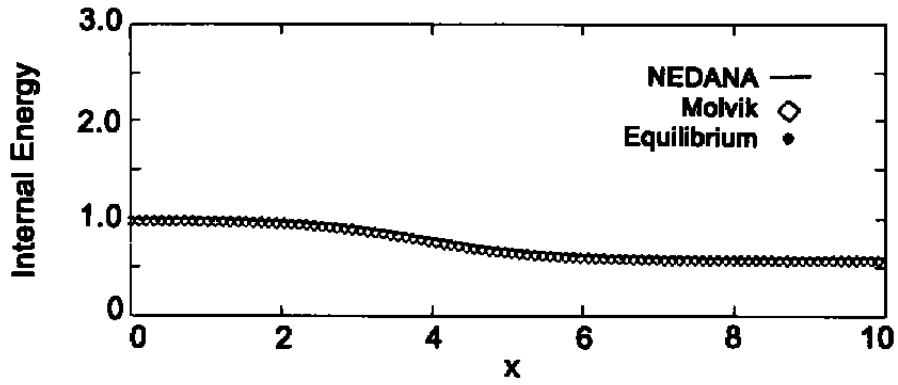
d. Internal energy (normalized by $e_I{}^*$)
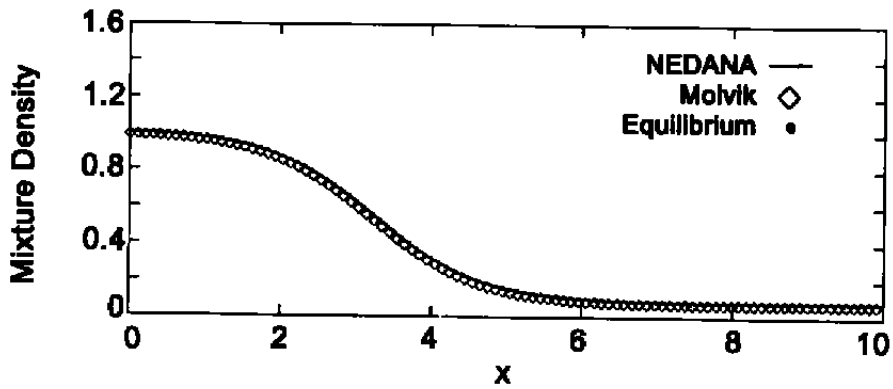
e. Mixture density (normalized by $\rho*$)
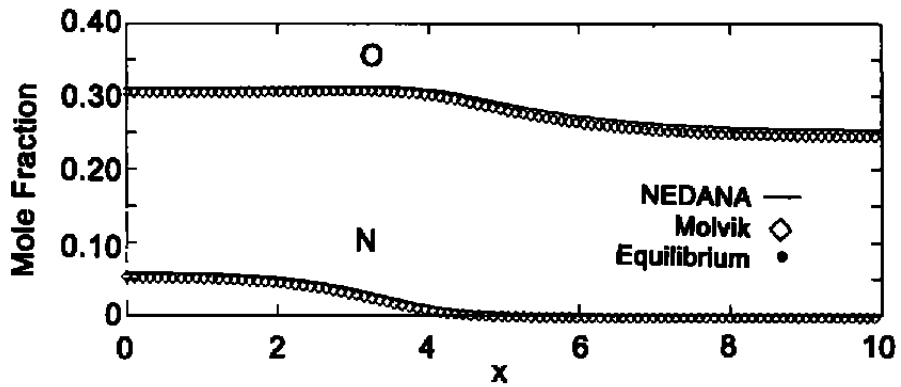
f. Atomic nitrogen and oxygen
Figure 7. Continued.
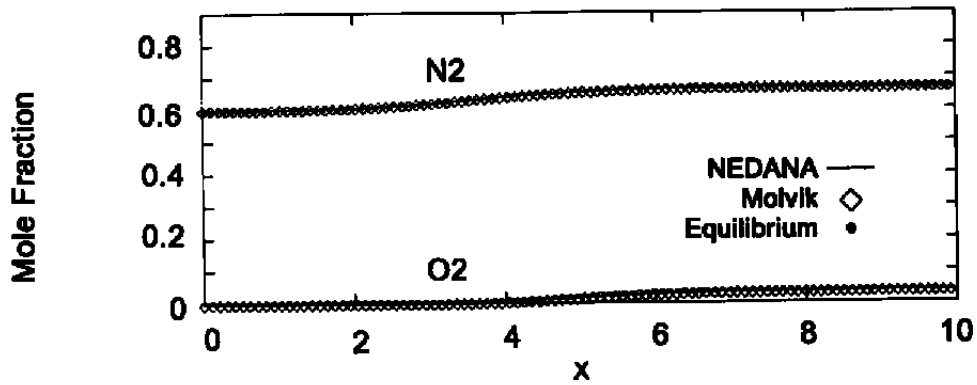
g. Molecular nitrogen and oxygen
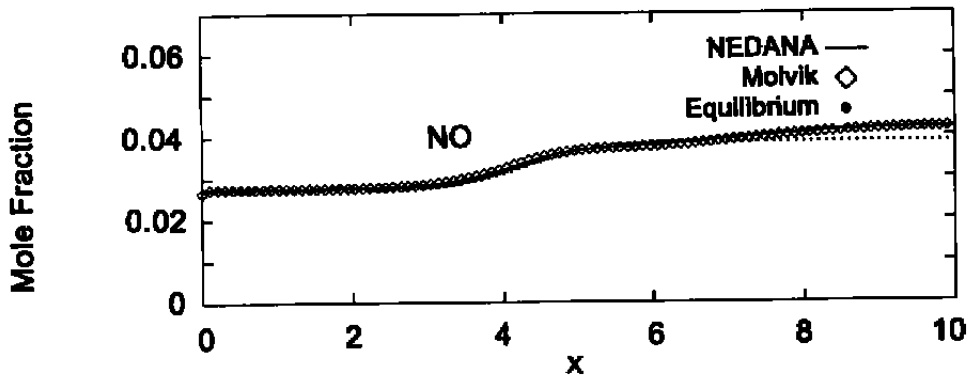
h. Nitric oxide
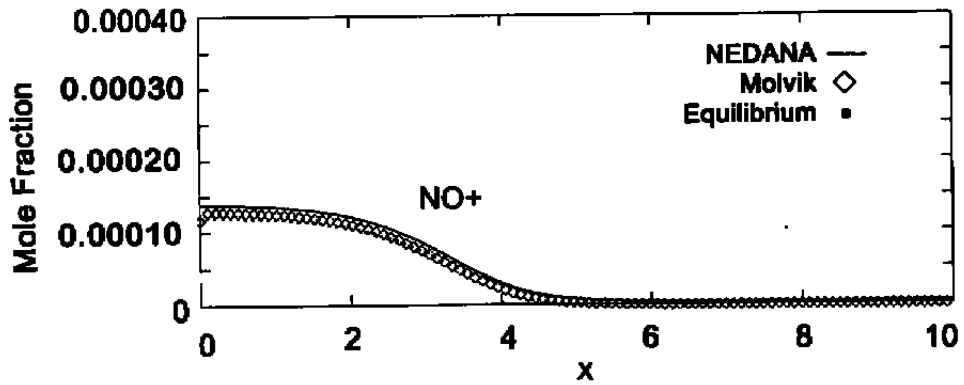
i. Electrons
Figure 7. Concluded.

4.4 SUPERSONIC DUCT WITH AREA CHANGE AND NORMAL SHOCK

This case is interesting because the flow downstream of the normal shock is subsonic. Consequently, a subsonic boundary condition is required at the exit. Initial conditions also must reflect this fact. Initial conditions were determined by first making an approximation to the properties in the duct from a perfect gas calculation. Then a crude equilibrium air calculation was made of the species distribution over the length of the duct. The initial shock location was close to the expected result. All of the dependent variables at the exit were determined by extrapolation as explained in the previous subsection; except that the specific total energy was calculated from the exit pressure which was imposed ($p_{exit} = 14.8$ atm). That is,

$$T_{exit} = \frac{p_{exit}}{\mathcal{R} \sum_{i=1}^{ns} \left(\frac{\rho_i}{\mathcal{M}_i} \right)}.$$

Knowing the mixture temperature and the constituents at the exit, NEQPAK returns the specific internal energy. The total specific energy is then found by adding the kinetic energy, as

$$\epsilon_{exit} = \epsilon_I + \tfrac{1}{2} u^2.$$

The comparisons are shown in Fig. 8. Only the equilibrium results are available to compare with NEDANA, because the version of Molvik's code used in this study does not make provisions for subsonic outflow boundary conditions.The results from NEDANA are in excellent agreement with the equilibrium air solution except for the distribution of $NO+$ downstream of the shock. This results because the equilibrium air solution considers eleven species, whereas the NEDANA computation was performed with a seven species model.

Note the changes in the constituents of the mixture across this shock, relative to the changes discussed with regard to the shock and contact surface in the shock tube. The changes in pressure and temperature are not as severe in the duct so that the adjustment process is not as smeared as in the shock tube. The constituents change cleanly across the duct shock, except for a spike in atomic oxygen. It is also important to recognize that in the duct, substantial dissociation exists on both sides of the shock; whereas in the shock tube, the air molecules are shocked from a nearly quiescent state.
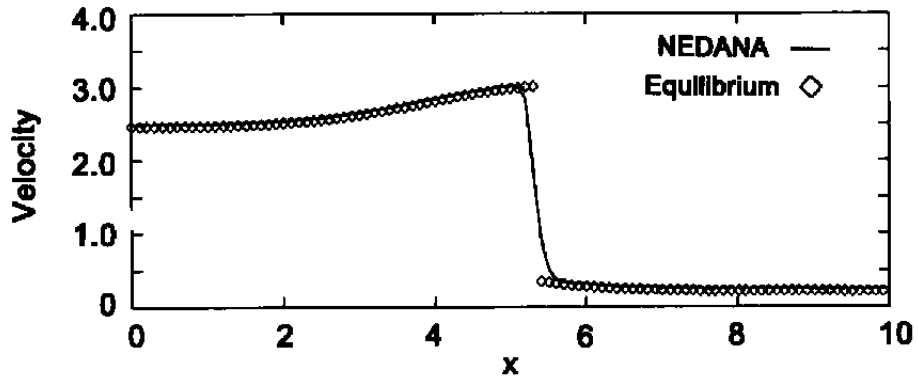
a. Velocity (normalized by a*)
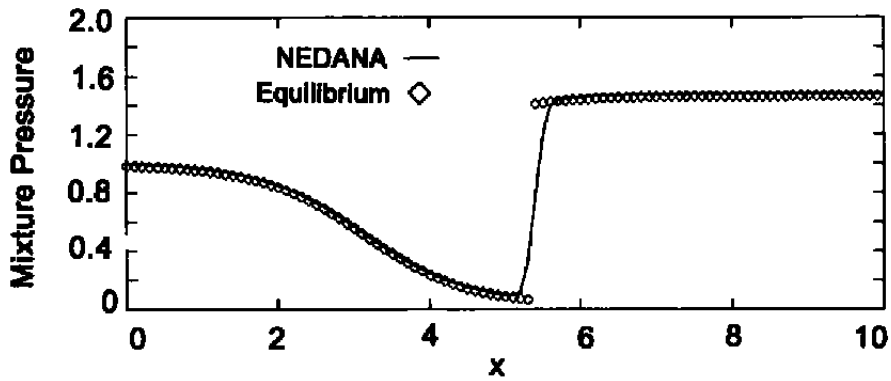
b. Mixture pressure (normalized by p*)
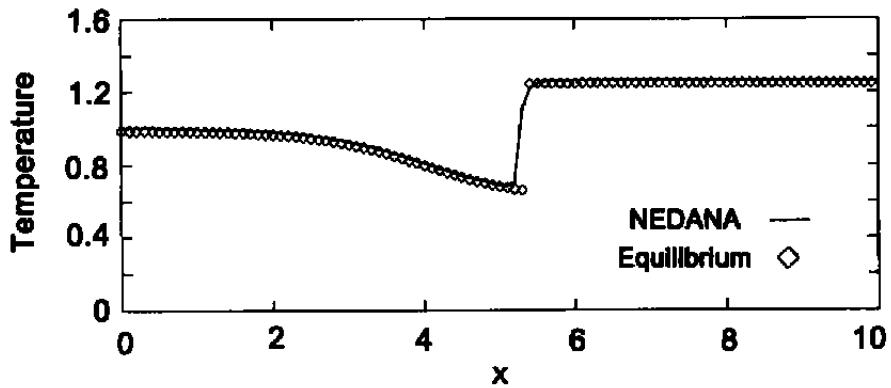
c. Temperature (normalized by T*)
Figure 8. Shock tube comparisons.
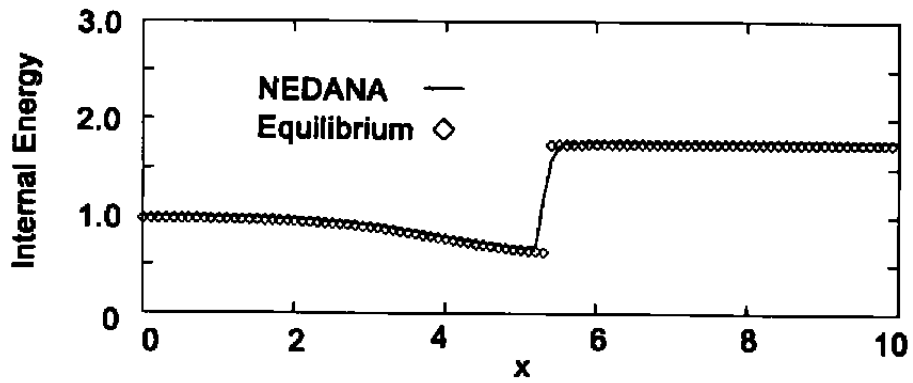
d. Mixture density (normalized by e_I*)
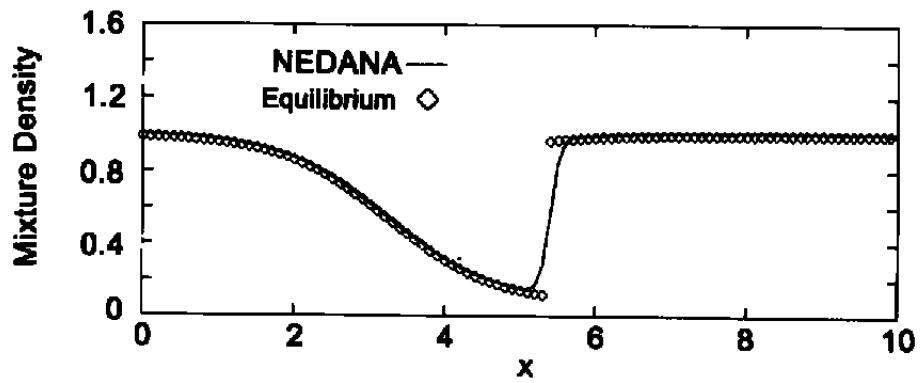
e. Mixture density (normalized by $\rho*$)
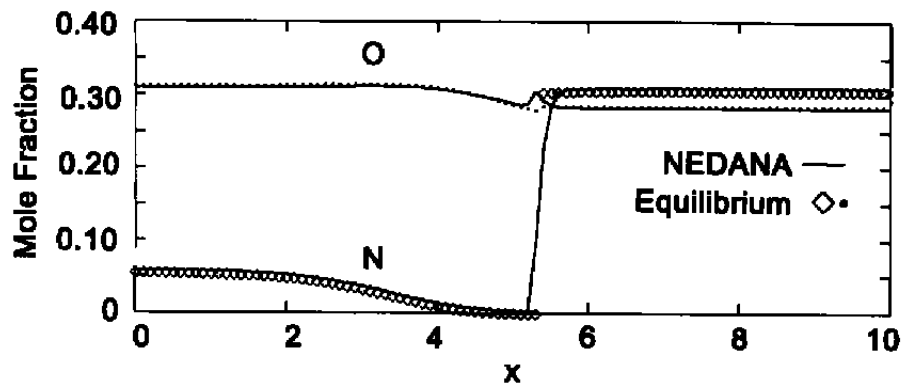
f. Atomic nitrogen and oxygen
Figure 8. Continued.
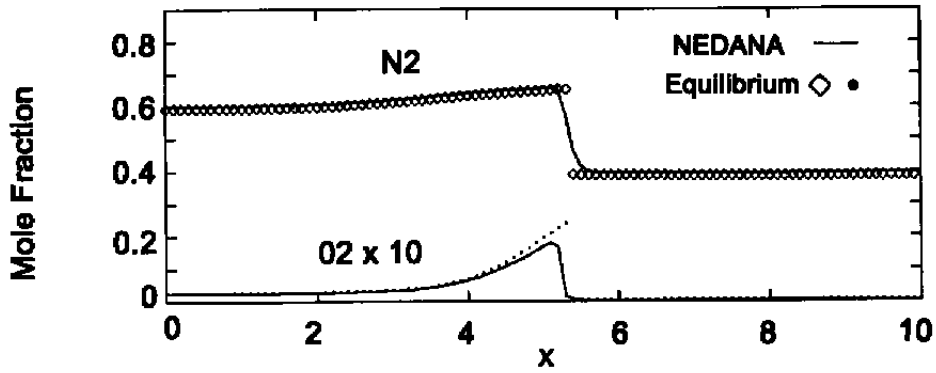
g. Molecular nitrogen and oxygen
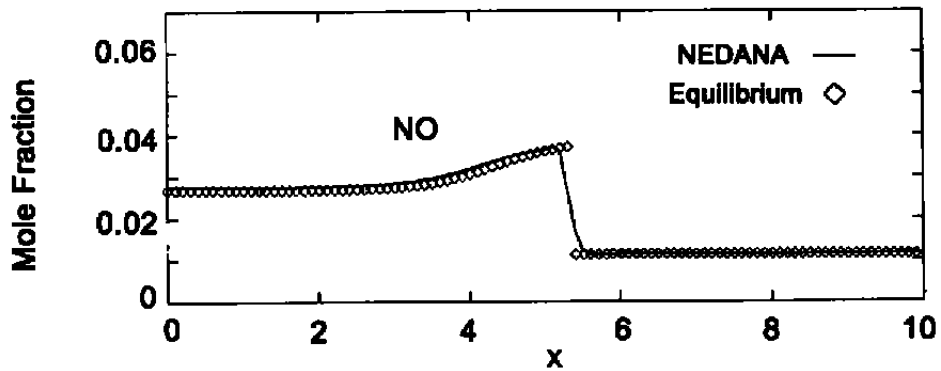
h. Nitric oxide
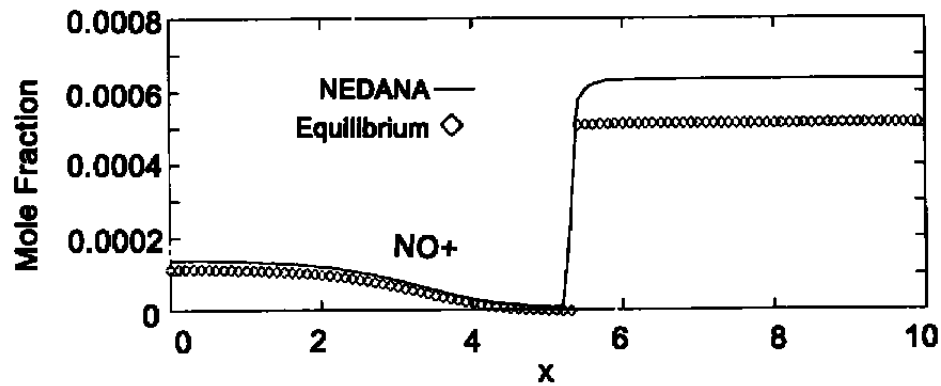
i. Electrons

Figure 8. Concluded.

5.0 RESULTS OF TWO- AND THREE-DIMENSIONAL COMPUTATIONS

Extensive flow computations were performed to validate and demonstrate the methodology and accuracy of the two-dimensional and three-dimensional modes of NEDANA. The classes of problems studied include:

1.   Laminar Separated Flows on Hypersonic Flat Plate/Wedges

2.   Nonequilibrium Flows around Hemisphere Cylinders

3.   Chimera Domain Decomposition in Nonequilibrium Flows

The numerical results are compared to both experimental data and numerical results from existing flow solvers where available.

5.1 BOUNDARY CONDITIONS

In this section, the boundary conditions imposed for the three test problems are discussed. In all cases, the flow was supersonic. Therefore, the upstream boundary was specified with free-stream values. The flow at the outflow boundary was primarily supersonic. Only a small subsonic region existed in the boundary layer at the outflow boundary. Therefore, a zeroth–order extrapolation was used. Fluxes at symmetry planes were calculated by reflecting grid points across the symmetry boundary. At the body surface, a no–slip condition was applied such that all components of the velocity were zero. For non–catalytic walls, a zero normal gradient in the species mass fractions was set at the wall. For fully catalytic walls, the species mass fractions at the wall were set to their equilibrium values based on the wall temperature. The nonequilibrium flow experiments investigated in this study reported a constant wall temperature of 555.55 K. Calculations using the method of Prabhu and Erickson (Ref. 48) showed that for this temperature the equilibrium composition of air was equal to the free-stream composition. Furthermore, this result was nearly independent of the equilibrium density. Therefore, the species mass fractions at the wall were set to their free-stream values. The pressure at the wall was set assuming zero normal pressure gradient. The temperatures at the wall were set to the reported wall temperature. Park (Ref. 52) reports that the vibrational and electronic temperatures of molecules leaving a surface are nearly equilibrated with the translational wall temperature. Therefore, the translational–rotational and vibrational–electronic temperatures at the wall were set to a common value.

Table 1. Flow Conditions and Geometries for Flat-Plate/Wedge Calculations

Wedge Angle (*deg*)	M_∞	$Re_\infty (1/m)$	$T_\infty(K)$	$p_\infty(Pa)$	$T_{wall}(K)$
15.05	15.67	$4.885 \times (10)^5$	40.31	8.27	294.4
18.00	15.58	$4.521 \times (10)^5$	42.53	8.34	294.4
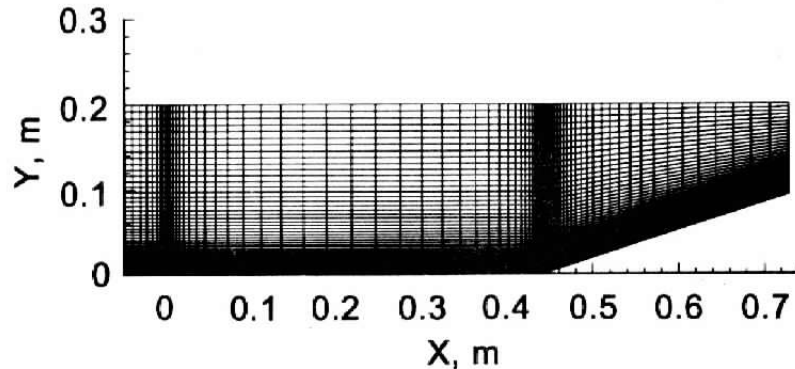
Figure 9. Flat-plate/wedge grid, $101 \times 3 \times 101$.

5.2 HYPERSONIC LAMINAR FLOW OVER A FLAT-PLATE/WEDGE

The flow over a compression corner formed by the intersection of a flat plate and a wedge was chosen as a test case for the two-dimensional, viscous coding of NEDANA. Measurements for laminar, attached and separated flows on flat–plate/wedge configurations reported in the CUBDAT database by Holden (Ref. 53) have been used by various researchers for code validation (Refs. 54, 55, and 56). Although the configuration is geometrically simple, the physics of the flow field are very complicated and serve as an ideal test case for viscous hypersonic phenomenon. A very strong leading–edge shock is generated that extends downstream and intersects the wedge flow field. In addition, for sufficiently large wedge angles, a boundary-layer separation region forms in the corner. On the wedge, downstream of this separation region, the flow is compressed and the boundary layer thins, resulting in large increases in skin friction and heat transfer. Furthermore, the compression waves produced by the corner coalesce into a shock wave that intersects with the leading–edge shock, generating an expansion fan and shear layer.

The CUBDAT database includes pressure, heat-transfer, and skin-friction data for nominally two-dimensional (finite-span) 15.05-*deg*, 18-*deg*, and 24-*deg* wedges. The work of Rudy et al. (Ref. 55) concludes that the inclusion of three-dimensional effects is necessary for accurate comparisons to experimental data for the 24-*deg* wedge case due to the larger boundary-layer separation region.

Therefore, two-dimensional comparisons are made only to the 15.05-*deg* and 18-*deg* wedge data. The conditions for the simulations are listed in Table 1. Note that the Reynolds number was low enough that the flow remained laminar. In addition, the high Mach number is achieved by an extremely low free-stream temperature. Therefore, the flow is assumed a perfect gas and not a chemically reacting gas. As a result, the flat–plate and wedge data comparisons allow for a validation of the NEDANA flow solver in the absence of the additional complexities of turbulence and chemistry.

For both wedge angles, the length of the flat plate and wedge are 0.4396 *m* and 0.3048 *m*, respectively. The test geometries were modeled as two–dimensional compression corners with 101 × 3 × 101 grids. (Note that the current version of NEDANA is a three-dimensional, finite-volume flow solver with the grid system described in Appendix B. Therefore, a minimum of three grid points is required in all coordinate directions.) A viscous wall spacing of 1.0×10^{-5} *m* was used. This viscous spacing produced values of $y^+ < 0.1$. The calculation of y^+ is useful for determining the minimum grid spacing required for accurate viscous solutions even in the absence of turbulence. A typical grid is shown in Fig. 9. The current version of NEDANA has been developed for nonequilibrium computations and, therefore, receives all thermodynamic and transport properties from NEQPAK. As a consequence, the perfect-gas flow was modeled as a chemically frozen mixture of N_2 and O_2, representing air. This fact is noteworthy because the NEQPAK curve fits for thermodynamic and transport properties were formulated for 100 K to 30,000 K.

Steady-state computations were made with the NEDANA flow solver for both the 15.05-*deg* and 18-*deg* wedge configurations using a global time step and a maximum CFL number of five. The dissipation parameters ((see Eq. (52)) were set at $\kappa_2 = 0.8$ and $\kappa_4 = 1.8$. Numerical tests showed that the use of local time stepping greatly increased the number of iterations for convergence. This finding may be due to the unsteady nature of the separated flow region. Steady-state solutions were typically achieved in 10,000 iterations with a reduction in residual of four orders of magnitude. Pressure, heat–transfer, and skin–friction results for the 15.05-*deg* wedge case are presented in Figs. 10, 11, and 12. The results are compared to experimental data. Solutions were also computed using Molvik's TUFF (Ref. 49) flow solver and the AEDC flow solver XMERA (Ref. 42). These results are included to assess the performance of NEDANA versus other state–of–the art flow solvers. Results from all three flow solvers are in good agreement with the experimental data. Note, the results of all three flow solvers may differ slightly due to the use of different curve fits for thermodynamic and transport properties.
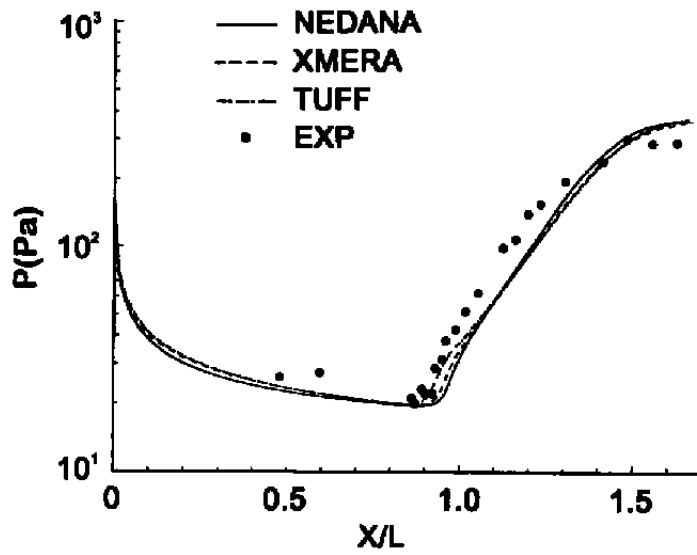
Figure 10. Pressure distributions for laminar flow over a 15.05-deg wedge, $M_\infty = 15.67$.

Figure 11. Heat-transfer distributions for laminar flow over a 15.05-deg wedge, $M_\infty = 15.67$.

Figure 12. Skin friction distributions for laminar flow over a 15.05-deg wedge, $M_\infty = 15.67$.

The calculation of the size of the separation region that forms at the juncture of the flat plate/ wedge is extremely sensitive to the numerical dissipation of the flow solver. A flow solver with low numerical dissipation should accurately predict both the size and shape of the separation region. As the dissipation of the numerical scheme increases, the size of the predicted separation region conversely decreases. Extremely dissipative schemes may actually suppress the formation of a separation region entirely. The effect of the separated flow is to decrease both the skin friction and heat transfer at the wall. As a result, the extent of the separation region is marked by a drop in the skin-friction and heat-transfer distributions. With this phenomenon in mind, an examination of the skin-friction and heat-transfer distributions reveals that NEDANA and XMERA are slightly more dissipative than TUFF. This result was anticipated because the TUFF flow solver is based on an upwind algorithm, whereas the NEDANA and XMERA flow solvers are based on central difference schemes with constant numerical dissipation parameters.

To investigate the effects of decreased numerical dissipation, a series of computations were performed with NEDANA in which the dissipation parameters were lowered to $\kappa_2 = 0.4$ and $\kappa_4 = 0.8$. Additional computations were performed where the dissipation parameters were also scaled by the normalized velocity such that $\kappa_2 \rightarrow 0.0$ and $\kappa_4 \rightarrow 0.0$ at the no-slip wall. This scaling was performed to further lower the dissipation in the viscous region near the wall. The decreased numerical dissipation did not significantly improve the NEDANA results. Only a slight increase in the size of the separation region was achieved, and at a cost of decreased numerical stability. A further numerical experiment was performed where the viscous spacing was increased to 1.0×10^{-4} m. The ensuing computation completely failed to predict the separation region. This result would indicate that adequate viscous grid resolution is more significant than the magnitude of the dissipation parameters employed.

Similar results are presented in Figs. 13, 14, and 15 for the 18-*deg* wedge case. The NEDANA and XMERA flow solvers performed similarly. However, the upwind Roe scheme of TUFF initially generated a nonphysical solution in the vicinity of the separation region where the flow switches from supersonic to subsonic. This nonphysical behavior is common to upwind Roe schemes and can be eliminated by applying an entropy fix (eigenvalue limiter) to the eigenvalues (Ref. 49). By increasing the absolute value of the entropy fix, physically consistent solutions were obtained. However, the TUFF results then offered no advantage over the central difference NEDANA and XMERA flow solvers. All three flow solvers failed to completely predict the extent of the separation region.
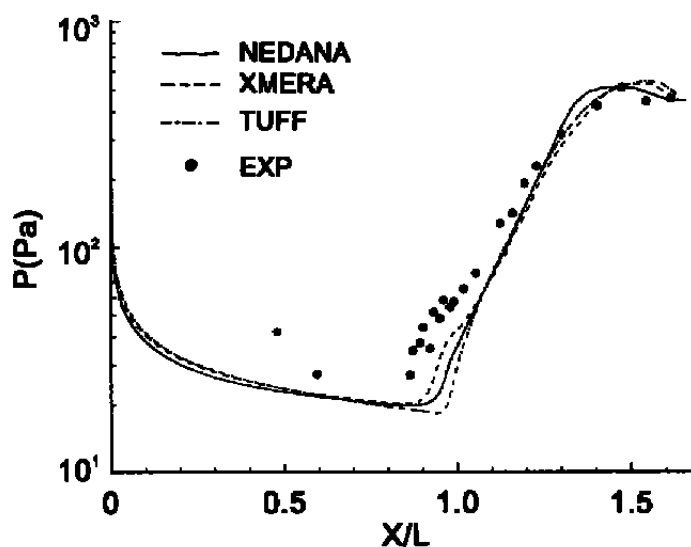
Figure 13. Pressure distributions for laminar flow over an 18-deg wedge, $M_\infty = 15.58$.

The results of the hypersonic laminar flat-plate/wedge cases have shown NEDANA to perform as well as current state-of-the art flow solvers. The NEDANA flow solver proved to be more stable and to converge more rapidly for hypersonic flow conditions than the XMERA flow solver. Where the NEDANA flow solver was able to run with a CFL number of five and converge in 10,000 iterations, the XMERA flow solver was limited to a CFL number of one-tenth and required 100,000 iterations to converge. Where the NEDANA code proved to be robust for both wedge geometries, the TUFF flow solver was susceptible to spurious solutions, even for small changes in wedge angle.
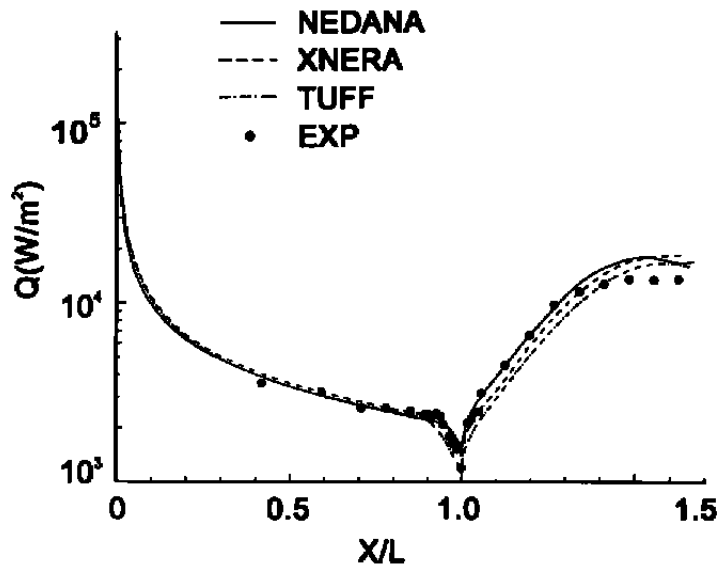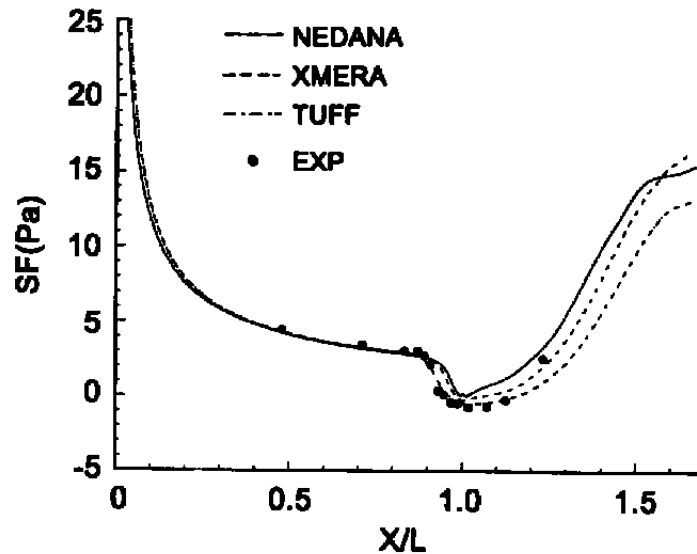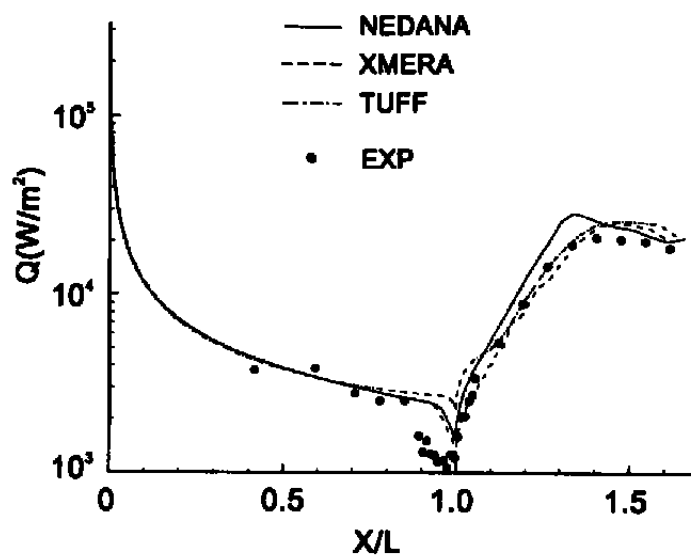
Figure 14. Heat-transfer distributions for laminar flow over an 18-deg wedge, $M_\infty = 15.58$.
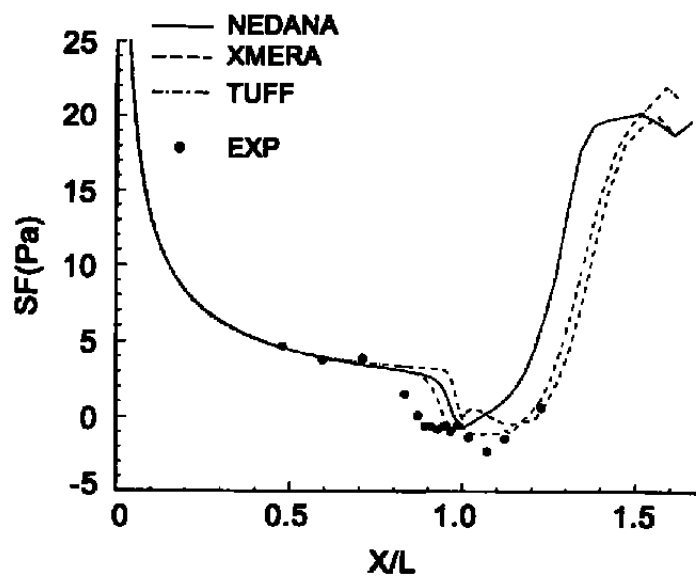
Figure 15. Skin-friction distributions for laminar flow over an 18-deg wedge, $M_\infty = 15.58$.

5.3 NONEQUILIBRIUM FLOW AROUND HEMISPHERE CYLINDERS

The computation of the thermal and chemical nonequilibrium flow fields around hemisphere cylinders (Refs. 57 and 58) was selected as a validation case for the nonequilibrium capabilities of NEDANA. Computations were made for the three geometries listed in Table 2. The three hemisphere cylinders have different radii and are referred to as model 1, model 2, and model 3. The nominal flow conditions for all three models are $M_\infty = 9.8$, $Re_\infty = 3.025 \times (10)^5$ $(1/m)$, $T_\infty = 450 \ K$, $p_\infty = 230 \ Pa$, and $T_{wall} = 555.55 \ K$. The conditions are such that the flow is in chemical and thermal nonequilibrium. The free-stream total enthalpy, $h_{0\infty}$, is 9.14 MJ/kg. A five species air chemistry, two-temperature model was applied using the reaction rates of Park (Ref. 36). In this work, the dissociation reactions are governed by a generic temperature where $\alpha = 0.3$ (see Eq. (31)). Heat-transfer measurements were obtained with both thin-film and thermocouple gauges. The thin-film gauges were coated with mother of pearl to minimize wall catalycity, whereas the thermocouple gauges allowed for wall catalysis. Models 1 and 2 were fitted with stagnation point thin-film gauges for measuring heat transfer, and model 3 was fitted with a stagnation point thermocouple gauge for measuring heat transfer.

Table 2. Hemisphere/Cylinder Geometries and Stagnation Point Catalytic Boundary Conditions

Model	Rn (m)	L (m)	Wall B.C.
1	0.0127	0.1143	Noncatalytic
2	0.0254	0.2032	Noncatalytic
3	0.0508	0.4064	Catalytic

Grid resolution studies were performed with the current flow solver on the intermediate-sized model, model 2, to determine the grid requirements for achieving valid pressure and heat-transfer results for nonequilibrium flows. Josyula and Shang (Ref. 57) reported using a mesh system with 40 points in the body-tangential direction and 50 points in the body-normal direction with a viscous wall spacing of $5.0 \times (10)^{-6}$ m. Using the results of Josyula and Shang as a guide, the system of meshes listed in Table 3 was developed. A typical grid is shown in Fig. 16. Grids 1, 2, and 3 were developed such that the grid distribution functions in the body-tangential and body-normal directions were the same. This criterion was enforced to maintain the same relative resolutions in all three grids. Grid 4 was created with the same number of grid points as Grid 1 but with the viscous spacing of Grid 3. Grid 4 was developed to assess the relative importance of the viscous spacing and the total number of points in the body-normal direction. (Grids 5, 6, and 7 will be discussed later.) Note that NEDANA was used in a fully three-dimensional, finite-volume mode with the grid system described in Appendix B. Therefore, five grid points were required in the body-azimuthal direction.

Table 3. Details of Grid Resolution Study

Grid	Dimensions	No. Points	$\Delta n(m)$	Iteration for Conversion
1	$51 \times 5 \times 51$	13005	$1.0 \times (10)^{-5}$	1100
2	$75 \times 5 \times 75$	28125	$7.0 \times (10)^{-6}$	1900
3	$101 \times 5 \times 101$	51005	$5.0 \times (10)^{-6}$	2850
4	$51 \times 5 \times 51$	13005	$5.0 \times (10)^{-6}$	1300
5	$51 \times 5 \times 51$	13005	$1.0 \times (10)^{-6}$	3700
6	$51 \times 5 \times 75$	19125	$1.0 \times (10)^{-6}$	4500
7	$51 \times 5 \times 75$	19125	$5.0 \times (10)^{-7}$	5000
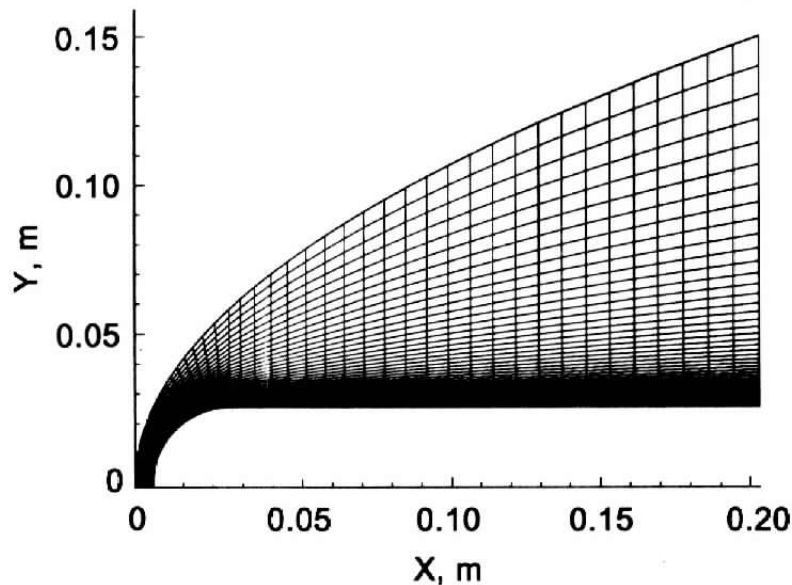
Figure 16. Hemisphere/cylinder grid, $51 \times 5 \times 51$.

Steady-state computations were made with NEDANA for Grids 1, 2, 3, and 4 using local time stepping and a maximum CFL number of ten. The dissipation parameters were set at $\kappa_2 = 0.8$ and $\kappa_4 = 1.8$ for all cases. Numerical tests showed that the use of a local time step gave the optimal convergence rate for the hemisphere cylinder flow fields. (This result is contrary to the findings of the flat-plate/wedge investigation and emphasizes the uncertainties of using local time-stepping methods.) The solutions were considered converged when the heat transfer to the wall varied by less than 1 percent over a characteristic time step based on the minimum time step for the grid,

where $t_{char} = Rn / u_\infty$. The number of time steps required to obtain a steady-state solution is also listed for each grid in Table 3. The NEDANA flow solver operated at a speed of 2.03×10^{-3} cpu-s/pt/iter on a Convex 3840 computer for five species in chemical and thermal nonequilibrium.

Surface pressure and heat-transfer distributions for the grid resolution study of model 2 with grids 1, 2, 3, and 4 are presented in Figs. 17 and 18. The comparisons with experimental measurements for pressure are excellent. Furthermore, the calculation of surface pressure is largely independent of the grid used. The pressure distributions for all grids differed by less than 2 percent. The comparisons with experimental heat-transfer measurements show a greater grid dependency. As the grid resolution and viscous spacing are refined, the computed heat transfer increases. The viscous spacing normal to the wall is critical in predicting surface heat transfer. This fact is evident in the comparison of the surface heat transfer for grids 3 and 4. Grid 4 has the same initial viscous spacing as grid 3, but only half the number of points normal to the body. Nevertheless, the surface heat-transfer distribution obtained on grid 4 is in better agreement with the results obtained on grid 3 than those obtained on grids 1 or 2. A comparison of the stagnation-point heat transfer for grids 1, 2, and 4, shows they differ from that of grid 3 by approximately 20 percent, 10 percent, and 5 percent, respectively. The comparisons are taken relative to grid 3, because it is assumed the grid with the best resolution will produce the most accurate results. Clearly, the computed surface heat-transfer distributions are grid dependent. For grid 3, $y^+ = 0.3$ at the stagnation point, and downstream of the spherical surface $y^+ \approx 1.5$. A viscous resolution corresponding to $y^+ < 1$ was initially expected to yield grid-independent results. However, the criteria for the accurate calculation of surface heat transfer proved to be more complex.

Siddiqui et al. (Ref. 59) report similar difficulties in computing grid-independent surface heat transfer using a variety of thin-layer Navier-Stokes algorithms. Siddiqui et al. computed the flow over spherically blunt cones at similar Mach numbers and Reynolds numbers. (However, the free-stream temperature and velocity were such that the flows were not chemically reacting.) They developed an expression to estimate the required viscous spacing as a function of Mach number and Reynolds number. Applying this expression to the hemisphere cylinders of this study, the estimated viscous spacing required for grid-independent heat transfer is $5.0 \times (10^{-7})$ m. To generate a grid with this viscous spacing and maintain a similar grid distribution as grids 1, 2 and 3 is not practical. The resulting grid would require hundreds of points normal to the body. Also, note that the number of iterations to convergence, as well as the cpu-s/iter would increase beyond practicality. Therefore, a compromise was made by holding the number of points normal to the body constant. As a result, a decrease in the viscous spacing produces poorer resolution of the shock layer. This reduced resolution in the shock layer is of importance in nonequilibrium flows where the chemical reactions can affect the heat transfer to the surface. This need to accurately resolve the chemical reactions in the shock layer is an additional constraint not imposed on the perfect-gas work of Siddiqui et al.
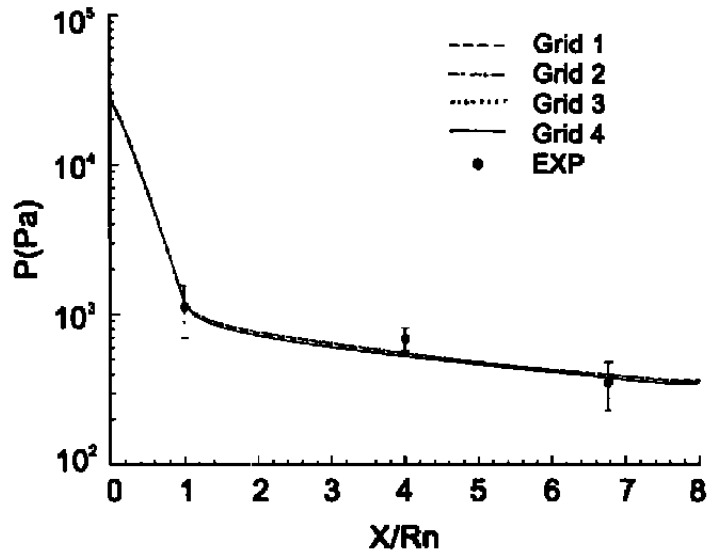
Figure 17. Pressure distributions for hemisphere/cylinder model 2 for grids 1, 2, 3, and 4.
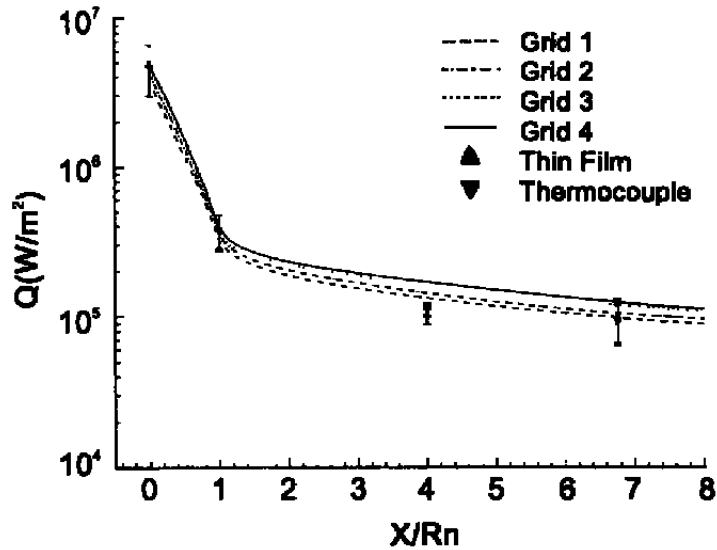
Figure 18. Heat-transfer distributions for hemisphere/cylinder model 2 for grids 1, 2, 3, and 4.

To assess the effects of even smaller viscous spacings, a second series of grid resolution computations was performed with viscous spacings approaching those recommended by Siddiqui et al. These grids are listed in Table 3 as grids 5, 6, and 7. Surface pressure and heat-transfer distributions for grids 5, 6, and 7 are presented in Figs. 19 and 20. The comparisons with experimental measurements for pressure are once again excellent. Furthermore, the calculation of surface pressure is largely independent of the grid used. The pressure distributions for all grids differed by less than 2 percent. The pressure distributions, as expected, also are in agreement with the results obtained from grids 1–4. The comparisons with experimental heat-transfer measurements for grids 5, 6, and 7 are similar. However, the heat-transfer distributions still exhibit a sensitivity to the viscous spacing. The stagnation-point values of heat transfer for grids 5 and 6 differ by approximately 20 and 10 percent, respectively, from those of grid 7. For grid 7, $y^+ \approx 0.10$ at the stagnation point. Downstream of the spherical surface, $y^+ \approx 0.15$. For grids 5 and 6, $y^+ \approx 0.15$ at the stagnation point. Downstream of the spherical surface, $y^+ \approx 0.20$. These results further demonstrate the difficulties in achieving truly grid-independent, heat-transfer predictions. However, these results coupled with the results of Sec. 5.2 also demonstrate that for the cases studied, grids with viscous spacings corresponding to $y^+ \approx 0.1$ produced heat-transfer predictions within the experimental scatter.
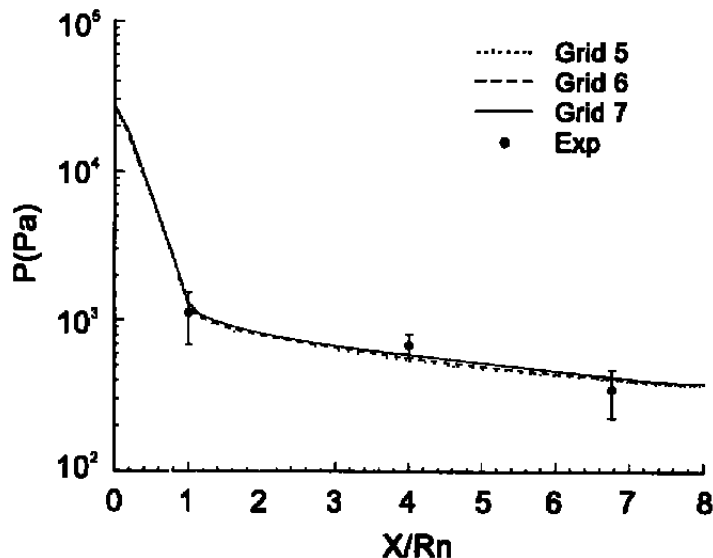
Figure 19. Pressure distributions for hemisphere/cylinder model 2 for grids 5, 6, and 7.
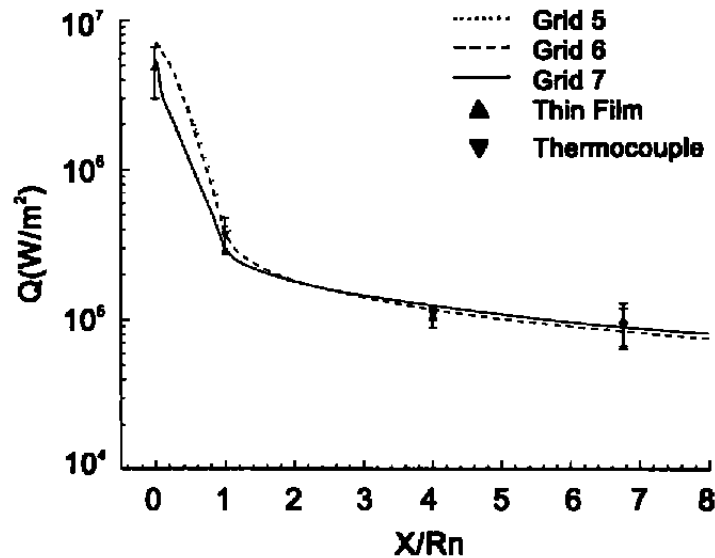
Figure 20. Heat-transfer distributions for hemisphere/cylinder model 2 for grids 5, 6, and 7.

The effects of viscous resolution on heat-transfer predictions have been well documented. However, the importance of resolving the shock layer should not be overlooked. This constraint is seen in the comparisons of surface heat transfer for grids 5 and 6. Both grids have the same initial viscous spacing. They only differ in the number of points and distribution of points normal to the body. The computed stagnation-point heat transfer for these two grids differs by approximately 8 percent, demonstrating the importance in resolving the shock layer. Also, the heat-transfer distributions for grids 5, 6, and 7 differ from those of grids 1–4 downstream of the hemisphere nose. However, instead of predicting an increased heat-transfer rate to the surface, they show a lower heat-transfer rate to the body. This trend is more in line with the experimental data. Siddiqui et al. (Ref. 59) state that this lower heat-transfer rate is due to a better resolution of the expansion waves emanating from the spherical region. This consequence of better resolving the expansion region of the flow further emphasizes the difficulties associated with accurate prediction of heat-transfer data.

Based on the results of the two grid resolution studies, the geometries of models 1, 2, and 3 were modeled with $51 \times 5 \times 75$ grids with initial viscous spacings of $5.0 \times (10)^{-7} m$. These viscous spacings produced values of $y^+ \approx 0.1$. Surface pressure and heat-transfer distributions for models 1, 2, and 3 are presented in Figs. 21–26. The surface pressure distributions are in excellent agreement with the experimental data for all three models. The agreement with the stagnation-point heat–transfer data is reasonable for all three models. The agreement with the heat-transfer data on the afterbodies is within the experimental data scatter. For model 3, both a fully catalytic wall and a

noncatalytic wall boundary condition were applied. The uncertainty in the stagnation-point heat-transfer measurement of model 3 is reported as zero because only one measurement was taken. Note that the fully catalytic wall increases the stagnation-point heat transfer by 58 percent over that of the noncatalytic wall. Generally, the model surface will exhibit finite catalytic rates. Therefore, the true heat-transfer distribution is bounded by the fully catalytic and noncatalytic values. Clearly, the accurate modeling of wall catalycity represents a significant challenge in the accurate prediction of surface heat transfer in both computational and experimental simulations.
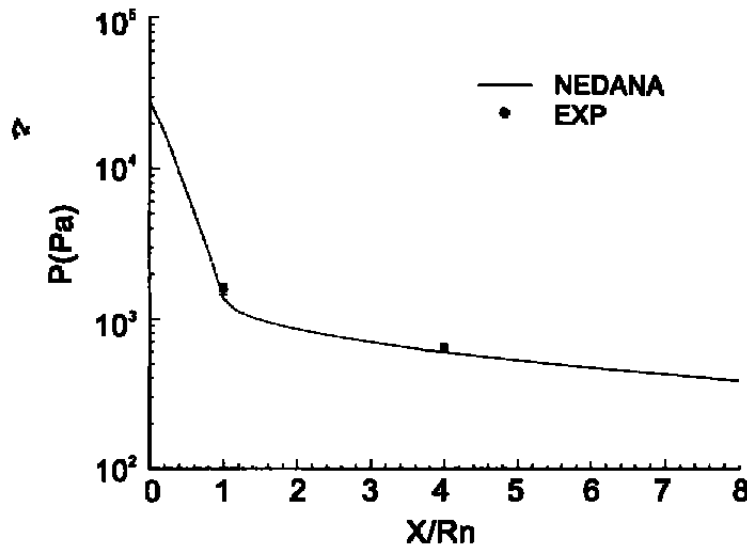
Figure 21. Pressure distributions for hemisphere/cylinder model 1.
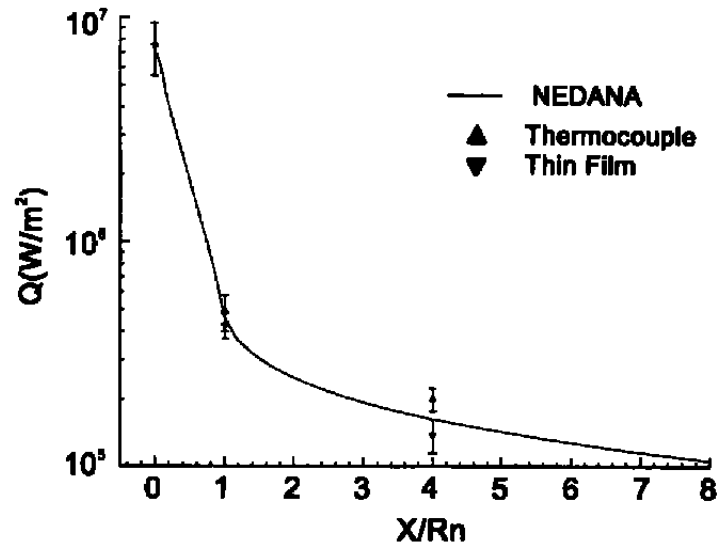
Figure 22. Heat-transfer distributions for hemisphere/cylinder model 1.
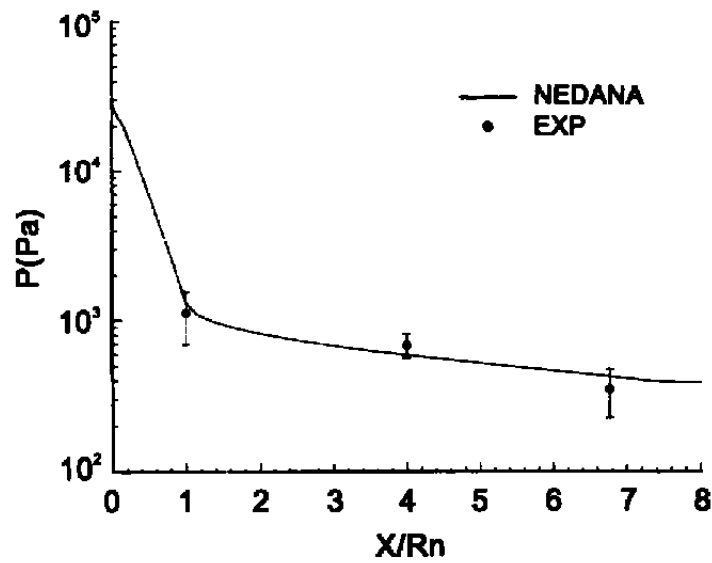
Figure 23. Pressure distributions for hemisphere/cylinder model 2.
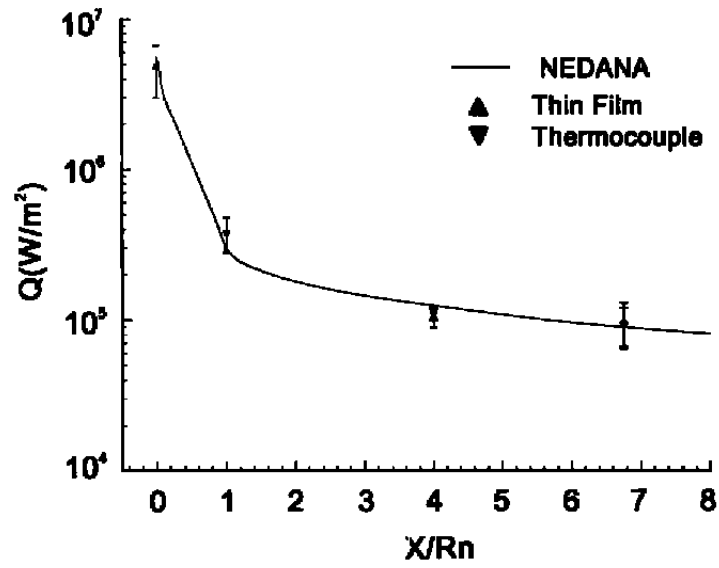
Figure 24. Heat-transfer distributions for hemisphere/cylinder model 2.
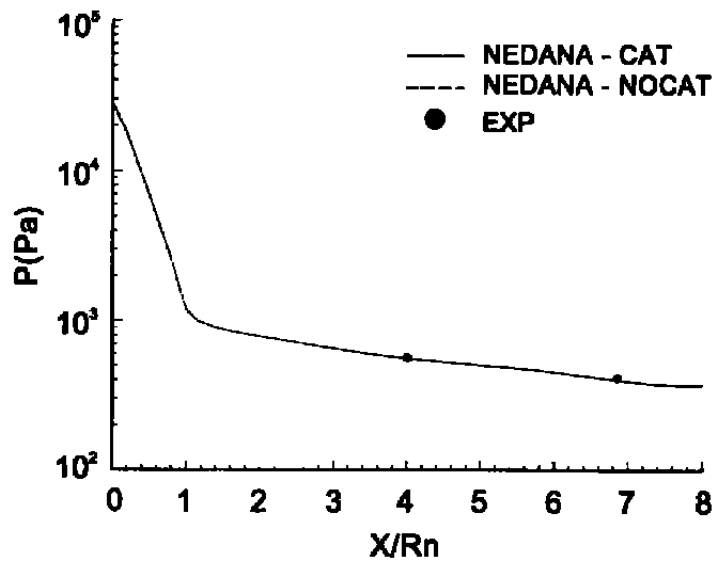
Figure 25. Pressure distributions for hemisphere/cylinder model 3.
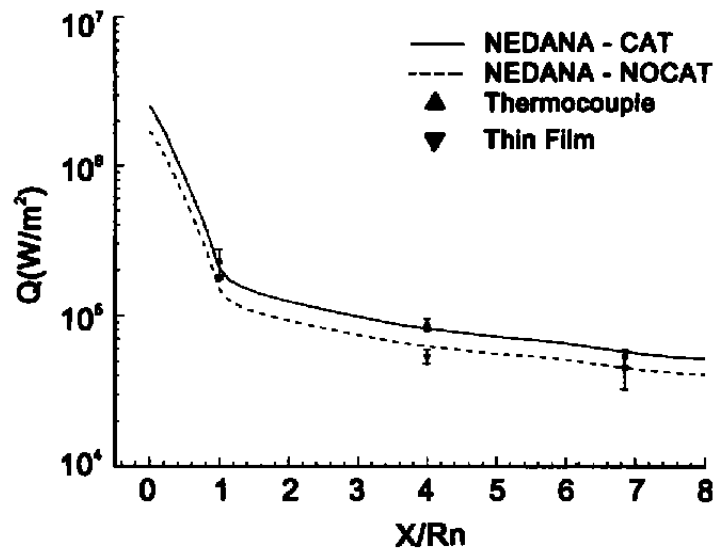
Figure 26. Heat-transfer distributions for hemisphere/cylinder model 3.

Temperature distributions along the stagnation streamline for models 1, 2, and 3 are presented in Fig. 27. The conditions directly behind the shock are determined by the free-stream conditions. Therefore, the peak post-shock temperatures for all three models are nearly the same. (Small differences in the post-shock temperatures may be attributed to differences in grid resolution.) Note, the translational temperature rises rapidly behind the shock. However, a much longer time is required for the vibrational modes of the molecules to become excited. As a result, the vibrational temperature lags the translational temperature, producing a state of thermal nonequilibrium. The time or distance that is required for the translational and vibrational temperatures to equilibrate is dependent on this initial departure from equilibrium, and is therefore similar for all three models. However, the shock-stand off distance for each model is proportional to the nose radius. Therefore, as the nose radius decreases, a larger extent of the shock layer is in a state of thermal nonequilibrium. Also, note that the peak post-shock temperature occurs closer to the body with decreasing nose radius. This condition produces steeper temperature gradients near the body, leading to increased heat-transfer rates. These findings are consistent with hypersonic boundary-layer theory (Ref. 60) which states that $q \propto 1/\sqrt{Rn}$.
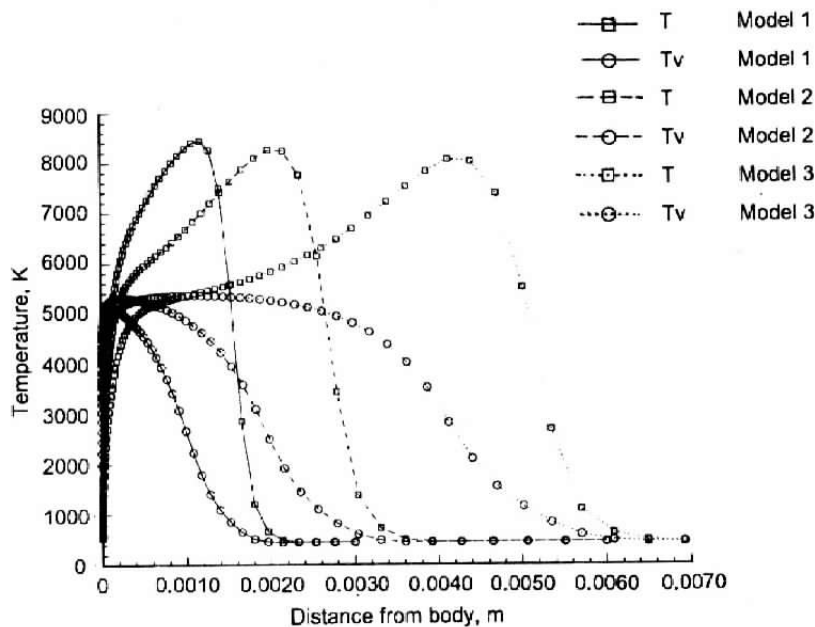
Figure 27. Temperature distributions along stagnation streamline for models 1, 2, and 3.

5.4 CHIMERA DOMAIN DECOMPOSITION

As a demonstration of the chimera capability of NEDANA, a computation for the hemisphere cylinder model 2 was made with the computational domain defined by two overlapping grids consisting of $45 \times 5 \times 75$ points on the forebody and $25 \times 5 \times 51$ points on the afterbody. The two-grid system is shown in Fig. 28. The two grids had different numbers of points and grid distributions in both directions. Therefore, there was no exact overlap (direct injection) of points between the two grids. The one grid constraint that was applied was that the first point off the wall for the two grids has the same viscous spacing. This constraint was applied because of the extreme dependence of heat-transfer results on viscous spacing. To facilitate the comparisons of the results obtained on a single grid, the two chimera grids were given initial viscous spacings equal to that of grid 1 in Table 3. Hence, comparisons are also made to the results of grid 1. Surface pressure and heat-transfer distributions for grid 1 and the chimera grid system are compared in Figs. 29 and 30. The distributions for the chimera grids are almost identical to those of grid 1 even with the mismatches in grid resolution. The pressure and heat-transfer distributions are also smooth in the overlap region between the forebody and afterbody grids.
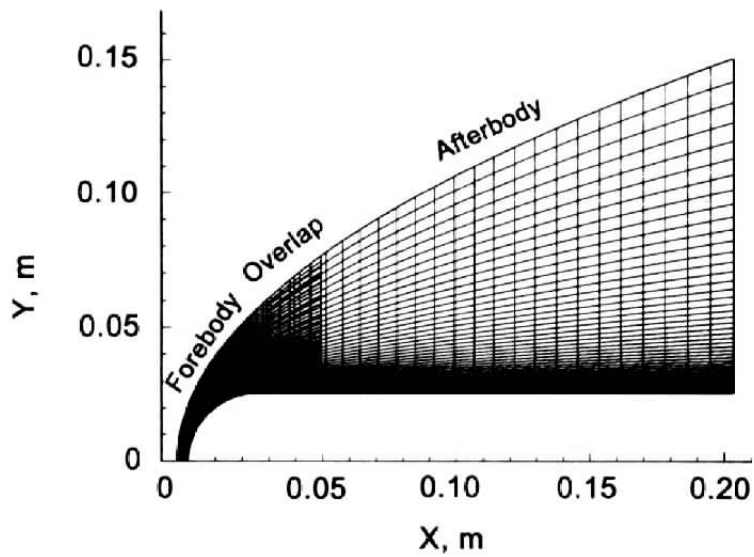
Figure 28. Chimera hemisphere/cylinder grid, $45 \times 5 \times 75$ and $25 \times 5 \times 51$.
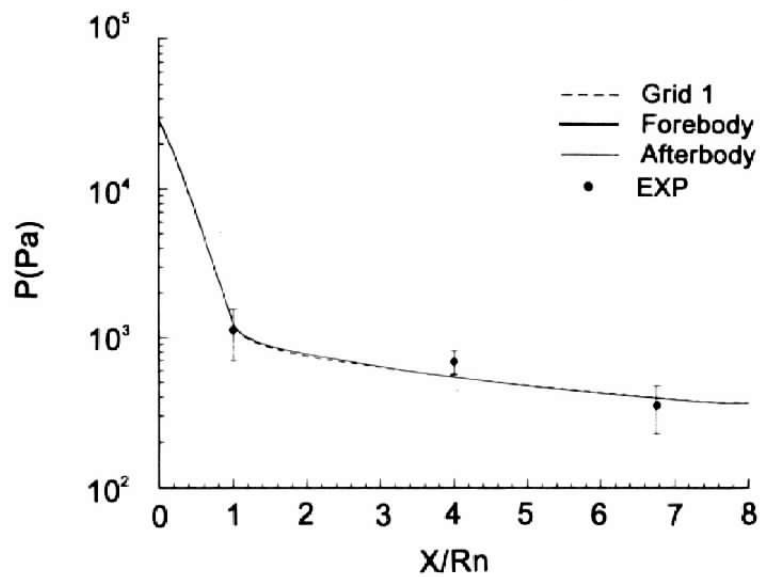
Figure 29. Pressure distributions for model 2 with single and chimera grid system.
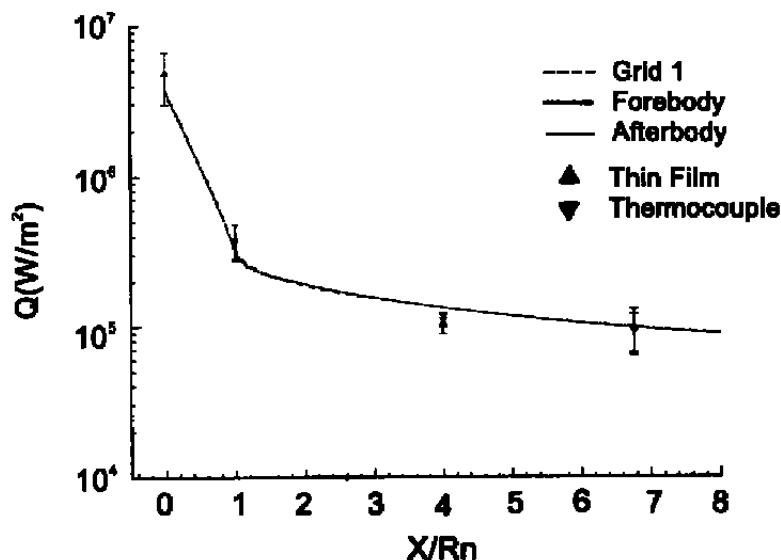
Figure 30. Heat-transfer distributions for model 2 with single and chimera grid system.

These results demonstrate the ability of the chimera grid system to reproduce the surface pressure and heat-transfer results of the single grid. However, questions have been raised about the applicability of the chimera scheme to hypersonic nonequilibrium flows, in particular, the ability of the scheme to capture strong shocks, as well as conserve species concentrations in the vicinity of grid overlaps. In Figs. 31 – 34, contour plots are presented for the translational-rotational and vibrational-electronic temperatures, and for the mass fractions of diatomic and monatomic oxygen. Contour lines are plotted on both grids in the overlap region. Therefore, any discrepancies in the temperatures or mass fractions between the grids should appear as mismatches in the contour lines. Small discrepancies are perceivable in the overlap region. They occur primarily in the plots of translational-rotational temperature and not in the plots of vibrational-electronic temperature or mass fractions.
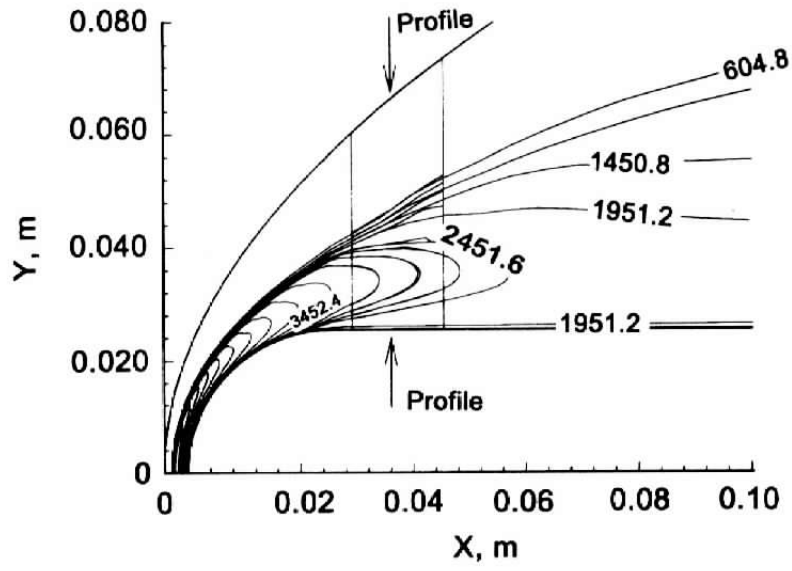
Figure 31. Translational-rotational temperature contours for chimera grid system.
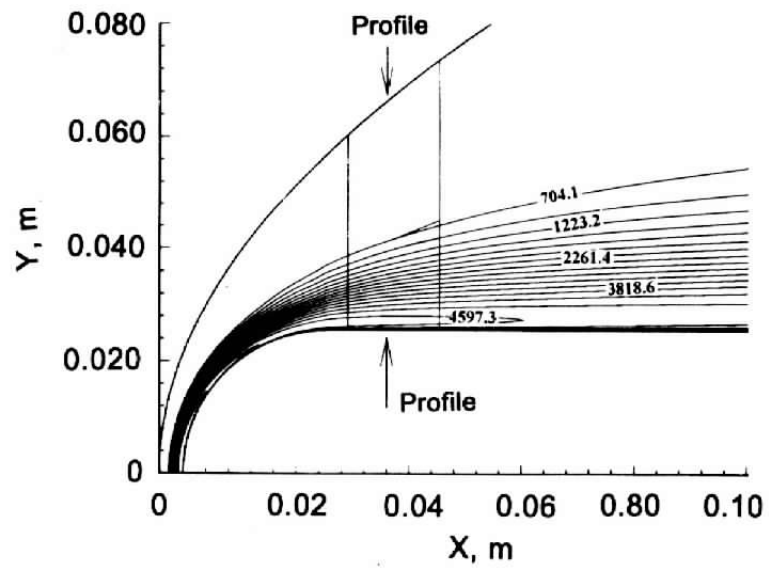
Figure 32. Vibrational-electronic temperature contours for chimera grid system.
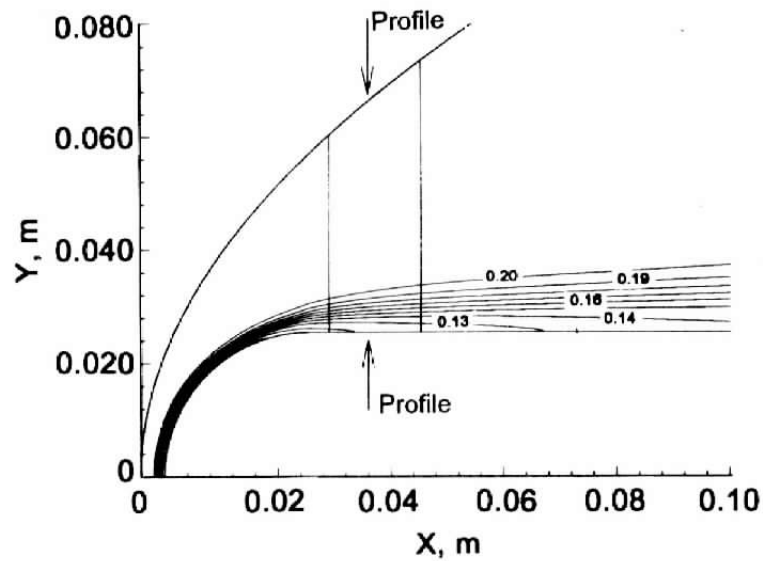
Figure 33. Mass fraction O_2 contours for chimera grid system.
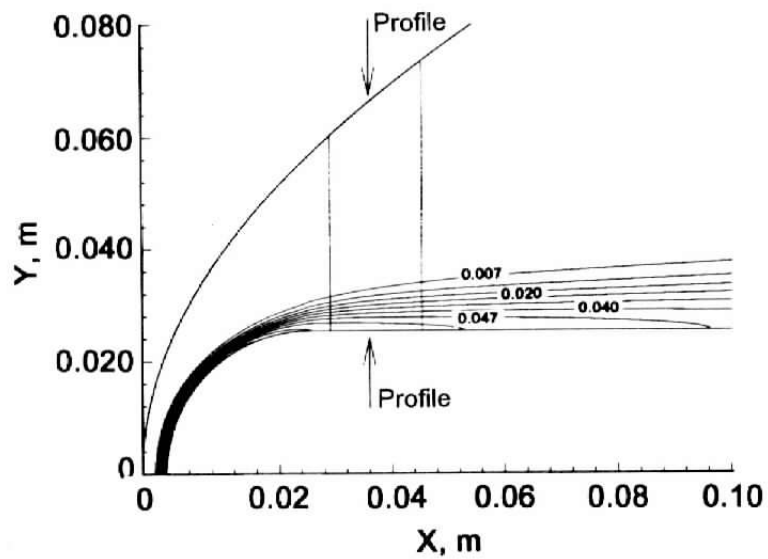
Figure 34. Mass fraction O contours for chimera grid system.

The contour plots provide a means for examining the qualitative properties of the chimera scheme in the overlap region. However, contour plots may be misleading because they depend on the contour levels chosen. Therefore, temperature and mass fraction profiles normal to the body at the location indicated by the arrows ($x \approx 0.036$) are presented in Figs. 35 and 36. The profiles extracted from the forebody and afterbody grids are nearly identical. Also, note the effects of both thermal and chemical nonequilibrium. The overlap region and the profile location extend from the free stream through the shock layer to the surface of the cylinder. Examining Fig. 35, the translational-rotational and vibrational-electronic temperatures are seen to be in equilibrium in the free stream. As the distance to the body decreases, the profiles correspond to a fluid element that crossed the oblique shock just upstream of the profile station. Therefore, the translation-rotational temperature increases while the vibrational-electronic temperature lags. This behavior is similar to the behavior along the stagnation line that was discussed in the previous section. The profiles at the stagnation line, by definition, correspond to a single streamline and shock crossing position. However, unlike the profile along the stagnation line, the current profiles correlate to many streamlines and shock crossing positions. As the distance to the body in Fig. 35 decreases further, the profile corresponds to fluid elements that have come through the much stronger shock of the stagnation region. These fluid elements have also been rapidly expanded around the hemisphere nose and are, to a great extent, vibrationally and chemically frozen. An examination of the temperature profiles near the surface show that the vibrational-electronic temperature is frozen at a much higher level than the translational-rotational temperature.

The effects of chemical nonequilibrium and freezing are seen in the mass fraction profiles of Fig. 36. The increase in the translational-rotational temperature that is a result of crossing the oblique shock is not accompanied by a change in the mass fractions of oxygen as is experienced at the stagnation line. This behavior is a result of the weaker oblique shock. The oblique shock produces lower temperature, and density rises relative to the shock at the stagnation region. The dissociation rates behind the oblique shock are, therefore, much slower. However, significant variations in the mass fractions are seen as the distance to the body decreases further. Near the body, the profiles correspond to fluid elements that have passed through the much stronger shock of the stagnation region and the subsequent expansion region. Therefore, the composition of the gas is partially frozen. This effect of chemical nonequilibrium is evident in the increased degree of dissociation of diatomic oxygen near the body. If the gas were in equilibrium at the local translational temperature, the degree of dissociation of the gas would be decreasing with decreasing temperature near the body.
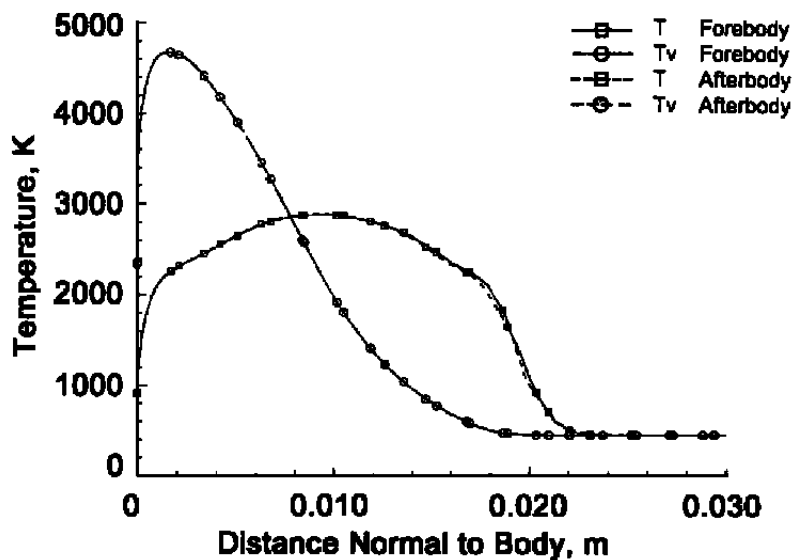
Figure 35. Temperature profiles in chimera overlap region.
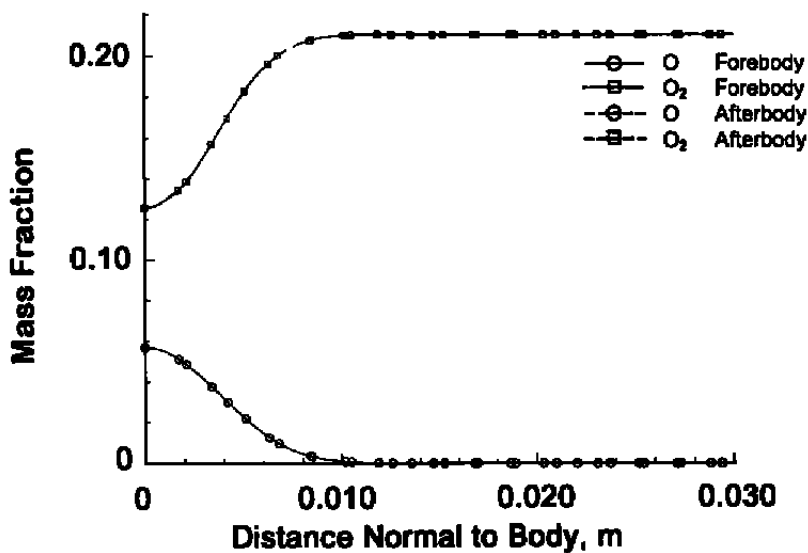
Figure 36. Mass fraction O_2 and O profiles in chimera overlap region.

6.0 CONCLUSION

A three-dimensional nonequilibrium chimera flow solver was developed and tested against existing flow solvers and experimental data. The present flow solver, NEDANA, uses an implicit, time-marching algorithm that is central differenced and made TVD (Total Variation Diminishing) through flux limiters. The LIM (Locally Implicit Method) scheme is used at each time step to obtain a solution to the nonlinear set of equations. Flexibility in the use of various nonequilibrium chemistry models is made possible by the availability of an AEDC-developed nonequilibrium chemistry package, NEQPAK. Use of such a chemistry package makes NEDANA unique in the field.

One-dimensional comparisons with the results from state-of-the art flow solvers were excellent. It was expected at the outset that sharper shocks in one-dimensional flows would be traded for a simpler algorithm, but this was not the case. The simpler algorithm (NEDANA) captured shocks as well as those of the more complex solvers. However, it is also evident that NEDANA does not handle contact surfaces as well. But, these surfaces only occur in unsteady flows, which are of somewhat less interest at AEDC. The three-dimensional NEDANA flow solver has been extensively tested against other flow solvers and available experimental data for perfect-gas and thermo-chemical nonequilibrium air chemistry. As expected, the NEDANA code proved to be slightly more dissipative than upwind schemes, but the effects of increased dissipation were marginal. A nonequilibrium chimera capability was also demonstrated, emphasizing the flexibility of the NEDANA methodology.

The present solver's simplicity helps achieve the goal of having solvers that are relatively easy to use, understand, and modify.

REFERENCES

1. Cable, A. J. "Upgrade of the Ballistic Range Facilities at AEDC: Status as of October 1993." *AIAA Paper 94-0542*, January 1994.

2. Maus, J. R., Laster, M. L., and Hornung, H. G. "The G-Range Impulse Facility - A High Performance Free-Piston Shock Tunnel." *AIAA Paper 92-3946*, July 1992.

3. Maus, J. R., Blanks, J. R., and DeWitt, J. R. "Calibration Tests of a New Free-Piston Shock Tunnel." *AIAA Paper 93-5003*, November 1993.

4. Blanks, J. R. and DeWitt, J. R. "Calibration Tests of AEDC Free-Piston Shock Tunnel." *AIAA Paper 94-2526*, June 1994.

5. Felderman, E. J., Chapman, R., and Jacocks, J. L. "Development of a High-Pressure, High-Power Arc Heater: Modeling Requirements and Status." *AIAA Paper 94-2658*, June 1994

6. Kraft, E. M. and Chapman, G. "A Critical Review of the Integration of Computations, Ground Tests, and Flight Tests for the Development of Hypersonic Vehicles." *AIAA Paper 93-5101*, November 1993.

7. Benek, J. A., Steger, J. L., Dougherty, F. C., and Buning, P. G. "Chimera: A Grid–Embedding Technique." AEDC-TR-85-64, December 1985.

8. Meakin, R. L. and Suhs, N. E. "Unsteady Aerodynamic Simulation of Multiple Bodies in Relative Motion." *AIAA Paper 89-1996*, June 1989.

9. Lijewski, L. E. and Suhs, N. E. "Chimera–Eagle Store Separation." *AIAA Paper 92-4569*, August 1992.

10. Sakell, L. "The Status of CFD: An Air Force Perspective." *AIAA Paper 93-3293*, June 1993.

11. Reddy, K. C. and Jacocks, J. L. "A Locally Implicit Scheme for the Euler Equations." *AIAA Paper 87-1144*, June 1987.

12. Nayani, S. N. "A Locally Implicit Scheme for the Navier–Stokes Equations." Ph.D. Dissertation, Univ. Tennessee, Knoxville, 1988.

13. Towne, M. C. "A Matrix–Free Locally Implicit Scheme for Navier–Stokes Equations." M. S. Thesis, Univ. Tennessee, Knoxville, 1989.

14. Reddy, K. C. and Benek, J. A. "A Locally Implicit Scheme for 3–D Compressible Viscous Flows." *AIAA Paper 90-1525*, June 1990.

15. Hwang, C. J. and Liu, J. L. "A Locally Implicit Total–Variation–Diminishing Scheme on Unstructured Triangular Meshes." *AIAA Journal*, Vol. 29, No. 10, 1991, pp. 1619–1626.

16. Tramel, R. W. "A Nonlinear Filter for Inviscid Fluid Flow Equations." M. S. Thesis, Univ. Tennessee, Knoxville, 1989.

17. Tramel, R. W., Keeling, S. L., and Fox, J. H. "A One–Dimensional Inviscid Nonequilibrium Flow Solver." *Developments in Theoretical and Applied Mechanics*, Volume XVI, Tullahoma TN, 1992, pp. III.II.48–55.

18.   Limbaugh, C. C., Tramel, R. W., Drakes, J., and Heirs, R., III. "Analysis of CO_2 Vibronic Ensembles of Nonequilibrium Combustion Flows." *AIAA Paper 94-1985*, June 1994.

19.   Bussing, T. R. A. and Murman E. A. "A Finite Volume Method for the Calculation of Compressible Chemically Reacting Flows." *AIAA Paper 85-0331*, January 1985.

20.   Eberhardt S. and Imlay S. "A Diagonal Implicit Scheme for Computing Flows with Finite–Rate Chemistry." *AIAA Paper 90-1577*, June 1990.

21.   Gnoffo, P. A. "An Upwind–Biased, Point–Implicit Relaxation Algorithm for Viscous, Compressible Perfect–Gas Flows." *NASA TP-2953*, February 1990.

22.   Gnoffo, P. A. "Asynchronous, Macrotasked Relaxation Strategies for the Solution of Viscous, Hypersonic Flows." *AIAA Paper 91-1579*, June 1991.

23.   Curtis J. T. and Tramel, R. W. "NEQPAK, The AEDC Thermochemical Nonequilibrium Package–Theory and Use." AEDC-TR-93-20, March 1994.

24.   Hirschfelder, J.O., Curtiss, C. F., and Bird, R.B. *Molecular Theory of Gases and Liquids.* Second Printing, John Wiley & Sons, New York, 1963

25.   Lee, J. H. "Basic Governing Equations for the Flight Regimes of Aeroassisted Orbital Transfer Vehicles." *Thermal Design of Aeroassisted Orbital Transfer Vehicles*, Nelson, H., F., Ed., Vol.96, *Progress in Astronautics and Aeronautics*, AIAA, 1985.

26.   Gnoffo, P. A., Gupta, R. N., and Shinn, J. L. "Conservation Equations and Physical Models for Hypersonic Air Flows in Thermal and Chemical Nonequilibrium." *NASA TP-2867*, February 1989.

27.   Gupta, R. N., Yos, J. M., Thompson, R. A., and Lee, K. "A Review of Reaction Rates and Thermodynamic and Transport Properties for the 11–Species Air Model for Chemical and Thermal Nonequilibrium Calculations to 30,000 K." *NASA RP-1232*, February 1989.

28.   Armaly, B. F. and Sutton, K. "Viscosity of Multicomponent Partially Ionized Gas Mixtures." *AIAA Paper 80-1495*, July 1980.

29.   Armaly, B. F and Sutton, K. "Thermal Conductivity of Partially Ionized Gas." *AIAA Paper 81-1174*, June 1981.

30. Williams, F. A. *Combustion Theory.* The Benjamin/Cummings Publishing Company, Inc. California, 1985.

31. Curtiss, C. F. and Hirschfelder, J. O. "Transport Properties of Multicomponent Gas Mixtures." *Journal Chemical Physics,* Vol. 17, No. 6, June 1949.

32. Vincenti, W. G. and Kruger, C. H., Jr. *Introduction to Physical Gas Dynamics.* John Wiley and Sons, New York, 1965.

33. Park, C. "Assessment of Two–Temperature Kinetic Model for Dissociating and Weakly Ionizing Nitrogen."*Journal of Thermophysics and Heat Transfer,* Vol. 2, No. 1, 1988, pp. 8–16.

34. Landau, L. and Teller, E. "Zur Theorie der Schalldispersion." *Physik Z. Sowjetunion,* band 10, heft 1, 1934.

35. Millikan, R. C. and White, D. R. "Systematics of Vibrational Relaxation." *Journal Chemical Physics,* Vol. 39, No. 12, December 15, 1963.

36. Park, C. "Convergence of Computation of Chemical Reacting Flows." in *Thermal Design of Aeroassisted Orbital Transfer Vehicles,* Nelson, H. F., Ed., Vol. 96, *Progress in Astronautics and Aeronautics,* AIAA, 1985.

37. Vinokur, M. "An Analysis of Finite-Difference and Finite-Volume Formulations of Conservation Laws." *Journal of Computational Physics,* Vol. 81, 1989, pp. 1–52.

38. Jameson, A. "*A Nonoscillatory Shock Capturing Scheme Using Flux Limited Dissipation.*" Lectures in Applied Mathematics, Vol. 22, Part I, AMS, 1985, pp. 345–370.

39. Yoon, S. and Kwak, D. "Artificial Dissipation Models for Hypersonic External Flow." *AIAA Paper 88-3277,* July 1988.

40. Benek, J. A., Steger, J. L., and Dougherty, F. C. "A Flexible Grid Embedding Technique with Applications to the Euler Equations." *AIAA Paper 83-1944,* July 1983.

41. Benek, J. A., Buning, P. G., and Steger, J. L. "A 3–D Chimera Grid Embedding Technique." *AIAA Paper 85-1523,* July 1985.

42. Benek, J. A., Donegan, T. L., and Suhs, N. E. "Extended Chimera Grid Embedding Scheme with Applications to Viscous Flow." *AIAA Paper 87-1126,* June 1987.

43. Dougherty, F. C., Benek, J. A., and Steger, J. L. "On Applications of Chimera Grid Scheme to Store Separation." *NASA-TM-88193*, October 1985.

44. Suhs, N. E. and Tramel, R. W. "PEGSUS 4.0 User's Manual." AEDC-TR-91-1, November 1991.

45. Ortega, J. M. and Rheinboldt, W. C. *Iterative Solution of Nonlinear Equations in Several Variables.* Academic Press, Inc., New York, 1970.

46. Ortega, J. M. and Voigt, R. G. "Solution of Partial Differential Equations on Vector and Parallel Computers." *SIAM Review,* Vol. 27, No. 2, 1985, pp. 149–240.

47. Shuen, J., Liou, M., and van Leer, B. "Inviscid Flux-Splitting Algorithms for Real Gases with Nonequilibrium Chemistry." *Journal of Computational Physics,* Vol. 90, 1990, pp. 371–395.

48. Prabhu, R. K. and Erickson, W. D. "A Rapid Method for the Computation of Equilibrium Chemical Composition of Air to 15000 K." NASA TP-2792, 1988.

49. Molvik, G. A. and Merkle, C. L. "A Set of Strongly Coupled, Upwind Algorithms for Computing Flows in Chemical Nonequilibrium." *AIAA Paper 89-0199,* January 1989.

50. Dunn, M. G. and Kang, S. "Theoretical and Experimental Studies of Reentry Plasmas." NASA CR-2232, 1973.

51. Blottner, F. G. "Viscous Shock Layer at the Stagnation Point with Nonequilibrium Air Chemistry." *AIAA Journal,* Vol. 7, No. 12, 1969, pp. 2281–2288.

52. Park, C. *Nonequilibrium Hypersonic Aerothermodynamics.* John Wiley & Sons Inc., New York, 1990.

53. Holden, M.S. and Moselle, J. R. "A Database of Aerothermal Measurements in Hypersonic Flow for CFD Validation."" *AIAA Paper 92-4023,* July 1992.

54. Hung, C. M. and MacCormack, R. W. "Numerical Solutions of Supersonic and Hypersonic Laminar Compression Corner Flows." *AIAA Journal,* Vol. 14, No. 4, 1976, pp. 475–481.

55. Rudy, D. H., Thomas, J. L., et al. "Computation of Laminar Hypersonic Compression–Corner Flows," *AIAA Journal,* Vol. 29, No. 7, 1991, pp. 1108–1113.

56. Gaitonde, D. and Shang, J. S. "Accuracy of Flux-Split Algorithms in High-Speed Viscous Flows" *AIAA Journal*, Vol. 31, No. 7, 1993, pp. 1215–1221.

57. Josyula, E. and Shang, J. S. "Computation of Nonequilibrium Hypersonic Flowfields Around Hemisphere Cylinders" *Journal of Thermophysics and Heat Transfer*, Vol. 7, No. 4, October–December 1993, pp. 668–679.

58. Cassady, P. Barr, D., and Shelton, D. "Reacting Gas Experimental Data in Low Density Flow; Task III Model Flowfield Experimental Surveys" WL-TR-91-3077, Wright–Patterson AFB, OH, January 1992.

59. Siddiqui, M. S., Hoffmann, K. A., Chiang, S. T., and Rutledge, W. H. "A Comparative Study of the Navier Stokes Solvers with Emphasis on the Heat Transfer Computations of High Speed Flows." *AIAA Paper 92-0835*, January 1992.

60. Anderson, J. D., Jr. *Hypersonic and High Temperature Gas Dynamics*. McGraw-Hill, New York, 1989.

61. LeVeque, R. J. *Numerical Methods for Conservation Laws*. Berkhauser Verlag, Basel, 1990.

62. Lax, P. D. *Hyperbolic Systems of Conservation Laws and the Mathematical Theory of Shock Waves*. SIAM, Philadelphia, 1972.

63. Harten, A. "On a Class of High Resolution Total Variation Stable Finite Difference Schemes." *SIAM Journal of Numerical Analysis*, Vol. 21, 1984, pp. 1–21.

64. Jameson, A. and Lax, P. D. "Conditions for the Construction of Multi-Point Total Variation Diminishing Difference Schemes." *Applied Numerical Mathematics*, Vol. 2, 1986, pp. 335–345.

65. Yee, H. C. "Construction of Explicit and Implicit Symmetric TVD Schemes and Their Applications." *Journal of Computational Physics*, Vol. 68, 1987, pp. 151–179.

66. Gudonov, S. K. "A Difference Scheme for Numerical Computation of Discontinuous Solutions of Equations of Fluid Dynamics." *Mat. Sb.*, Vol. 47, 1959, pp. 271–290.

67. van Leer, B. "Towards the Ultimate Conservation Difference Scheme V, A Second-Order Sequel to Godunov's Method." *Journal of Computational Physics*, Vol. 32, 1979, pp. 101–136.

68. Roe, P. L. "Approximate Riemann Solvers, Parameter Vectors, and Difference Schemes." *Journal of Computational Physics*, Vol. 43, 1981, pp. 357–372.

69. Liu, Y. and Vinokur, M. "Nonequilibrium Gas Flow Computations. I. An Analysis of Numerical Formulations of Conservation Laws." NASA CR-177489, June 1988.

70. von Neumann, J. and Richtmyer, R. D. "A Method for the Numerical Calculations of Hydrodynamical Shocks." *Journal of Applied Physics*, Vol. 21, 1950, pp. 232–237.

71. Deese, J. E. and Agarwal, R. K. "Three-Dimensional Hypersonic Navier-Stokes Calculations Using Central-Difference Methods with Adaptive Dissipation." AIAA-90-3069, 1990.

72. Van Dyke, M. "Slow Variations in Continuum Mechanics." *Advances in Applied Mechanics*, Vol. 25, 1987, pp. 1–45.

73. Apostol, T. M. *Mathematical Analysis*. Addison-Wesley, Menlo Park, 1974.

APPENDIX A
DERIVATION OF MODELING EQUATIONS

The purpose of this appendix is to begin with very few simplifying assumptions, and to develop a rather general set of conservation equations modeling viscous nonequilibrium flow. Then, various assumptions are made to obtain a simplified, reduced equation set from the more general.

First, the internal energy per unit mass, e_s, of a given species, s, is assumed to be composed as follows:

$$\epsilon_s = \epsilon_{t,s} + \epsilon_{r,s} + \epsilon_{v,s} + \epsilon_{e,s}, \qquad s = 1, \ldots, ns$$

where $e_{t,s}$, $e_{r,s}$, $e_{v,s}$ and $e_{e,s}$ are translational, rotational, vibrational, and electronic parts, respectively. Also, ns is the total number of species. Each of the above energies has an associated temperature. Specifically, in thermodynamic equilibrium, the most probable fractions, $f_{q,s}^{(i)}$, $q = t, r, v, e$, of the particles of a given species, s, at the discrete energies, $e_{q,s}^{(i)}$, $q = t, r, v, e$, respectively, are described by Boltzmann distributions,

$$f_{q,s}^{(i)} = \frac{d_{q,s}^{(i)}}{Z_{q,s}} \exp\left(-\frac{\epsilon_{q,s}^{(i)}}{kT_{q,s}}\right), \qquad q = t, r, v, e, \qquad s = 1, \ldots, ns$$

with temperatures, $T_{q,s}$, $q = t, r, v, e$, respectively. Here, i is an index over discrete energy states. Also, $d_{q,s}^{(i)}$ is the number of distinct states with energy, $e_{q,s}^{(i)}$, and $Z_{q,s}$ is the partition function,

$$Z_{q,s} = \sum_j d_{q,s}^{(j)} \exp\left(-\frac{e_{q,s}^{(j)}}{kT_{q,s}}\right).$$

The Boltzmann constant is $k = \mathcal{R}/N_A$, where $\mathcal{R}$ is the universal gas constant and N_A is Avagadro's number. To obtain the four energies for the mixture, a mass average is performed:

$$\epsilon_q = \sum_{s=1}^{ns} \frac{\rho_s}{\rho} \epsilon_{q,s}, \qquad q = t, r, v, e.$$

Here, ρ_s is the partial density of species, s, and ρ is the mixture density given by the sum of the partial densities. Also, the mixture internal energy is given by:

$$e = \sum_{s=1}^{ns} \frac{\rho_s}{\rho} e_s.$$

In contrast to the species that have an internal structure, the free electron has only one form of energy, namely translational energy. Specifically,

$$\epsilon_{e^-} = \epsilon_{t,e^-}, \qquad \epsilon_{r,e^-} = \epsilon_{v,e^-} = \epsilon_{e,e^-} = 0. \tag{A-1}$$

Also, because elemental species do not have components that vibrate with respect to each other,

$$\epsilon_{v,s} = 0, \qquad s \neq \text{molecule.} \tag{A-2}$$

Similarly, the enthalpy per unit mass, h_s, for a given species, s, is assumed to be the sum of translational, rotational, vibrational, and electronic parts:

$$h_s = h_{t,s} + h_{r,s} + h_{v,s} + h_{e,s}. \qquad s = 1, \ldots, ns.$$

These are related to the internal energies according to

$$h_{q,s} = \begin{cases} \epsilon_{q,s} & q \neq t \\ \epsilon_{t,s} + \dfrac{\mathcal{R}T_{t,s}}{\mathcal{M}_s} & q = t \end{cases} \tag{A-3}$$

where $\mathcal{M}_s$ is the molecular weight of species, s. Thus, by Eq. (A-1), the free electron has only one form of enthalpy:

$$h_{e^-} = h_{t,e^-}, \qquad h_{r,e^-} = h_{v,e^-} = h_{e,e^-} = 0. \tag{A-4}$$

Also, by Eq. (A-2),

$$h_{v,s} = 0, \qquad s \neq \text{molecule.} \tag{A-5}$$

To obtain the four enthalpies for the mixture, a mass average is performed:

$$h_q = \sum_{s=1}^{ns} \frac{\rho_s}{\rho} h_{q,s}, \qquad q = t, r, v, e.$$

Then, the mixture enthalpy is given by:

$$h = \sum_{s=1}^{ns} \frac{\rho_s}{\rho} h_s.$$

The energies and their associated temperatures are related by specific heats according to:

$$\epsilon_{q,s} = \int_{T_{ref}}^{T_{q,s}} C_{v,q}^{s}(T')dT' + (\epsilon_{q,s})_{ref}, \qquad q = t, r, v, e, \quad s = 1, \ldots, ns.$$

Also, the enthalpies and the temperatures are related by:

$$h_{q,s} = \int_{T_{ref}}^{T_{q,s}} C_{p,q}^{s}(T')dT' + (h_{q,s})_{ref}, \qquad q = t, r, v, e, \quad s = 1, \ldots, ns.$$

Here, $C_{v,q}^{s}$ and $C_{p,q}^{s}$ are specific heats per unit mass at constant volume and pressure, respectively. From statistical mechanical considerations it can be shown that (Ref. 32)

$$C_{v,q}^{s} = \frac{\mathcal{R}}{\mathcal{M}_s} \frac{\partial}{\partial T_{q,s}} \left[T_{q,s}^2 \frac{\partial \ln Z_{q,s}}{\partial T_{q,s}} \right], \qquad q = t, r, v, e, \quad s = 1, \ldots, ns. \qquad \text{(A-6)}$$

Then, by Eq. (A-3), it follows that:

$$C_{p,q}^{s} = \begin{cases} C_{v,q}^{s} & q \neq t \\ C_{v,q}^{s} + \dfrac{\mathcal{R}}{\mathcal{M}_s} & q = t \end{cases} \qquad \text{(A-7)}$$

As with the energies and enthalpies, the specific heats, C_V^s and C_p^s, for a given species, s, are assumed to be the sum of translational, rotational, vibrational, and electronic parts:

$$C_v^s = C_{v,t}^s + C_{v,r}^s + C_{v,v}^s + C_{v,e}^s,$$
$$C_p^s = C_{p,t}^s + C_{p,r}^s + C_{p,v}^s + C_{p,e}^s, \qquad s = 1, \ldots, ns. \qquad \text{(A-8)}$$

To obtain the mixture specific heats for the different modes, a mass average is performed:

$$C_{v,q} = \sum_{s=1}^{ns} \frac{\rho_s}{\rho} C_{v,q}^s, \qquad C_{p,q} = \sum_{s=1}^{ns} \frac{\rho_s}{\rho} C_{p,q}^s, \qquad q = t, r, v, e.$$

Then, the mixture specific heats are given by:

$$C_v = \sum_{s=1}^{ns} \frac{\rho_s}{\rho} C_v^s, \qquad C_p = \sum_{s=1}^{ns} \frac{\rho_s}{\rho} C_p^s.$$

In complete thermal equilibrium, when all temperatures are equal, say $T_{s,q} = T$, Eqs. (A-6) and (A-7) can be evaluated explicitly to give the species specific heats according to Eq. (A-8). The following interpolation is used to approximate this calculation as a function of the equilibrium temperature:

$$C_p^s(T) = \frac{\mathcal{R}}{\mathcal{M}_s} \sum_{i=1}^{5} a_{i,s} T^{i-1} \qquad C_v^s(T) = \frac{\mathcal{R}}{\mathcal{M}_s} \sum_{i=1}^{5} a_{i,s} T^{i-1} - \frac{\mathcal{R}}{\mathcal{M}_s}. \qquad \text{(A-9)}$$

Also, in certain cases where the temperatures are distinct, explicit calculations can be performed easily to obtain the specific heats. For example, the translational and rotational specific heats are independent of temperature:

$$C_{v,t}^{'s} = \frac{3\mathcal{R}}{2\mathcal{M}_s}, \qquad C_{p,t}^{'s} = \frac{5\mathcal{R}}{2\mathcal{M}_s}. \qquad \text{(A-10)}$$

$$C_{v,r}^{'s} = \frac{r_s \mathcal{R}}{2\mathcal{M}_s} = C_{p,r}^{'s}. \qquad \text{(A-11)}$$

Here, r_s is the number of rotational degrees of freedom for a species, s. In particular, for diatomic molecules, $r_s = 2$. Next, though it requires more effort, the electronic specific heats can be calculated from Eq. (A-6) after tabulating a sufficient number, say I_s, of energy levels, $e_{e,s}^{(i)}$, and degeneracies, $d_{e,s}^{(i)}$. The result is:

$$C_{v,e}^{s} = C_{p,e}^{'s} = \frac{\mathcal{R}}{\mathcal{M}_s} \frac{1}{Z_{e,s}} \sum_{i=1}^{I_s} d_{e,s}^{(i)} \left(\frac{e_{e,s}^{(i)}}{kT_{e,s}} \right)^2 \exp\left(-\frac{e_{e,s}^{(i)}}{kT_{e,s}} \right)$$

$$-\frac{\mathcal{R}}{\mathcal{M}_s} \left[\frac{1}{Z_{e,s}} \sum_{i=1}^{I_s} d_{e,s}^{(i)} \left(\frac{e_{e,s}^{(i)}}{kT_{e,s}} \right) \exp\left(-\frac{e_{e,s}^{(i)}}{kT_{e,s}} \right) \right]^2. \qquad \text{(A-12)}$$

Finally, because of the complexity of calculating the vibrational specific heats by Eq. (A-6) for real molecules, the following approximation is used:

$$C_{v,v}^{s} = C_v^s(T_{v,s}) - C_{v,t}^s(T_{v,s}) - C_{v,r}^s(T_{v,s}) - C_{v,e}^s(T_{v,s})$$

$$= C_v^s(T_{v,s}) - \frac{(3 + r_s)\mathcal{R}}{2\mathcal{M}_s} - C_{v,e}^s(T_{v,s}) \qquad \text{(A-13)}$$

$$C_{p,v}^{'s} = C_{v,v}^{'s}.$$

Here, the nonvibrational parts are subtracted away from the total specific heat for the species, after evaluating all these specific heats at the vibrational temperature in Eqs. (A-9) – (A-12).

Since the free electron has only translational energy or enthalpy, its specific heats have only a translational part. Thus, with $s = e^-$, Eq. (A-8) becomes:

$$C_v^{\prime e^-} = C_{v,t}^{e^-} = \frac{3\mathcal{R}}{2\mathcal{M}_s}, \qquad C_p^{e^-} = C_{p,t}^{\prime e^-} = \frac{5\mathcal{R}}{2\mathcal{M}_s}. \tag{A-14}$$

For the temperatures, $T_{q,s}$, $q = t, r, v, e$, there are associated thermal conductivities, $\kappa_{q,s}$, $q = t, r, v, e$, respectively. First, the translational thermal conductivities are given by

$$\kappa_{t,s} = \frac{15}{4} \frac{\mathcal{R}}{\sigma_s^2 \Omega_{s,s}^{(2,2)}(T_{t,s})} \sqrt{\frac{T_{t,s}}{\mathcal{M}_s}}. \tag{A-15}$$

Here, σ_s is the collision diameter for the pure species, s, and Ω is the collision integral defined as the weighted average of a collision cross section of the form

$$\pi \Omega_{s,r}^{(l,l')}(T) = \frac{\int_0^\infty \int_0^\pi 4\pi \sigma_{sr}(\chi, g) e^{-\gamma^2} \gamma^{2l'+3}(1 - \cos^l \chi) \sin \chi \, d\chi \, d\gamma}{\int_0^\infty \int_0^\pi e^{-\gamma^2} \gamma^{2l'+3}(1 - \cos^l \chi) \sin \chi \, d\chi \, d\gamma},$$

$$g = \left[\frac{\mathcal{M}_s \mathcal{M}_r}{2\mathcal{R}T(\mathcal{M}_s + \mathcal{M}_r)}\right]^{-\frac{1}{2}} \gamma. \tag{A-16}$$

Here, σ_{sr} is the collision cross section for the s-r collision pair, χ is the scattering angle in the center of mass system, g is the relative velocity of the colliding particles, and γ is the reduced velocity. The expression in Eq. (A-15) is approximated within NEQPAK (Ref. 23) by the following interpolation:

$$\kappa_{t,s} = \frac{1.5}{4} \frac{\mathcal{R}}{\mathcal{M}_s} \exp\left[\sum_{i=1}^{5} b_{i,s} (\ln T_{t,s})^{5-i}\right]. \tag{A-17}$$

The other thermal conductivities are given by:

$$\kappa_{q,s} = \rho_s \mathcal{D}_s C_{p,q}^s, \qquad q = r, v, e. \tag{A-18}$$

Here,

$$\mathcal{D}_s = \mathcal{D}_{ss}(T_{t,s})$$

is the self-diffusion coefficient, where, in general, the binary diffusion coefficient is given in terms of a temperature, T, as:

$$\mathcal{D}_{sr}(T) = \frac{3kT^{\frac{3}{2}}}{8p\Omega_{s,r}^{(1,1)}(T)} \sqrt{\frac{\mathcal{R}(\mathcal{M}_s + \mathcal{M}_r)}{2\pi \mathcal{M}_s \mathcal{M}_r}}. \tag{A-19}$$

This expression is approximated within NEQPAK (Ref. 23) by the interpolation,

$$\mathcal{D}_{sr}(T) = 10.1325\frac{S_{sr}(T)}{p}\exp\left[\sum_{i=1}^{4} d_i^{s,r}\,(\ln T)^{4-i}\right]$$

(A-20)

where $S_{sr}(T)$ is the electrostatic shielding ratio (Ref. 27),

$$S_{sr}(T) = \begin{cases} 1 & s \text{ and } r \text{ neutral} \\[2ex] \dfrac{1}{\ln \Lambda\left(Tp_e^{-\frac{1}{4}}\right)} & s \text{ or } r \text{ charged} \end{cases}$$

and the shielding function $\Lambda(T)$ is defined as

$$\Lambda(T) = \sqrt{\frac{2.09}{10^{14}}\left(\frac{T^4}{p_{e-}}\right) + \frac{1.52}{10^{12}}\left(\frac{T^4}{p_{e-}}\right)^{\frac{2}{3}}}$$

and p_{e-} is the partial pressure of the electron in *atm*. In case a collection of species has the same temperature for a given energy mode, an associated mixture thermal conductivity can be defined in terms of thermal conductivities for the pure species. Specifically, suppose all species but the free electron have the same translational temperature, T. Then, the translational thermal conductivity for this mixture is given by:

$$\kappa_t = \frac{4}{\det \{L_{sr}\}_{s,r\neq e-}}\det\begin{bmatrix} L_{11} & \cdots & L_{1,ns} & \chi_1 \\ \vdots & \ldots L_{sr} \ldots & \vdots & \vdots \\ & & & \chi_s \\ & & & \vdots \\ L_{ns,1} & \cdots & L_{ns,ns} & \chi_{ns} \\ \chi_1 & \cdots \chi_r \cdots & \chi_{ns} & 0 \end{bmatrix}_{s,r\neq e-}.$$

Here the terms L_{sr} depend on the pure species thermal conductivities, but the explicit form is given below only for the diagonal terms to fully specify the approximation,

$$\kappa_t = -4 \sum_{s\neq e-} \frac{\chi_s^2}{L_{ss}}.$$

(A-21)

where χ_s is the mole fraction of species, s. The diagonal terms are given by

$$L_{ss} = -4\frac{\chi_s^2}{\kappa_{t,s}} - \sum_{r\neq s}\frac{\chi_s \chi_r \left(\frac{15}{2}\mathcal{M}_s^2 + \frac{5}{2}\mathcal{M}_r^2 + 4\mathcal{M}_r\mathcal{M}_s A_{sr}\right)}{\sqrt{2}(\mathcal{M}_r + \mathcal{M}_s)^{\frac{3}{2}} A_{sr}}\left[\frac{\mathcal{M}_r^{\frac{1}{2}}}{\kappa_{t,s}^{\frac{1}{2}}}F_{sr} + \frac{\mathcal{M}_s^{\frac{1}{2}}}{\kappa_{t,r}^{\frac{1}{2}}}B_{sr}\right]^2$$

where in general,

$$A_{sr} = \frac{\Omega_{s,r}^{(2,2)}(T)}{\Omega_{s,r}^{(1,1)}(T)}, \qquad F_{sr} = \sqrt{\frac{\Omega_{s,r}^{(2,2)}(T)}{\Omega_{s,s}^{(2,2)}(T)}}, \qquad B_{sr} = \sqrt{\frac{\Omega_{s,r}^{(2,2)}(T)}{\Omega_{r,r}^{(2,2)}(T)}}.$$

Following the method of Armaly and Sutton (Ref. 29), these terms are approximated as follows:

$$A_{sr} = A_{rs} = \begin{cases} 0.18 & s = H, r = H^+ \\ 0.025 & s = He, r = He^+ \\ 1.10 & s = \text{atom} \neq H, He, r = s^+ \\ 1.25 & \text{otherwise} \end{cases} \cdot \tag{A-22}$$

and

$$F_{sr} = F_{rs} = 1, \tag{A-23}$$

$$B_{sr} = B_{rs} = \begin{cases} 0.2 & s = \text{atom or molecule}, r = e^- \\ 0.15 & s = \text{atom or molecule}, r = \text{ion} \\ 0.78 & s, r = \text{atom or molecule} \\ 1.0 & \text{otherwise} \end{cases} \cdot \tag{A-24}$$

Thus, Eq. (A-21) can be viewed as giving a mixture thermal conductivity according to a mixture function, $\mathcal{N}_{AS}$, due to Armaly and Sutton, that depends on pure species thermal conductivities. In particular, if the translational temperatures for all species, except the free electron, are the same, then

$$\kappa_t = \mathcal{N}_{AS}(\ldots \kappa_{t,s \neq e^-}, \ldots). \tag{A-25}$$

In a similar manner, other mixture thermal conductivities can be defined, provided the constituents have the same temperature for the corresponding energy mode. Specifically, if the rotational temperatures are the same (there is none for the electron),

$$\kappa_r = \mathcal{N}_{AS}(\ldots \kappa_{r,s \neq e^-} \ldots). \tag{A-26}$$

If the vibrational temperatures of the molecules are the same,

$$\kappa_v = \mathcal{N}_{AS}(\ldots \kappa_{v,s=\text{molecule}} \ldots). \tag{A-27}$$

83

If the electronic temperatures are the same,

$$\kappa_e = \mathcal{N}_{AS}(\ldots, \kappa_{e,s \neq e^-}, \ldots).$$ (A-28)

Since the free electron has only a translational temperature, i.e., $T_{e^-} = T_{t,e^-}$, its thermal conductivity is given by Eq. (A-15),

$$\kappa_{e^-} = \kappa_{t,e^-} = \frac{1.5}{4} \frac{\mathcal{R}}{\mathcal{M}_{e^-}} \exp\left[\sum_{i=1}^{5} b_{i,e^-} (\ln T_{e^-})^{5-i}\right].$$ (A-29)

Finally, if all temperatures are the same and equal to T, the species thermal conductivities are determined by

$$\kappa_s = \frac{1.5}{4} \frac{\mathcal{R}}{\mathcal{M}_s} \exp\left[\sum_{i=1}^{5} b_{i,s} (\ln T)^{5-i}\right] + \rho_s \ D_s \left[C_p^{'s} - \frac{5}{2} \frac{\mathcal{R}}{\mathcal{M}_s}\right].$$ (A-30)

Here, the first expression shows the translational part. The second expression shows the translational part of the specific heat subtracted away so that the expression gives the nontranslational part of the thermal conductivity. Then, the mixture thermal conductivity is given, according to the method of Armaly and Sutton, as:

$$\kappa = \mathcal{N}_{AS}(\kappa_1, \ldots, \kappa_{ns}).$$ (A-31)

A similar procedure, due to Armaly and Sutton (Ref. 28), is used to determine the mixture viscosity, μ. First, the pure species viscosity, μ_s, for a species, s, is defined by

$$\mu_s = \frac{4}{15} \frac{\mathcal{M}_s}{\mathcal{R}} \kappa_{t,s}$$ (A-32)

where $\kappa_{t,s}$ is defined in Eq. (A-15). Thus, by Eq. (A-17), μ_s is approximated by the interpolation,

$$\mu_s = \frac{1}{10} \exp\left[\sum_{i=1}^{5} b_{i,s} (\ln T_{t,s})^{5-i}\right].$$ (A-33)

Then, the viscosity for the mixture is given by

$$\mu = -\frac{1}{\det\{H_{sr}\}} \det \begin{bmatrix} H_{11} & \cdots & H_{1,ns} & \chi_1 \\ \vdots & & \vdots & \vdots \\ H_{ns,1} & \cdots & H_{ns,ns} & \chi_{ns} \\ \chi_1 & \cdots & \chi_{ns} & 0 \end{bmatrix}.$$

Here the terms H_{sr} depend on the pure species viscosities, but the explicit form is given below only for the diagonal terms to fully specify the approximation,

$$\mu = \sum_{s=1}^{ns} \frac{\lambda_s^2}{H_{ss}}.$$

(A-34)

The diagonal terms are given by

$$H_{ss} = \frac{\lambda_s^2}{\mu_s} + \sum_{r \neq s} \frac{\lambda_s \lambda_r}{2\sqrt{2}} \frac{\sqrt{\mathcal{M}_s \mathcal{M}_r}}{(\mathcal{M}_s + \mathcal{M}_r)^{\frac{3}{2}}} \left[\frac{5}{3A_{sr}} + \frac{\mathcal{M}_r}{\mathcal{M}_s} \right] \left[\frac{\mathcal{M}_s^{\frac{1}{4}}}{\mu_s^{\frac{1}{2}}} F_{sr} + \frac{\mathcal{M}_r^{\frac{1}{4}}}{\mu_r^{\frac{1}{2}}} B_{sr} \right]^2$$

where A_{sr}, F_{sr}, and B_{sr} are given by Eqs. (A-22) – (A-24).

In the remainder of this report, it is assumed that the translational and rotational energies, $e_{t,s}$ and $e_{r,s}$, $s \neq e^-$, are distributed with the same temperature, T, i.e.,

$$T_{t,s} = T_{r,s} = T, \qquad s \neq e^-.$$

Also, the electronic excitation energies, $e_{e,s}$, $s \neq e^-$, are assumed to be distributed with the same temperature, T_e, i.e.,

$$T_{e,s} = T_e. \qquad s \neq e^-.$$

Recalling $T_{e^-} = T_{t,e^-}$, and using Eq. (A-3),

$$h_{e^-} = e_{e^-} + \frac{\mathcal{R}T_{e^-}}{\mathcal{M}_{e^-}}.$$

Since there is a single translational temperature, Eq. (A-3) shows that the translational enthalpy and energy for other species are related according to:

$$h_{t,s} = e_{t,s} + \frac{\mathcal{R}T}{\mathcal{M}_s}.$$

(A-35)

With the above definitions, the conservation equations can now be given. First, the conservation of mass for each species is expressed as:

$$\frac{\partial}{\partial t} \rho_s + \sum_{j=1}^{3} \frac{\partial}{\partial x_j} \left[\rho_s u_j + \rho_s u_{js}^d \right] = \omega_s \qquad s = 1, \ldots . ns$$

(A-36)

where $u_{j,s}^d$ is the diffusion velocity of a species, s. Also, ω_s is a source term that depends on the partial densities and the translational temperature in such a way that it vanishes when equilibrium conditions are achieved. Specifically, the source terms are constructed as follows. The reactions on which they are based can be written in the form

$$\sum_{n=1}^{ns} \nu_{r,n} M_n \rightleftharpoons \sum_{m=1}^{ns} \nu_{r,m}' M_m, \qquad 1 \leq r \leq nr. \qquad (A-37)$$

Here, $\{\nu_{r,n}\}_{n=1}^{ns}$ and $\{\nu_{r,m}'\}_{m=1}^{ns}$ are stoichiometric coefficients for the rth reaction, M_s represents one mole of species s, and nr is the number of reactions. The rate of disappearance of a species s due to the rth reaction is

$$\mathcal{L}_{r,s} = \nu_{r,s}' k_r^r \prod_{n=1}^{ns} \gamma_n^{\nu_{r,n}'} + \nu_{r,s} k_r^f \prod_{n=1}^{ns} \gamma_n^{\nu_{r,n}}. \qquad (A-38)$$

while the production rate of a species s due to the rth reaction is

$$\mathcal{G}_{r,s} = \nu_{r,s}' k_r^f \prod_{m=1}^{ns} \gamma_m^{\nu_{r,m}} + \nu_{r,s} k_r^r \prod_{m=1}^{ns} \gamma_m^{\nu_{r,m}'}. \qquad (A-39)$$

The net rate of change of species s due to all reactions is

$$\omega_s = \mathcal{M}_s \sum_{r=1}^{nr} (\mathcal{G}_{r,s} - \mathcal{L}_{r,s}). \qquad (A-40)$$

Like most aerothermochemical models, NEQPAK assumes the modified Arrhenius form (Ref. 32) for chemical reaction rates

$$k_r^f = A_r T^{B_r} exp(-C_r/T), \qquad (A-41)$$

where T is the translational temperature of the gas. The rates defined in Eq. (A-41) were obtained from fits to experimental data that were collected under conditions of thermal equilibrium. However, when the reaction rate under question represents, for instance, a two-body dissociation reaction, then the reaction rate also depends on the vibrational temperature of the gas. One of the more popular approaches used to account for thermal nonequilibrium is that of Park (Ref. 33), who replaced the translational temperature in Eq. (A-41) with a generic temperature or average temperature, T_q. Park defined T_q by the relation

$$T_q = T_V^{\alpha} T^{1-\alpha}; 0 < \alpha < 1, \qquad (A-42)$$

where α was chosen to reproduce experimental data.

The reverse reaction rate coefficient k_r^r is related to the forward rate by

$$k_r^r = k_r^f / K_r^{-c}.$$

(A-43)

where

$$K_r^{-c} = (p_{atm}/\mathcal{R}T)^{\delta_r} exp(-\frac{\Delta F_r}{\mathcal{R}T}),$$

(A-44)

is the equilibrium constant for the rth reaction and

$$\delta_r \equiv \sum_{s=1}^{n_s} (\nu'_{r,s} - \nu_{r,s});$$

$$\Delta F_r \equiv \sum_{s=1}^{n_s} (\nu'_{r,s} - \nu_{r,s}) G_s^0.$$

(A-45)

In Eq. (A-44), $p_{atm} = 1.01325 \times 10^5\ Pa$. Also G_S^0 is the Gibbs free energy for species s at the given temperature and a pressure of 1 *atm*. The Gibbs free energies are computed from curve fits taken from Ref. 27. This interpolation takes the form,

$$G_s^0(T) = \mathcal{R}T \left[a_{1,s}(1 - \ln T) - \sum_{i=1}^{4} \frac{a_{i+1,s}}{i(i+1)} T^i + \frac{a_{6,s}}{T} - a_{7,s} \right].$$

Next, the conservation of mixture momentum is expressed as:

$$\frac{\partial}{\partial t} (\rho u_i) + \sum_{j=1}^{3} \frac{\partial}{\partial x_j} \left[\rho u_i u_j + \delta_{ij} \left(p + \frac{2}{3} \mu \sum_{k=1}^{3} \frac{\partial u_k}{\partial x_k} \right) - \mu \left(\frac{\partial u_i}{\partial x_j} + \frac{\partial u_j}{\partial x_i} \right) \right]$$

$$= \left(1 - \frac{1}{n_{e^-}} \sum_{s=ion} n_s \right) \frac{\partial p_{e^-}}{\partial x_i} \qquad i = 1, 2, 3$$

(A-46)

Here, the mixture viscosity, μ, is given in Eq. (A-34).

The vibrational energy associated with each molecule is conserved according to:

$$\frac{\partial}{\partial t} (\rho_s \epsilon_{v,s}) + \sum_{j=1}^{3} \frac{\partial}{\partial x_j} \left[\rho_s \epsilon_{v,s} u_j - \kappa_{v,s} \frac{\partial T_{v,s}}{\partial x_j} + h_{v,s} \rho_s u_{js}^d \right] = \omega_{v,s}$$

s = molecule. (A-47)

87

where

$$\omega_{v,s} = \rho_s \frac{e_{v,s}^* - e_{v,s}}{\tau_{t-v,s}} + \rho_s \frac{e_{v,s}^{**} - e_{v,s}}{\tau_{e-v,s}} + \omega_s \hat{D}_s$$

Here, $e_{v,s}^*$ and $e_{v,s}^{**}$ are the vibrational energies of species s evaluated at the translational temperature, T, and the electronic excitation temperature, T_e, respectively. Also, $\tau_{t-v,s}$ and $\tau_{e-v,s}$ are the translational-vibrational energy relaxation time and electronic-vibrational energy relaxation time, respectively, for molecular species s. Finally, $\hat{D}_e$ is the average vibrational energy per unit mass of molecule s, which is created at rate ω_r.

Since all the electronic excitation energies, $e_{e,s}$, are assumed to be distributed with the same temperature, T_e, the conservation of the mixture electronic excitation energy, e_e, can be expressed in terms of this single temperature as follows:

$$\frac{\partial}{\partial t}(\rho e_e) + \sum_{j=1}^{3} \frac{\partial}{\partial x_j} \left[\rho e_e u_j - \kappa_e \frac{\partial T_e}{\partial x_j} + \sum_{s \neq e^-} h_{e,s} \rho_s u_{js}' \right] = -Q_{rad} \qquad \text{(A-48)}$$

where κ_e is given in Eq. (A-28). Also, Q_{rad} is the radiative energy transfer rate. Since the translational temperature, $T_{t,e^-} = T_{e^-}$, for the free electron is assumed to be different from that for other species, the conservation of electron energy must be written separately as:

$$\frac{\partial}{\partial t}(\rho_{e^-} e_{e^-}) + \sum_{j=1}^{3} \frac{\partial}{\partial x_j} \left[\rho_{e^-} e_{e^-} u_j - \kappa_{e^-} \frac{\partial T_{e^-}}{\partial x_j} + h_{e^-} \rho_{e^-} u_{je^-}' \right]$$

$$= -\sum_{j=1}^{3} p_{e^-} \frac{\partial u_j}{\partial x_j} + \omega_{e^-}$$

where

$$\omega_{e^-} = 3\rho_{e^-} \mathcal{R} (T - T_{e^-}) \sum_{s \neq e^-} \frac{\nu_{e^-,s}}{\mathcal{M}_s} - \sum_{s = \text{ion}} \dot{n}_{e^-,s} I_s - \sum_{s = \text{mol.}} \rho_s \frac{e_{v,s}^{**} - e_{v,s}}{\tau_{e-v,s}} \qquad \text{(A-49)}$$

and κ_{e^-} is given in Eq. (A-29). Also, $\nu_{e^-,s}$ is the effective collision frequency for electrons and heavy particles in electronic-translational energy relaxation. Then, $\dot{n}_{e^-,s}$ is the molar rate of production of species s per unit volume by electron impact ionization, and I_s is the first ionization energy of species s per kg-mole.

Finally, define the total energy as the sum of internal and kinetic energy:

$$e_T = e + 0.5 \sum_{i=1}^{3} u_i^2.$$

This is conserved according to the following:

$$\frac{\partial}{\partial t}(\rho \epsilon_T) + \sum_{j=1}^{3} \frac{\partial}{\partial x_j} \left[(\rho \epsilon_T + p)u_j - (\kappa_t + \kappa_r)\frac{\partial T}{\partial x_j} - \sum_{s=\text{mol.}} \kappa_{v,s}\frac{\partial T_{v,s}}{\partial x_j} - \kappa_\epsilon \frac{\partial T_\epsilon}{\partial x_j} - \kappa_{\epsilon-}\frac{\partial T_{\epsilon-}}{\partial x_j} \right.$$

$$\left. + \sum_{s=1}^{ns} h_s \rho_s u_{j,s}^d - \mu u_i \left(\frac{\partial u_i}{\partial x_j} + \frac{\partial u_j}{\partial x_i} \right) + \frac{2}{3}\mu u_i \delta_{ij} \sum_{k=1}^{3} \frac{\partial u_k}{\partial x_k} \right]$$

$$= \left(1 - \frac{1}{n_{e-}} \sum_{s=\text{ion}} n_s \right) \sum_{j=1}^{3} u_j \frac{\partial p_{\epsilon-}}{\partial x_j} - Q_{\text{rad}} \tag{A-50}$$

where κ_t and κ_r are given in Eqs. (A-25) and (A-26).

Now, assume that the electron energy, $e_{\epsilon-}$, and the mixture electronic excitation energy, e_ϵ, are distributed with the same temperature, T_E, i.e.,

$$T_E = T_{\epsilon-} = T_\epsilon.$$

Therefore, the conservation of the two energies can be expressed in a single equation in terms of a single temperature. For this, define the electron and electronic excitation energy,

$$\epsilon_E = \epsilon_\epsilon + \frac{\rho_{\epsilon-}}{\rho}\epsilon_{\epsilon-}.$$

Also, certain molecules may be assumed to have the same vibrational temperature. These will be called type I molecules, and their vibrational temperatures are assumed to be equal to the translational temperature, i.e.,

$$T = T_{v,s}, \qquad s = \text{type I molecule}.$$

The remaining molecules with distinct vibrational temperatures will be called type II molecules. Finally, the degree of charge separation,

$$1 - \frac{1}{n_{e-}} \sum_{s=\text{ion}} n_s$$

is assumed negligible and is set to zero in the appropriate conservation equations.

Now the conservation equations are given as follows. First, the conservation of mass for each species is expressed as

$$\frac{\partial}{\partial t}\rho_s + \sum_{j=1}^{3} \frac{\partial}{\partial x_j} \left[\rho_s u_j - \rho D_s \frac{\partial \backslash_s}{\partial x_j} \right] = \omega_s \qquad s = 1, \ldots, ns. \tag{A-51}$$

Note that in this equation and in ones that follow, the diffusion velocity of species s is approximated as

$$u_{js}^d \approx -\frac{\rho}{\rho_s} D_s \frac{\partial \chi_s}{\partial x_j} \tag{A-52}$$

where χ_s is the mole fraction of species, s, and D_s is an effective diffusion coefficient given by

$$D_s = \frac{\mathcal{M}_s \left(1 - \frac{\rho_s}{\rho}\right)}{\sum_{r \neq s} \frac{\chi_r}{\mathcal{D}_{rs}}}. \tag{A-53}$$

In general, the diffusion velocity for a given species depends on concentration gradients of other species as:

$$\sum_{r=1}^{ns} \frac{\chi_s \chi_r}{\mathcal{D}_{sr}} \left(\vec{u}_r^d - \vec{u}_s^d\right) = \nabla \chi_s + \left(\chi_s - \frac{\rho_s}{\rho}\right) \nabla \ln p - \left[\sum_{r=1}^{ns} \frac{\chi_s \chi_r}{\mathcal{D}_{rs}} \left(\frac{D_r^T}{\rho_r} - \frac{D_s^T}{\rho_s}\right)\right] \nabla \ln T$$

where D_S^T is the thermal diffusion coefficient for species s. This dependence does not appear in the approximation of Eq. (A-52).

Next, since the number density of the free electron is assumed approximately equal to the total number density of ions, the conservation of mixture momentum is expressed as:

$$\frac{\partial}{\partial t}(\rho u_i) + \sum_{j=1}^{3} \frac{\partial}{\partial x_j} \left[\rho u_i u_j + \delta_{ij} \left(p + \frac{2}{3}\mu \sum_{k=1}^{3} \frac{\partial u_k}{\partial x_k}\right) - \mu \left(\frac{\partial u_i}{\partial x_j} + \frac{\partial u_j}{\partial x_i}\right)\right] = 0$$

$$i = 1, 2, 3 \tag{A-54}$$

The vibrational energy associated with each type II molecule is conserved according to:

$$\frac{\partial}{\partial t}(\rho_s e_{v,s}) + \sum_{j=1}^{3} \frac{\partial}{\partial x_j} \left[\rho_s e_{v,s} u_j - \kappa_{v,s} \frac{\partial T_{v,s}}{\partial x_j} - \rho h_{v,s} D_s \frac{\partial \chi_s}{\partial x_j}\right] = \omega_{v,s} \tag{A-55}$$

where
$$s = \text{type II molecule.}$$

$$\omega_{v,s} = \rho_s \frac{e_{v,s}^* - e_{v,s}}{\tau_{t-v,s}} + \rho_s \frac{e_{v,s}^{**} - e_{v,s}}{\tau_{e-v,s}} + \omega_s \hat{D}_s$$

Since the mixture electronic excitation energy, e_e, and the electron energy, e_{e^-}, are assumed to be distributed with the same temperature, T_E, the conservation of the electron and electronic excitation energy, e_E, can be expressed in terms of this single temperature as follows:

90

$$\frac{\partial}{\partial t}(\rho \epsilon_E) + \sum_{j=1}^{3} \frac{\partial}{\partial x_j}\left[\rho \epsilon_E u_j - (\kappa_e + \kappa_{e-})\frac{\partial T_E}{\partial x_j} - \rho \sum_{s=1}^{n_s} h_{E,s} D_s \frac{\partial \chi_s}{\partial x_j}\right]$$

where

$$= -\sum_{j=1}^{3} p_{e-}\frac{\partial u_j}{\partial x_j} + \omega_E - Q_{rad} \qquad (A\text{-}56)$$

$$h_{E,s} = \begin{cases} h_{e-} & s = e^- \\ h_{e,s} & \text{otherwise} \end{cases}$$

and

$$\omega_E = 3\rho_r - \mathcal{R}(T - T_E)\sum_{s \neq e^-}\frac{\nu_{e-,s}}{\mathcal{M}_s} - \sum_{s=\text{ion}} \dot{n}_{e-,s}\hat{I}_s - \sum_{s=\text{mol.}}\rho_s\frac{\epsilon_{v,s}^{**} - \epsilon_{v,s}}{\tau_{e-v,s}}$$

Finally, the total energy is conserved according to the following:

$$\frac{\partial}{\partial t}(\rho \epsilon_T) + \sum_{j=1}^{3} \frac{\partial}{\partial x_j}\left[(\rho \epsilon_T + p)u_j - \left(\kappa_t + \kappa_r + \sum_{s=\text{mol. I}}\kappa_{v,s}\right)\frac{\partial T}{\partial x_j} - \sum_{s=\text{mol. II}}\kappa_{v,s}\frac{\partial T_{v,s}}{\partial x_j}\right.$$

$$\left. -(\kappa_r + \kappa_{e-})\frac{\partial T_E}{\partial x_j} - \rho\sum_{s=1}^{n_s}h_s D_s \frac{\partial \chi_s}{\partial x_j} - \mu u_i\left(\frac{\partial u_i}{\partial x_j} + \frac{\partial u_j}{\partial x_i}\right) + \frac{2}{3}\mu u_i \delta_{ij}\sum_{k=1}^{3}\frac{\partial u_k}{\partial x_k}\right] = -Q_{rad}$$

$$(A\text{-}57)$$

Now, assume that the vibrational energies of all molecules, $e_{v,s}$, s = molecule, are distributed with the same temperature, T_v, i.e.,

$$T_{v,s} = T_v, \qquad s = \text{molecule}.$$

Therefore, the conservation of vibrational energies can be expressed in a single equation involving the mixture vibrational energy, e_v, and the single temperature, T_v.

Now the conservation equations are given as follows. First, the conservation of mass and of mixture momentum are shown in Eqs. (A-54) and (A-36). The mixture vibrational energy is conserved according to:

$$\frac{\partial}{\partial t}(\rho e_v) + \sum_{j=1}^{3}\frac{\partial}{\partial x_j}\left[\rho e_v u_j - \kappa_v\frac{\partial T_v}{\partial x_j} - \rho\sum_{s=\text{mol.}}h_{v,s}D_s\frac{\partial \chi_s}{\partial x_j}\right] = \omega_v \qquad (A\text{-}58)$$

where κ_v is given in Eq. (A-27), and

$$\omega_v = \sum_{s=\text{mol.}}\omega_{v,s}.$$

The conservation of the electron and electronic excitation energy is expressed as:

$$\frac{\partial}{\partial t}(\rho \epsilon_E) + \sum_{j=1}^{3} \frac{\partial}{\partial x_j}\left[\rho \epsilon_E u_j - (\kappa_e + \kappa_{e-})\frac{\partial T_E}{\partial x_j} - \rho \sum_{s=1}^{ns} h_{E,s} D_s \frac{\partial \backslash_s}{\partial x_j}\right] \tag{A-59}$$

$$= -\sum_{j=1}^{3} p_{e-}\frac{\partial u_j}{\partial x_j} + \omega_E - Q_{rad}$$

where

$$\omega_E = 3\rho_e \cdot \mathcal{R}(T - T_E)\sum_{s\neq e^-}\frac{\nu_{e-,s}}{\mathcal{M}_s} - \sum_{s=ion}\dot{n}_{e-,s}\bar{I}_s - \sum_{s=mol.}\rho_s \frac{\epsilon_{v,s}^{**} - \epsilon_{v,s}}{\tau_{e-v,s}}$$

Finally, the total energy is conserved according to the following:

$$\frac{\partial}{\partial t}(\rho \epsilon_T) + \sum_{j=1}^{3} \frac{\partial}{\partial x_j}\left[(\rho \epsilon_T + p)u_j - (\kappa_t + \kappa_r)\frac{\partial T}{\partial x_j} - \kappa_v\frac{\partial T_v}{\partial x_j} - (\kappa_e + \kappa_{e-})\frac{\partial T_E}{\partial x_j} - \rho \sum_{s=1}^{ns} h_s D_s \frac{\partial \backslash_s}{\partial x_j}\right.$$

$$\left. -\mu u_i\left(\frac{\partial u_i}{\partial x_j} + \frac{\partial u_j}{\partial x_i}\right) + \frac{2}{3}\mu u_i \delta_{ij}\sum_{k=1}^{3}\frac{\partial u_k}{\partial x_k}\right] = -Q_{rad} \tag{A-60}$$

Now, assume that the electron and electronic excitation energy, e_E, and the mixture vibrational energy, e_v, are distributed with the same temperature, T_V, i.e.,

$$T_E = T_v = T_V.$$

Therefore, the conservation of the two energies can be expressed in a single equation involving the mixture vibrational and electronic energy,

$$e_V = e_E + e_v.$$

and the single temperature, T_V.

Now the conservation equations are given as follows. First, the conservation of mass and of mixture momentum are shown in Eqs. (A-54) and (A-36). The mixture vibrational and electronic energy is conserved according to:

$$\frac{\partial}{\partial t}(\rho \epsilon_V) + \sum_{j=1}^{3} \frac{\partial}{\partial x_j}\left[\rho \epsilon_V u_j - (\kappa_v + \kappa_e + \kappa_{e-})\frac{\partial T_V}{\partial x_j} - \rho \sum_{s=1}^{ns} h_{V,s} D_s \frac{\partial \backslash_s}{\partial x_j}\right]$$

$$= -\sum_{j=1}^{3} p_{e-}\frac{\partial u_j}{\partial x_j} + \omega_V - Q_{rad}$$

$$\tag{A-61}$$

92

where

$$h_{V,s} = \begin{cases} h_{e^-} & s = e^- \\ h_{e,s} + h_{v,s} & s = \text{molecule} \\ h_{e,s} & \text{otherwise} \end{cases}$$

and

$$\omega_V = \omega_v + \omega_E$$

Finally, the total energy is conserved according to the following:

$$\frac{\partial}{\partial t}(\rho e_T) + \sum_{j=1}^{3} \frac{\partial}{\partial x_j} \left[(\rho e_T + p)u_j - (\kappa_t + \kappa_r)\frac{\partial T}{\partial x_j} - (\kappa_v + \kappa_e + \kappa_e -)\frac{\partial T_V}{\partial x_j} - \rho \sum_{s=1}^{ns} h_s D_s \frac{\partial \lambda_s}{\partial x_j} \right.$$

$$\left. - \mu u_i \left(\frac{\partial u_i}{\partial x_j} + \frac{\partial u_j}{\partial x_i} \right) + \frac{2}{3}\mu u_i \delta_{ij} \sum_{k=1}^{3} \frac{\partial u_k}{\partial x_k} \right] = -Q_{\text{rad}} \tag{A-62}$$

Now, assume that all energies are distributed with the same temperature. The conservation equations are given as follows. First, the conservation of mass for each species is expressed in Eq. (A-36). The conservation of mixture momentum is expressed in Eq. (A-54). Finally, the total energy is conserved according to the following:

$$\frac{\partial}{\partial t}(\rho e_T) + \sum_{j=1}^{3} \frac{\partial}{\partial x_j} \left[(\rho e_T + p)u_j - \kappa\frac{\partial T}{\partial x_j} - \rho \sum_{s=1}^{ns} h_s D_s \frac{\partial \lambda_s}{\partial x_j} \right.$$

$$\left. - \mu u_i \left(\frac{\partial u_i}{\partial x_j} + \frac{\partial u_j}{\partial x_i} \right) + \frac{2}{3}\mu u_i \delta_{ij} \sum_{k=1}^{3} \frac{\partial u_k}{\partial x_k} \right] = -Q_{\text{rad}}. \tag{A-63}$$

Here, κ is given in Eq. (A-31).

APPENDIX B
CELL GEOMETRY

The method by which the flow field is discretized into a three-dimensional computational domain is described in this appendix. The numerical algorithm employed by NEDANA is a finite-volume scheme. Traditional finite-volume schemes are constructed on computational grids where the dependent variables (Q) are stored at cell centers, and the independent variables (x, y, z) are known at cell corners. Employing the notation of Gnoffo (Ref. 21), (J, K, L) denote the indices of the cell centers, and (j, k, l) denote the indices of the cell faces. The two indexing systems are related by (J, K, L) = (j + 1/2, k + 1/2, l + 1/2). In traditional schemes, the cell corners, (j, k, l), form the vertices of a computational cell, and the dependent variables represent the average of the variables over the cell volume (J, K, L). One disadvantage of this grid technique is that the grid must be shifted to output the (x, y, z) location of the dependent variables. Because NEDANA interacts with software that requires the dependent and independent variables to be written at the same location, an alternative grid system was adopted. In this system, the computation grid is constructed from the cell-centered coordinate system. In effect, the coordinate system is shifted by half an index. The areas and volumes are calculated on the (J - 1/2, K - 1/2, L - 1/2) coordinate system and stored before the flow solver is executed. This shift is made possible because the location of the cell corners is never explicitly used in the finite-volume scheme. As long as the cell volumes and areas are calculated correctly with respect to the cell centers, the coordinate system chosen is irrelevant. This shifting is transparent to the user of NEDANA because all of the cell geometry logic is performed by a preprocessor code.

The shifting does, however, affect the treatment of the boundary conditions. Unlike traditional finite-volume schemes where domain boundaries correspond to cell faces, the NEDANA boundaries correspond to cell centers. Therefore, the boundary conditions can be set directly. Figure B-1 is a schematic of the NEDANA grid system for a single plane. Note that at the boundaries, the cell face areas become cell-centered areas. This psuedo-area is appropriate because no flux evaluations are performed at the boundaries. The areas are only used for calculating normals to the surface and setting boundary conditions. In Fig. B-2, the geometry of a single computational cell is shown. In this figure, the two coordinate systems and the relative positions of the cell faces and the cell center can be more easily seen. Note that the cell faces lag the cell centers by half an index.
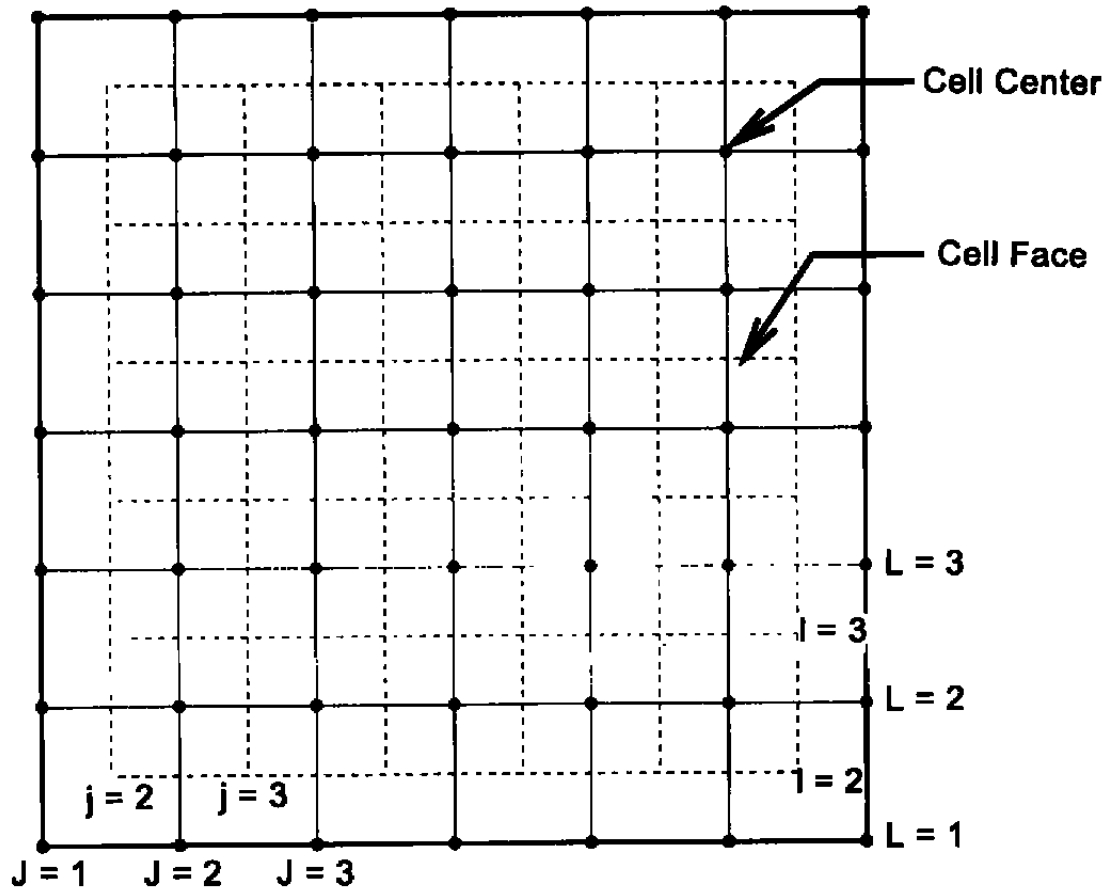
Figure B-1. NEDANA grid system.
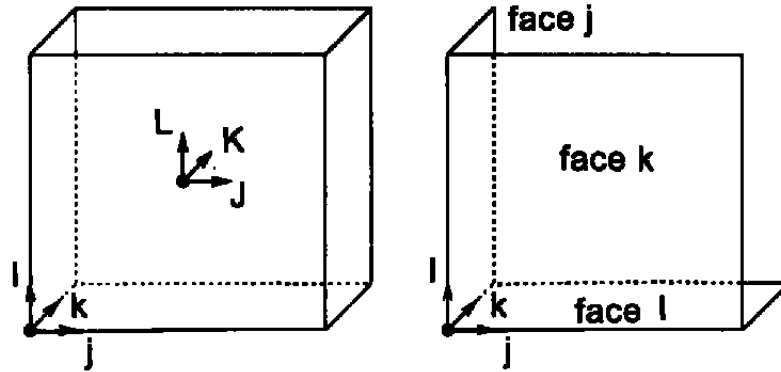
Figure B-2. Cell geometry and coordinate systems.

The calculation of the cell face areas and volumes is performed entirely by the NEDANA preprocessor code. The methodology employed follows directly from that of Gnoffo (Ref. 21). First, define the location of the cell corners with position vectors in the Cartesian coordinate system. Let

$$d\vec{r}_1 = \vec{r}_{j,k+1,l} - \vec{r}_{j,k,l+1}$$

$$d\vec{r}_2 = \vec{r}_{j,k+1,l+1} - \vec{r}_{j,k,l}$$

$$d\vec{r}_3 = \vec{r}_{j,k,l+1} - \vec{r}_{j+1,k,l}$$

$$d\vec{r}_4 = \vec{r}_{j+1,k,l+1} - \vec{r}_{j,k,l}$$

$$d\vec{r}_5 = \vec{r}_{j+1,k,l} - \vec{r}_{j,k+1,l}$$

$$d\vec{r}_6 = \vec{r}_{j+1,k+1,l} - \vec{r}_{j,k,l}$$

$$d\vec{r}_7 = \vec{r}_{j+1,k+1,l+1} - \vec{r}_{j,k,l} \tag{B-1}$$

where

$$\vec{r}_{j,k,l} = [x\hat{i}_x + y\hat{i}_y + z\hat{i}_z]_{j,k,l} . \tag{B-2}$$

The directed cell areas, σ, and the cell volume, V, can now be defined by

$$\vec{\sigma}_{\xi\,j,K,L} = \frac{d\vec{r}_1 \times d\vec{r}_2}{2}$$

$$\vec{\sigma}_{\eta\,J,k,L} = \frac{d\vec{r}_3 \times d\vec{r}_4}{2}$$

$$\vec{\sigma}_{\zeta\,J,K,l} = \frac{d\vec{r}_5 \times d\vec{r}_6}{2} \tag{B-3}$$

$$V_{J,K,L} = d\vec{r}_7 \cdot \left(\frac{\vec{\sigma}_{\xi\,j,K,L} + \vec{\sigma}_{\eta\,J,k,L} + \vec{\sigma}_{\zeta\,J,K,l}}{3} \right). \tag{B-4}$$

The projected area, $\vec{\sigma}$, with magnitude σ, is normal to the cell face and points in the direction of increasing J, K, L, respectively. In the NEDANA notation, the cell face areas are written

$$
\begin{aligned}
\vec{\sigma}_{\xi\,J,K,L} &= \sigma_\xi^x \hat{i}_x + \sigma_\xi^y \hat{i}_y + \sigma_\xi^z \hat{i}_z \\
\vec{\sigma}_{\eta\,J,K,L} &= \sigma_\eta^x \hat{i}_x + \sigma_\eta^y \hat{i}_y + \sigma_\eta^z \hat{i}_z \\
\vec{\sigma}_{\zeta\,J,K,L} &= \sigma_\zeta^x \hat{i}_x + \sigma_\zeta^y \hat{i}_y + \sigma_\zeta^z \hat{i}_z
\end{aligned}
\tag{B-5}
$$

where the terms σ^x, σ^y, and σ^z denote the magnitude of the area as projected onto the Cartesian coordinates. The transformation metrics in a finite-volume scheme, such as ξ_x, ξ_y, ξ_z, are expressed as the ratio of cell face areas to cell volumes. Equation (B-4) is first-order accurate with respect to a cell face or a cell volume. Gnoffo states that this formulation introduces errors when crossing an axis singularity. Gnoffo proposes a second-order accurate expression that uses symmetric averages of differences about the cell center. The volume can now be expressed as

$$
V_{J,K,L} = \frac{d\vec{r}_8 \cdot (\vec{\sigma}_{\xi\,J,K,L} + \vec{\sigma}_{\xi\,J+1,K,L} + \vec{\sigma}_{\eta\,J,k,L} + \vec{\sigma}_{\eta\,J,k+1,L} + \vec{\sigma}_{\zeta\,J,K,l} + \vec{\sigma}_{\zeta\,J,K,l+1})}{6}
\tag{B-6}
$$

where

$$
d\vec{r}_8 = [(\hat{x}_\xi + \hat{x}_\eta + \hat{x}_\zeta)\hat{i}_x + (\hat{y}_\xi + \hat{y}_\eta + \hat{y}_\zeta)\hat{i}_y + (\hat{z}_\xi + \hat{z}_\eta + \hat{z}_\zeta)\hat{i}_z]_{J,K,L}
\tag{B-7}
$$

and

$$
\begin{aligned}
[\hat{s}_\xi]_{J,K,L} &= \frac{[\hat{s}_\xi]_{J,k,L} + [\hat{s}_\xi]_{J,k+1,L}}{2} = \frac{[\hat{s}_\xi]_{J,K,l} + [\hat{s}_\xi]_{J,K,l+1}}{2} \\
[\hat{s}_\eta]_{J,K,L} &= \frac{[\hat{s}_\eta]_{j,K,L} + [\hat{s}_\eta]_{j+1,K,L}}{2} = \frac{[\hat{s}_\eta]_{J,K,l} + [\hat{s}_\eta]_{J,K,l+1}}{2} \\
[\hat{s}_\zeta]_{J,K,L} &= \frac{[\hat{s}_\zeta]_{J,k,L} + [\hat{s}_\zeta]_{J,k+1,L}}{2} = \frac{[\hat{s}_\zeta]_{j,K,l} + [\hat{s}_\zeta]_{j+1,K,L}}{2}
\end{aligned}
\tag{B-8}
$$

where the generic differences $\hat{s}$ are second-order accurate with respect to the cell centers, and the dummy variable s represents the independent variables x, y, z. The $\bar{s}$ differences are second-order accurate with respect to the cell faces and have the form

$$
\begin{aligned}
{[\bar{s}_\xi]}_{J,k,L} &= \frac{1}{2}(s_{j+1,k,l} - s_{j,k,l} + s_{j+1,k,l+1} - s_{j,k,l+1}) \\
{[\bar{s}_\xi]}_{J,K,l} &= \frac{1}{2}(s_{j+1,k,l} - s_{j,k,l} + s_{j+1,k+1,l} - s_{j,k+1,l}) \\
{[\bar{s}_\eta]}_{j,K,L} &= \frac{1}{2}(s_{j,k+1,l} - s_{j,k,l} + s_{j,k+1,l+1} - s_{j,k,l+1}) \\
{[\bar{s}_\eta]}_{J,K,l} &= \frac{1}{2}(s_{j,k+1,l} - s_{j,k,l} + s_{j+1,k+1,l} - s_{j+1,k,l}) \\
{[\bar{s}_\zeta]}_{j,K,L} &= \frac{1}{2}(s_{j,k,l+1} - s_{j,k,l} + s_{j,k+1,l+1} - s_{j,k+1,l}) \\
{[\bar{s}_\zeta]}_{J,k,L} &= \frac{1}{2}(s_{j,k,l+1} - s_{j,k,l} + s_{j+1,k,l+1} - s_{j+1,k,l}).
\end{aligned}
\tag{B-9}
$$

The transformation metrics are defined by

$$
\begin{bmatrix} \xi_x & \eta_x & \zeta_x \\ \xi_y & \eta_y & \zeta_y \\ \xi_z & \eta_z & \zeta_z \end{bmatrix} = \begin{bmatrix} x_\xi & y_\xi & z_\xi \\ x_\eta & y_\eta & z_\eta \\ x_\zeta & y_\zeta & z_\zeta \end{bmatrix}^{-1} . \tag{B-10}
$$

In finite-volume notation, these terms are written as the ratio of cell face areas to cell volumes

$$
\vec{\nabla}\xi_{j,K,L} = \frac{\vec{\sigma}_{\xi\,j,K,L}}{V_{J,K,L}}
$$

$$
\vec{\nabla}\eta_{J,k,L} = \frac{\vec{\sigma}_{\eta\,J,k,L}}{V_{J,K,L}} \tag{B-11}
$$

$$
\vec{\nabla}\zeta_{J,K,l} = \frac{\vec{\sigma}_{\zeta\,J,K,l}}{V_{J,K,L}} .
$$

Equations (B-11) are only first-order accurate. The reason being that $\vec{\sigma}$ is second-order accurate with respect to cell faces but only first-order accurate with respect to cell centers; and conversely, V is second-order accurate with respect to the cell centers but only first-order accurate with respect to cell faces. Gnoffo suggests using a symmetric average of cell faces and volumes to obtain second-order accurate metrics for the evaluation of viscous terms. These second-order accurate metrics take the form

$$
\vec{\nabla}\xi_{j,K,L} = \frac{V_{J,K,L}(\vec{\sigma}_{\xi\,j-1,K,L} + \vec{\sigma}_{\xi\,j,K,L}) + V_{J-1,K,L}(\vec{\sigma}_{\xi\,j,K,L} + \vec{\sigma}_{\xi\,j+1,K,L})}{4\,V_{J,K,L}V_{J-1,K,L}}
$$

$$
\vec{\nabla}\xi_{J,k,L} = \frac{V_{J,K,L}(\vec{\sigma}_{\xi\,j,K-1,L} + \vec{\sigma}_{\xi\,j+1,K-1,L}) + V_{J,K-1,L}(\vec{\sigma}_{\xi\,j,K,L} + \vec{\sigma}_{\xi\,j+1,K,L})}{4\,V_{J,K,L}V_{J,K-1,L}}
$$

$$
\vec{\nabla}\xi_{J,K,l} = \frac{V_{J,K,L}(\vec{\sigma}_{\xi\,j,K,L-1} + \vec{\sigma}_{\xi\,j+1,K,L-1}) + V_{J,K,L-1}(\vec{\sigma}_{\xi\,j,K,L} + \vec{\sigma}_{\xi\,j+1,K,L})}{4\,V_{J,K,L}V_{J,K,L-1}}
$$

$$
\vec{\nabla}\eta_{j,K,L} = \frac{V_{J,K,L}(\vec{\sigma}_{\eta\,J-1,k,L} + \vec{\sigma}_{\eta\,J-1,k+1,L}) + V_{J-1,K,L}(\vec{\sigma}_{\eta\,J,k,L} + \vec{\sigma}_{\eta\,J,k+1,L})}{4\,V_{J,K,L}V_{J-1,K,L}}
$$

$$
\vec{\nabla}\eta_{J,k,L} = \frac{V_{J,K,L}(\vec{\sigma}_{\eta\,J,k-1,L} + \vec{\sigma}_{\eta\,J,k,L}) + V_{J,K-1,L}(\vec{\sigma}_{\eta\,J,k,L} + \vec{\sigma}_{\eta\,J,k+1,L})}{4\,V_{J,K,L}V_{J,K-1,L}}
$$

$$
\vec{\nabla}\eta_{J,K,l} = \frac{V_{J,K,L}(\vec{\sigma}_{\eta\,J,k,L-1} + \vec{\sigma}_{\eta\,J,k+1,L-1}) + V_{J,K,L-1}(\vec{\sigma}_{\eta\,J,k,L} + \vec{\sigma}_{\eta\,J,k+1,L})}{4\,V_{J,K,L}V_{J,K,L-1}}
$$

$$
\vec{\nabla}\zeta_{j,K,L} = \frac{V_{J,K,L}(\vec{\sigma}_{\zeta\,J-1,K,l} + \vec{\sigma}_{\zeta\,J-1,K,l+1}) + V_{J-1,K,L}(\vec{\sigma}_{\zeta\,J,K,l} + \vec{\sigma}_{\zeta\,J,K,l+1})}{4\,V_{J,K,L}V_{J-1,K,L}}
$$

$$
\vec{\nabla}\zeta_{J,k,L} = \frac{V_{J,K,L}(\vec{\sigma}_{\zeta\,J-1,K,l} + \vec{\sigma}_{\zeta\,J-1,K,l+1}) + V_{J,K-1,L}(\vec{\sigma}_{\zeta\,J,K,l} + \vec{\sigma}_{\zeta\,J,K,l+1})}{4\,V_{J,K,L}V_{J,K-1,L}}
$$

$$
\vec{\nabla}\zeta_{J,K,l} = \frac{V_{J,K,L}(\vec{\sigma}_{\zeta\,J,K,l-1} + \vec{\sigma}_{\zeta\,J,K,l}) + V_{J,K,L-1}(\vec{\sigma}_{\zeta\,J,K,l} + \vec{\sigma}_{\zeta\,J,K,l+1})}{4\,V_{J,K,L}V_{J,K,L-1}} . \tag{B-12}
$$

APPENDIX C
NUMERICAL BACKGROUND

The purpose of this appendix is to discuss basic issues crucial to the selection of a finite-volume scheme for the solution of the nonequilibrium flow equations shown in Eq. (43). The topics covered include first, the properties of schemes that guarantee convergence of approximate solutions: conservativeness, consistency, and total variation stability. Then the flux-limited and the slope-limited approaches to constructing high-resolution convergent schemes are introduced. The examples given to illustrate these two approaches are Yee's symmetric TVD scheme and van Leer's MUSCL scheme, respectively. However, a primary objective of the work documented in this report is that the numerical method selected be not only fast, accurate, and stable, but also easy to understand and modify. With this in mind, Jameson's flux-limited dissipation model is developed as an alternative to the previously defined techniques. Most of this material is presented for scalar model problems but also is briefly generalized to a vector setting. For a more detailed discussion of the issues addressed in this appendix, see LeVeque (Ref. 61).

For simplicity, first consider methods for solving the model problem,

$$q_t + f_x = 0. \tag{C-1}$$

The task is to approximate the solution to this problem on a space-time grid, $\{(x_j, t^n)\}$, with grid values $\{q_j^n\}$ such that $q_j^n \approx q(x_j, t^n)$. Although all grid values are known only at grid points, the definition of certain numerical constructs will be motivated by focusing on activity at the midpoints, $x_{j+1/2} = 1/2(x_j + x_{j+1})$. These will also be referred to as the interface points between adjacent spatial cells. The jth such cell is defined as the set of points for which x is between $x_{j-1/2}$ and $x_{j+1/2}$.

It will also be necessary to consider the performance of approximation schemes on space-time grids of ever increasing refinement. Specifically, it is crucial that the grid values $\{q_j^n\}$ approximate a solution, q, with arbitrarily small error, provided $\Delta t = t^{n+1}-t^n$ and $\Delta x = x_{j+1/2} - x_{j-1/2}$ are sufficiently small. This convergence is theoretically guaranteed of finite-difference schemes that:

1. can be written in *conservation form,*

2. are *consistent,* and

3. are *total variation diminishing* (TVD).

These three conditions are explained in detail below.

C-1.0 CONSERVATION FORM AND NUMERICAL FLUX FUNCTIONS

Before deriving a finite-difference approximation to Eq. (C-1), note that a physically relevant *solution*, q, to Eq. (C-1) may develop discontinuities even in cases in which the initial data, $q(x, 0)$, are smooth (Ref. 62). Such a q would not satisfy the differential equation in a strict sense. Thus, it is productive to express Eq. (C-1) in a weaker form, where no differentiability is required of the solution. This is accomplished by integrating the differential equation over an arbitrary space-time cell, say $[x_1, x_2] \times [t_1, t_2]$. Specifically, integrating q_t explicitly with respect to t, and f_x explicitly with respect to x gives the integral equation:

$$\int_{x_1}^{x_2} [q(x, t_2) - q(x, t_1)] dx + \int_{t_1}^{t_2} [f(q(x_2, t)) - f(q(x_1, t))] dt = 0.$$

Notice that no derivatives appear in this equation. In particular, the meaning is clear even if a solution is discontinuous. A function, q, that satisfies this equation for all x_1, x_2, t_1 and t_2 is said to be a *weak solution* to Eq. (C-1). Toward a finite-difference approximation to this, let the integration cell be $[x_{j-1/2}, x_{j+1/2}] \times [t^n, t^{n+1}]$, so that it is aligned with a space-time grid cell. Then the above equation can be written in the finite-volume form:

$$[\bar{q}^{n+1} - \bar{q}^n]\Delta x + [\bar{f}_{j+\frac{1}{2}} - \bar{f}_{j-\frac{1}{2}}]\Delta t = 0.$$

Here, $\bar{q}^n$ and $\bar{q}^{n+1}$ denote averages of the solution over the spatial interval, $[x_{j-1/2}, x_{j+1/2}]$, at times $t = t^n$ and $t = t^{n+1}$, respectively. Also, $f_{j-1/2}$ and $f_{j+1/2}$ denote averages of the flux over the temporal interval, $[t^n, t^{n+1}]$, at cell interfaces $x = x_{j-1/2}$ and $x = x_{j+1/2}$, respectively. This calculation motivates the distinction of finite-difference schemes in the following *conservation form*:

$$\frac{q_j^{n+1} - q_j^n}{\Delta t} + \frac{f_{j+\frac{1}{2}}^* - f_{j-\frac{1}{2}}^*}{\Delta x} = 0. \tag{C-2}$$

Compare the last two equations. Here, the grid value, q_j^n, approximates the spatial average, $\bar{q}^n$. Also, the temporal average, $\bar{f}_{j+1/2}$ is approximated by the *numerical flux function*, $f_{j+1/2}^*$. A sample f^* is given by:

$$f_{j+\frac{1}{2}}^* = \tfrac{1}{2}(f_j^n + f_{j+1}^n) \tag{C-3}$$

which leads to the central difference approximation to f_x:

$$\frac{f_{j+\frac{1}{2}}^* - f_{j-\frac{1}{2}}^*}{\Delta x} = \frac{f_{j+1}^n - f_{j-1}^n}{2\Delta x}.$$

C-2.0 CONSISTENCY

In general, $f^*_{j+1/2}$ is a function of a certain number of grid values on opposite sides of the interface at $x_{j+1/2}$. Also, these could be taken from time level t^n or t^{n+1}. In the example shown in Eq. (C-3), $f^*_{j+1/2} = f^*_{j+1/2}(q^n_j, q^n_{j+1})$.

A natural requirement of any numerical flux function is that it should reduce to the exact flux in certain simple cases. For example, if the solution is a constant, $q = \bar{q}$, then the flux is a constant, $f = f(\bar{q})$. Therefore, f^* should satisfy:

$$f^*_{j+\frac{1}{2}}(\bar{q}, \ldots, \bar{q}) = f(\bar{q}). \tag{C-4}$$

Schemes of the form shown in Eq. (C-2) for which this condition holds (and for which f^* depends sufficiently smoothly on its arguments) are said to be *consistent*. In particular, the central difference example mentioned above is consistent since $f_{j+1/2}(q^n_j, q^n_{j+1}) = 1/2(f^n_j + f_{j+1})$ implies that $f^*_{j+1/2j}(\bar{q}, \bar{q}) = 1/2(f(\bar{q}) + f(\bar{q})) = f(\bar{q})$. Note that this particular notion of consistency is an example of a general notion that may be more familiar to the reader. Specifically, a finite-difference equation is said to be a consistent approximation to a differential (or integral) equation, if the solution to the latter satisfies the former, except for a residual that vanishes in the limit of ever increasing grid refinement.

C-3.0 TVD PROPERTY

Although the central difference example given above easily demonstrates consistency, it does not lead to a stable scheme. In fact, it can lead to errors that increase without bound as the number of time steps increases. On the other hand, there are schemes that give bounded solutions, but with spurious oscillations near discontinuities. When such oscillations develop in the grid function, $\{q^n_j\}$, its total variation,

$$TV(\{q^n_j\}) \equiv \sum_j |q^n_j - q^n_{j-1}|$$

increases with respect to n. Observe that this is an appropriate measure of the spatial variation in q^n, since $TV(\{q^n_j\})$ approximates the spatial integral of $|\partial q^n/\partial x|$. Thus, a particular notion of stability based on the total variation is now introduced. Specifically, a method is said to be *total variation diminishing* (TVD) if

$$TV(\{q^{n+1}_j\}) \leq TV(\{q^n_j\}).$$

The TVD property is geometrically straightforward; nevertheless, from a practical perspective, it is important to have criteria that can be verified easily to show that a given scheme is TVD. For this, let the terms of the scheme be rearranged in the form:

$$\frac{\Delta_t q_j^n}{\Delta t} + L_j^+ \frac{\Delta_x q_j^{n+1}}{\Delta x} + L_j^- \frac{\Delta_x q_{j-1}^{n+1}}{\Delta x} = R_j^+ \frac{\Delta_x q_j^n}{\Delta x} + R_j^- \frac{\Delta_x q_{j-1}^n}{\Delta x} \qquad \text{(C-5)}$$

where

$$\Delta_t q_j^n \equiv q_j^{n+1} - q_j^n \quad \text{and} \quad \Delta_x q_j^n \equiv q_{j+1}^n - q_j^n.$$

To make this process more concrete, consider an upwind example for which the numerical flux function is given by:

$$f_{j+\frac{1}{2}}^* = \tfrac{1}{2}(f_{j+1}^n + f_j^n) - \tfrac{1}{2}|a_{j+\frac{1}{2}}^n|(q_{j+1}^n - q_j^n), \quad \text{where} \quad a_{j+\frac{1}{2}}^n \equiv \frac{f_{j+1}^n - f_j^n}{q_{j+1}^n - q_j^n}. \qquad \text{(C-6)}$$

Observe that the consistency criterion in Eq. (C-4) is satisfied by this example. Also, a few calculations show that:

$$\delta_x f_j^* = \tfrac{1}{2}\left[a_{j+\frac{1}{2}}^n - |a_{j+\frac{1}{2}}^n| \right] \Delta_x q_j^n + \tfrac{1}{2}\left[a_{j-\frac{1}{2}}^n + |a_{j-\frac{1}{2}}^n| \right] \nabla_x q_j^n$$

where

$$\delta_x f_j^* \equiv f_{j+\frac{1}{2}}^* - f_{j-\frac{1}{2}}^* \quad \text{and} \quad \nabla_x q_j^n \equiv q_j^n - q_{j-1}^n.$$

The upwinding character in this formula is seen by noting that backward or forward differencing is used on q depending on the sign of a, i.e., the wind direction. When this expression is inserted into the conservation form in Eq. (C-2), the following result is obtained:

$$\frac{\Delta_t q_j^n}{\Delta t} = \tfrac{1}{2}\left[|a_{j+\frac{1}{2}}^n| - a_{j+\frac{1}{2}}^n \right] \frac{\Delta_x q_j^n}{\Delta x} - \tfrac{1}{2}\left[|a_{j-\frac{1}{2}}^n| + a_{j-\frac{1}{2}}^n \right] \frac{\Delta_x q_{j-1}^n}{\Delta x}.$$

Compare this with Eq. (C-5) to find that for the upwind scheme:

$$L_j^+ = 0, \quad L_j^- = 0, \quad R_j^+ = \tfrac{1}{2}\left[|a_{j+\frac{1}{2}}^n| - a_{j+\frac{1}{2}}^n \right], \quad \text{and} \quad R_j^- = -\tfrac{1}{2}\left[|a_{j-\frac{1}{2}}^n| + a_{j-\frac{1}{2}}^n \right].$$

Thus, as this example illustrates, a given scheme can always be written in the form shown in Eq. (C-5). Furthermore, provided $\Delta t/\Delta x$ is sufficiently small, the upwind scheme is seen to be TVD according to the following general result due to Harten, (Ref 63), and Jameson and Lax, (Ref. 64).

A finite-difference scheme in the form of Eq. (C-5) is TVD if $L_j^+ \leq 0$,
$L_j^- \geq 0$, $R_j^+ \geq 0$, $R_j^- \leq 0$ *and* $(R_{j-1}^+ - R_j^-)\Delta t/\Delta x \leq 1$.

Note that the conditions stated here are sufficient for a scheme to be TVD. They are not necessary. Moreover, a given scheme is not represented uniquely in the form shown in Eq. (C-5). Therefore, it may be necessary to experiment with different ways of defining the coefficients before the above conditions can be verified.

C-4.0 CONVERGENCE

The forgoing concepts are now summarized precisely in the following convergence result.

Suppose a grid function is generated by a TVD finite-difference scheme which is consistent with the scalar wave equation in Eq. (C-1). Also, assume that the scheme can be written in conservation form. Then, the grid function approximates some weak solution to Eq. (C-1) (in an integral sense) with arbitrarily small error, provided Δt and Δx are sufficiently small.

For example, the basic upwind scheme defined by Eq. (C-6) satisfies all stated conditions. Therefore, it can be used to compute an arbitrarily accurate approximation to a weak solution. However, this scheme is only first-order accurate and is extremely dissipative. In other words, it does not offer high resolution of a weak solution, without a highly refined grid. Therefore, the discussion now turns to the development of high-resolution schemes that satisfy the conditions of the convergence result given above.

C-5.0 HIGH-RESOLUTION SCHEMES

The construction of a high-resolution method begins with the observation that the order of the method should switch according to the smoothness of the solution. Specifically, greater accuracy can be achieved in regions where the solution is smooth, by using a higher-order method. On the other hand, such a method causes oscillations around discontinuities such as shocks. Thus, in these regions, it is necessary to switch to a lower-order method.

103

C-6.0 FLUX-LIMITED APPROACH

This switching can be accomplished according to a *flux-limited* approach such as the following. Let f^* be a numerical flux function such that $\delta_x f^*/\Delta x$ approximates f_x to an order corresponding to the smoothness of q. In other words, $\delta_x f^*/\Delta x$ switches from a high-order approximation to f_x where q is smooth, to a low-order approximation to f_x where q is nonsmooth. Specifically, f^* can have the form

$$f_{j\pm\frac{1}{2}}^* = f_{j\pm\frac{1}{2}}^H + [1 - \Phi_{j\pm\frac{1}{2}}](f_{j\pm\frac{1}{2}}^L - f_{j\pm\frac{1}{2}}^H), \qquad \text{(C-7)}$$

where $\delta_x f^H/\Delta x$ and $\delta_x f^L/\Delta x$ are high- and low-order approximations to f_x, respectively. Also, Φ is a nonlinear *flux limiter*. It is so-named because the use of high-order flux terms is limited as Φ switches from one to zero whenever a lack of smoothness is detected in q.

For example, f^H might correspond to central differencing as explained after Eq. (C-3). This can be implemented by setting

$$f_{j+\frac{1}{2}}^H = \tfrac{1}{2}(f_{j+1}^n + f_j^n). \qquad \text{(C-8)}$$

Also, f^L might correspond to upwinding as explained after Eq. (C-6). This can be achieved with

$$f_{j+\frac{1}{2}}^L = \tfrac{1}{2}(f_{j+1}^n + f_j^n) - \tfrac{1}{2}|a_{j+\frac{1}{2}}^n|(q_{j+1}^n - q_j^n). \qquad \text{(C-9)}$$

For the flux limiter, Φ, to perform the switching from f^H to f^L, it must be constructed to detect a lack of smoothness in the solution, q. For example, this can be accomplished by monitoring the ratio of differences,

$$r_j^n \equiv \frac{q_{j+1}^n - q_j^n}{q_j^n - q_{j-1}^n}, \quad q_j^n \neq q_{j-1}^n, \qquad r_j^n \equiv 0, \quad q_j^n = q_{j-1}^n.$$

Specifically, r_j^n is negative when the solution is oscillating. This should trigger the use of only low-order flux terms. On the other hand, when r_j^n is close to one, q is smooth and the high-order flux terms should be switched on. A typical limiter can be implemented by defining:

$$\Phi_{j+\frac{1}{2}} = \phi(r_j^n)\psi(r_{j+1}^n), \qquad \text{(C-10)}$$

where

$$\phi(r) = \mathrm{minmod}(1,r) = \begin{cases} \mathrm{min}(1,r) & r > 0 \\ 0 & r \leq 0 \end{cases} \quad \text{and} \quad \psi(r) = \phi(\tfrac{1}{r}). \qquad \text{(C-11)}$$

Note that $\Phi_{j+1/2}$ becomes zero when $r_j^n \leq 0$ or $r_{j+1}^n \leq 0$; it approaches one when r_j^n and r_{j+1}^n are close to one. This gives a continuous switching required in Eq. (C-7). Also, Φ can be shown to satisfy conditions which guarantee that the scheme is TVD (Ref. 65).

C-7.0 SLOPE-LIMITED APPROACH

Alternatively, the switching can be accomplished according to a *slope-limited* approach as follows. As before, the numerical flux function is constructed so that $\delta_x f^* / \Delta x$ approximates f_x to an order corresponding to the smoothness of q. However, in the present approach, the switching occurs among q values instead of among fluxes. This is performed within the framework of a discretization procedure which is originally due to Gudonov (Ref. 66), which is described in detail below. Basically, the procedure consists of the following. At a given time level, the variations in the solution are approximated by jumps at cell interfaces. In fact, the accuracy of this approximation determines the order of the method. Next, the waves resulting from these jumps are propagated forward in time. When this information reaches the next time level, it is averaged to complete the time step.

To implement this procedure, the solution is initially approximated by a constant on opposite sides of a cell interface. Let the value on the right of $x_{j+1/2}$ be denoted by $q_{j+1/2}^R$, and the value on the left by $q_{j+1/2}^L$. For example, they can be determined by zeroth-order extrapolation according to:

$$q_{j+\frac{1}{2}}^R = q_{j+1}^n \quad \text{and} \quad q_{j+\frac{1}{2}}^L = q_j^n. \tag{C-12}$$

Since these values are generally not equal, this piecewise constant approximation creates a jump, $q_{j+1/2}^R - q_{j+1/2}^L$, , at the cell interface, $x_{j+1/2}$. Next, this information is propagated forward in time by assigning it as the initial state for the linearized problem,

$$\partial_t w_{j+\frac{1}{2}}(x,t) + \bar{a}_{j+\frac{1}{2}}^n \partial_x w_{j+\frac{1}{2}}(x,t) = 0, \quad \text{where} \quad \bar{a}_{j+\frac{1}{2}}^n \equiv \frac{f(q_{j+\frac{1}{2}}^R) - f(q_{j+\frac{1}{2}}^L)}{q_{j+\frac{1}{2}}^R - q_{j+\frac{1}{2}}^L}.$$

This *Riemann problem* can be solved explicitly for every interface $x_{j+1/2}$. Then the solutions are superimposed so that the grid value, q_{j+1}^n, is determined according to an average of values at time level t^{n+1},

$$q_j^{n+1} = \frac{1}{\Delta x}\left[\int_{x_{j-\frac{1}{2}}}^{x_j} w_{j-\frac{1}{2}}(x,t^{n+1})dx + \int_{x_j}^{x_{j+\frac{1}{2}}} w_{j+\frac{1}{2}}(x,t^{n+1})dx\right].$$

The details are not provided, but it can be shown that this scheme has a numerical flux function with the form:

$$f^*_{j+\frac{1}{2}} = \frac{1}{2}\left(f(q^R_{j+\frac{1}{2}}) + f(q^L_{j+\frac{1}{2}})\right) - \frac{1}{2}|\breve{a}^n_{j+\frac{1}{2}}|\left(q^R_{j+\frac{1}{2}} - q^L_{j+\frac{1}{2}}\right). \qquad \text{(C-13)}$$

Note that this is identical to the low-order upwind flux in Eq. (C-9), under the condition of the zeroth-order extrapolation shown in Eq. (C-12). This gives the low-order method to be used where the solution is nonsmooth. A higher-order method is obtained by improving the accuracy of the extrapolation. However, the first-order extrapolations,

$$q^R_{j+\frac{1}{2}} = \left\{ q^n_{j+1} - \frac{x_{j+1} - x}{x_{j+2} - x_{j+1}}(q^n_{j+2} - q^n_{j+1}) \right\}\Bigg|_{x=x_{j+\frac{1}{2}}} = q^n_{j+1} - \frac{1}{2}\Delta_x q^n_{j+1}$$

$$q^L_{j+\frac{1}{2}} = \left\{ q^n_j + \frac{x - x_j}{x_j - x_{j-1}}(q^n_j - q^n_{j-1}) \right\}\Bigg|_{x=x_{j+\frac{1}{2}}} = q^n_j + \frac{1}{2}\nabla_x q^n_j$$

lead to unwanted oscillations in nonsmooth regions. Thus, to limit the slope variations appearing in these linear approximations, *slope limiters*, ϕ and ψ, are introduced to give:

$$q^R_{j+\frac{1}{2}} = q^n_{j+1} - \frac{1}{2}\phi(r^n_{j+1})\Delta_x q^n_{j+1} \quad \text{and} \quad q^L_{j+\frac{1}{2}} = q^n_j + \frac{1}{2}\psi(r^n_j)\nabla_x q^n_j. \qquad \text{(C-14)}$$

Again, ϕ and ψ are defined by Eq. (C-11), but their interpretation here is different. Before, they were used to limit the use of high-order flux terms. Here, they limit the use of large slopes in a linear approximation of the solution.

The scheme will now be summarized. When a lack of smoothness is detected in the solution, the interface values are determined by zeroth-order extrapolation. This leads to a low-order upwind numerical flux function. On the other hand, when the solution is smooth, the interface values are determined by first-order, linear extrapolation. The result is a high-order upwind numerical flux function. The switching is performed according to the formulas in Eqs. (C-13) and (C-14). Also, the slope limiters can be shown to satisfy conditions which guarantee that the scheme is TVD. This slope-limited method is an example of a MUSCL scheme (Ref. 67).

C-8 VECTOR FORM

Now consider the generalization of the above schemes for nonscalar problems such as the one-dimensional Euler equations,

$$Q_t + F_x = 0.$$

Focus on generalizing Eqs. (C-9) and (C-13), in particular, since it is not clear how to form a counterpart to $a^n_{j+1/2}$ or $\tilde{a}^N_{j+1/2}$. This is accomplished in the following first-order upwind Roe scheme:

$$\frac{\Delta_t Q^n_j}{\Delta t} + \frac{\delta_x F^*_j}{\Delta x} = 0$$

where

$$F^n_{j+\frac{1}{2}} = \tfrac{1}{2}(F^n_{j+1} + F^n_j) - \tfrac{1}{2}|A^n_{j+\frac{1}{2}}|(Q^n_{j+1} - Q^n_j).$$

For this, the absolute value of a matrix is defined in terms of the absolute values of its eigenvalues. Specifically, if $A = S^{-1}\Lambda S$, where $\Lambda = \text{diag}\{\lambda_i\}$, then

$$|A| = S^{-1}|\Lambda|S, \qquad \text{where} \qquad |\Lambda| = \text{diag}\{|\lambda_i|\}.$$

The most conspicuous property defining $A^n_{j+1/2}$ above is that

$$A^n_{j+\frac{1}{2}}(Q^n_{j+1} - Q^n_j) = F^n_{j+1} - F^n_j.$$

Such a matrix can be constructed by a special averaging procedure. This was done by Roe (Ref. 68) for the case of a perfect gas, and extended to nonequilibrium flows by Liu and Vinokur (Ref. 69).

The flux-limited approach introduced above can be implemented by setting

$$F^*_{j+\frac{1}{2}} = \frac{1}{2}(F^n_{j+1} + F^n_j) - \frac{1}{2}S^{-1}(I - \bar{\Phi}^n_{j+\frac{1}{2}})|\Lambda^n|S(Q^n_{j+1} - Q^n_j) \qquad (A = S^{-1}\Lambda S)$$

where $\Phi^n_{j+1/2}$ is a diagonal matrix whose ith entry is a flux limiter as shown in Eq. (C-10), with q^n_j replaced with the ith component of SD^n_j.

Finally, the slope-limited MUSCL approach introduced above can be implemented by setting

$$F^*_{j+\frac{1}{2}} = \frac{1}{2}\left(F(Q^R_{j+\frac{1}{2}}) + F(Q^L_{j+\frac{1}{2}})\right) - \frac{1}{2}|\tilde{A}^n_{j+\frac{1}{2}}|\left(Q^R_{j+\frac{1}{2}} - Q^L_{j+\frac{1}{2}}\right)$$

where

$$\tilde{A}^n_{j+\frac{1}{2}}(Q^R_{j+\frac{1}{2}} - Q^L_{j+\frac{1}{2}}) = F(Q^R_{j+\frac{1}{2}}) - F(Q^L_{j+\frac{1}{2}})$$

and the components of $Q_{j+1/2}^R$ and $Q_{j+1/2}^L$ are defined in terms of slope limiters as shown in Eq. (C-14).

Note the complexity of defining such upwind schemes. In addition, extending upwinding techniques to higher dimensions is not straightforward. In fact, attempts to generalize these schemes to two or three dimensions have resulted in the production of zigzag shocks unless the grid is aligned with the shock. Also, the eigenvalues and eigenvectors of A would have to be rederived and coded whenever a new thermo-chemical model was considered. Therefore, as an alternative to the matrix-based dissipation models presented above, Jameson's flux-limited scalar dissipation was selected for incorporation into NEDANA to satisfy the objectives of this developmental effort. Jameson's model is discussed below.

C-9.0 JAMESON'S FLUX-LIMITED DISSIPATION MODEL

The high resolution schemes based on upwinding presented in the previous subsection have developed in parallel with those based on artificial dissipation models. The concept of artificial dissipation originated with von Neumann and Richtmyer (Ref. 70), who were attempting to simulate computationally the propagation of shock waves in inviscid fluid flow without generating mesh scale numerical oscillations. von Neumann proposed that to suppress these oscillations, the difference equations could be augmented with terms reminiscent of the viscosity terms in the Navier-Stokes equations. However, the proposed artificial terms were purely numerical and did not correspond to any physical dissipative mechanism. This concept has evolved so that modern implementations operate adaptively. In the more recently developed schemes, smoothing terms are made to dominate in the vicinity of discontinuities when a lack of smoothness is detected in the solution. In particular, Jameson's flux-limited artificial dissipation model has the simplicity of the artificial dissipation approach while satisfying the TVD criteria.

Subsection 6.0 gives a general description of the flux-limited approach to achieving the TVD property. Here, the particular method used in NEDANA is explained. This flux-limited dissipation approach was first studied by Jameson (Ref. 38), and modified by Yoon and Kwak (Ref. 39), and later by Deese and Agarwal (Ref. 71). It can be described easily for the scalar Eq. (C-1), and its finite-difference approximation in Eq. (C-2). Here, the numerical flux function is defined by

$$f_{j+\frac{1}{2}}^* = \tfrac{1}{2}(f_{j+1}^{n+1} + f_j^{n+1}) + \tfrac{1}{2}\varepsilon_{j+\frac{1}{2}}|a_{j+\frac{1}{2}}^{n+1}|(\phi_{j+1}^{n+1}\Delta_x q_{j+1}^{n+1} - 2\Delta_x q_j^{n+1} + \psi_j^{n+1}\Delta_x q_{j-1}^{n+1}) \quad (C-15)$$

where $\phi_{j+1}^{n+1} = \phi\left(r_{j+1}^{n+1}\right)$ and $\Psi_j^{n+1} = \Psi\left(r_j^{n+1}\right)$ are defined in Eq. (C-11). Also, $\varepsilon_{j+1/2}$ is an adjustable parameter which can be used to control the amount of artificial dissipation.

Recall from subsection C-6.0 that if oscillations are detected in the solution, the numerical flux function shown in Eq. (C-7) becomes the flux shown in Eq. (C-9). Here, oscillations cause ϕ and ψ to vanish and $f^*_{j+1/2}$ becomes

$$f^L_{j+\frac{1}{2}} = \frac{1}{2}(f^{n+1}_{i+1} + f^{n+1}_j) - \varepsilon_{j+\frac{1}{2}}|a^{n+1}_{j+\frac{1}{2}}|\Delta_x q^{n+1}_j.$$

This resembles the low-order form shown in Eq. (C-9), and it is useful to view the second term as artificial dissipation. Next, recall that if the solution is smooth, the numerical flux function in Eq. (C-7) becomes the flux shown in Eq. (C-8). Here, when q is smooth, ϕ and ψ are close to one, and $f^*_{j+1/2}$ becomes

$$f^H_{j+\frac{1}{2}} = \frac{1}{2}(f^{n+1}_{i+1} + f^{n+1}_j) + \frac{1}{2}\varepsilon_{j+\frac{1}{2}}|a^{n+1}_{j+\frac{1}{2}}|\delta^2_x\Delta_x q^{n+1}_j.$$

This resembles the high-order form shown in Eq. (C-8) since the second term is negligible in terms of truncation error; thus, f^H here and in Eq. (C-8) leads to an approximation of f_x of the same order. The second term here is used because it has been found to inhibit the odd/even decoupling of grid values that can result from the use of a central difference scheme. Finally, note that the method defined by Eqs. (C-2) and (C-15) can be shown to be TVD, provided $\varepsilon_{j+1/2} \geq 1$. The numerical flux function for Jameson's scheme takes the following form for systems of equations:

$$F^*_{i+\frac{1}{2}} = \frac{1}{2}(F^{n+1}_j + F^{n+1}_{j+1}) + D^{n+1}_{j+\frac{1}{2}} \tag{C-16}$$

where

$$D^{n+1}_{j+\frac{1}{2}} = c^n_j\left[\bar{\Psi}(\Delta_x Q^{n+1}_{j+1}, \Delta_x Q^{n+1}_j) - 2\Delta_x Q^{n+1}_j + \bar{\Psi}(\Delta_x Q^{n+1}_j, \Delta_x Q^{n+1}_{j-1})\right],$$

$$c^n_j = \frac{\varepsilon^n_{j+\frac{1}{2}}}{2} \cdot \frac{1}{2}\left[\lambda^n_j + \lambda^n_{j+1}\right], \quad \varepsilon^n_{i+\frac{1}{2}} = [\kappa_2 + \kappa_4 \max(\nu^n_j, \nu^n_{j+1})], \quad \nu^n_j = \left|\frac{p^n_{j+1} - 2p^n_j + p^n_{j-1}}{p^n_{j+1} + 2p^n_j + p^n_{j-1}}\right|.$$

Here, $\bar{\Psi}$ is defined for vectors P and Q to have components:

$$\Psi_i(P,Q) = \frac{1}{2}[\text{sign}(P_i) + \text{sign}(Q_i)]\min(|P_i|, |Q_i|).$$

Note that this is a convenient way of expressing the limiters since for the scalar case,

$$\phi^{n+1}_{j+1}\Delta_x q^{n+1}_{j+1} = \Psi(\Delta_x q^{n+1}_{j+1}, \Delta_x q^{n+1}_j) \quad \text{and} \quad \psi^{n+1}_j\Delta_x q^{n+1}_{j-1} = \Psi(\Delta_x q^{n+1}_j, \Delta_x q^{n+1}_{j-1}).$$

The other quantities in Eq. (C-16) include κ_2 and κ_4 which are adjustable dissipation parameters, and λ which is the spectral radius of the flux Jacobian $\partial F/\partial Q$. An important advantage of the present

method is that only the spectral radius of the flux Jacobian need be rederived and implemented when new thermo-chemical models or new physical phenomena such as magnetohydrodynamics are considered for inclusion in the code.

Consider the terms that comprise c_j. First, $\varepsilon_{j+1/2}$ depends on the pressure sensors, v_j^n and v_{j+1}^n. These sensors allow the dissipation to be adjusted adaptively. Specifically, they are large in the presence of high-pressure gradients and negligible in regions of a smoothly varying pressure. The influence of these variations on $\varepsilon_{j+1/2}$ is attenuated or amplified according to the value of κ_4. Also, κ_2 is a constant chosen large enough to suppress small-scale background oscillations.

This implementation of the flux-limited dissipation scheme is a componentwise application of the scalar constructions to the vector equations. However, such a generalization is not uniquely determined. For example, the quantity, $\varepsilon_{j+1/2}|a_{j+1/2}|$, appearing in the scalar development, has a natural matrix counterpart here. Yet, for ease of implementation, it is replaced by the scalar coefficient, c_j. Therefore, this is called a scalar dissipation model. The form of the numerical flux function used for the quasi-one-dimensional set of conservation equations may be found in Ref. 17.

APPENDIX D
DEFINITION OF TIME STEP

The computational time step at the cell volume J, K, L is set to be the minimum of the time steps in the individual computational directions

$$\Delta t = min(\Delta t^\xi, \Delta t^\eta, \Delta t^\zeta),$$ (D-1)

where

$$\Delta t^\xi_{J,K,L} = CFL \left[\frac{V}{\lambda_\xi}\right]_{J,K,L}$$

$$\Delta t^\eta_{J,K,L} = CFL \left[\frac{V}{\lambda_\eta}\right]_{J,K,L}$$

$$\Delta t^\zeta_{J,K,L} = CFL \left[\frac{V}{\lambda_\zeta}\right]_{J,K,L},$$ (D-2)

and CFL is the Courant-Friedrichs-Lewy number. The spectral radii are defined as

$$\lambda_{\xi J,K,L} = \left|\vec{u} \cdot \overline{\vec{\sigma_\xi}}\right|_{J,K,L} + a_{J,K,L} \left\|\overline{\vec{\sigma_\xi}}\right\|_{J,K,L}$$

$$\lambda_{\eta J,K,L} = \left|\vec{u} \cdot \overline{\vec{\sigma_\eta}}\right|_{J,K,L} + a_{J,K,L} \left\|\overline{\vec{\sigma_\eta}}\right\|_{J,K,L}$$

$$\lambda_{\zeta J,K,L} = \left|\vec{u} \cdot \overline{\vec{\sigma_\zeta}}\right|_{J,K,L} + a_{J,K,L} \left\|\overline{\vec{\sigma_\zeta}}\right\|_{J,K,L}$$ (D-3)

where

$$\overline{\vec{\sigma_\xi}}_{J,K,L} = \frac{1}{2}[\vec{\sigma_\xi}_{J+1,K,L} + \vec{\sigma_\xi}_{J,K,L}]$$

$$\overline{\vec{\sigma_\eta}}_{J,K,L} = \frac{1}{2}[\vec{\sigma_\eta}_{J,k+1,L} + \vec{\sigma_\eta}_{J,k,L}]$$

$$\overline{\vec{\sigma_\zeta}}_{J,k,L} = \frac{1}{2}[\vec{\sigma_\zeta}_{J,K,l+1} + \vec{\sigma_\zeta}_{J,K,l}].$$ (D-4)

The frozen speed of sound, a, is calculated from

$$a^2 = \gamma_f \frac{p}{\rho}$$ (D-5)

where the frozen ratio of specific heats, γ_f, is expressed as

$$\gamma_f = (1 + \beta),$$ (D-6)

where $\beta = \partial p/\partial E$. The evaluation of β is dependent on the type of nonequilibrium model employed. The current version of the NEDANA flow solver is limited to NEQPAK thermodynamic models one or two. Therefore,

$$\beta = \begin{cases} \left(\sum_{s=1}^{n_s} \rho_s C^{vs}_{v,tr}\right)^{-1} p/T, & \text{model} = 1 \\ \left(\sum_{s\neq e^-} \rho_s C^{vs}_{v,tr}\right)^{-1} (p - p_e)/T, & \text{model} = 2 \end{cases}$$ (D-7)

111

APPENDIX E
QUASI-ONE-DIMENSIONAL NOZZLE FLOW EQUATIONS

The purpose of this appendix is to derive the partial differential equations that model inviscid quasi-one-dimensional nozzle flow. The derivation proceeds by integrating the differential form of the equations over a nozzle cross section of vanishingly small width. Then, the integral is transformed in steps by applying certain assumptions. For example, it is assumed that there are no azimuthal variations in the flow. Also, for simplicity, nozzle cross sections are assumed to be circular. Finally, the required result is obtained in the limit of decreasing cross-sectional width. See Ref. 72 for more information.

To facilitate the integration of the differential form of the equations over a nozzle cross section, the full three-dimensional equation set is first expressed in the curvilinear coordinates,

$$\xi = \xi(x, y, z), \quad \eta = \eta(x, y, z), \quad \zeta = \zeta(x, y, z).$$

For convenience, the notations

$$(x, y, z) = (x_1, x_2, x_3) = \vec{x} \quad (\xi, \eta, \zeta) = (\xi_1, \xi_2, \xi_3) = \vec{\xi}$$

$$(u, v, w) = (v_1, v_2, v_3) = \vec{v} \quad (F, G, H) = (F_1, F_2, F_3)$$

are used. Here, F, G, and H are the Cartesian flux vectors defined in Eq. (46). The Jacobian of the transformation $\vec{x} \rightarrow \vec{\xi}$ is written as

$$\mathcal{J} = \det \left\{ \frac{\partial \xi_i}{\partial x_j} \right\}_{1 \leq i,j \leq 3}.$$

Following Ref. 37, the differential form of the conservation equations is written in the curvilinear coordinates as:

$$\frac{\partial \hat{Q}}{\partial t} + \frac{\partial \hat{F}}{\partial \xi} + \frac{\partial \hat{G}}{\partial \eta} + \frac{\partial \hat{H}}{\partial \zeta} = \hat{\Omega} \tag{E-1}$$

where for flows in thermo–chemical nonequilibrium

$$
\hat{Q} = \mathcal{J}^{-1}
\begin{bmatrix}
\rho_1 \\
\vdots \\
\rho_{ns} \\
E_V \\
\rho u \\
\rho v \\
\rho w \\
E
\end{bmatrix},
\qquad
\hat{F} = \mathcal{J}^{-1}
\begin{bmatrix}
\rho_1 U \\
\vdots \\
\rho_{ns} U \\
E_V U \\
\rho u U + p\partial\xi/\partial x \\
\rho v U + p\partial\xi/\partial y \\
\rho w U + p\partial\xi/\partial z \\
(E+p)U
\end{bmatrix},
$$

$$
\hat{G} = \mathcal{J}^{-1}
\begin{bmatrix}
\rho_1 V \\
\vdots \\
\rho_{ns} V \\
E_V V \\
\rho u V + p\partial\eta/\partial x \\
\rho v V + p\partial\eta/\partial y \\
\rho w V + p\partial\eta/\partial z \\
(E+p)V
\end{bmatrix},
\qquad
\hat{H} = \mathcal{J}^{-1}
\begin{bmatrix}
\rho_1 W \\
\vdots \\
\rho_{ns} W \\
E_V W \\
\rho u W + p\partial\zeta/\partial x \\
\rho v W + p\partial\zeta/\partial y \\
\rho w W + p\partial\zeta/\partial z \\
(E+p)W
\end{bmatrix},
\qquad
\hat{\Omega} = \mathcal{J}^{-1}
\begin{bmatrix}
\omega_1 \\
\vdots \\
\omega_{ns} \\
\omega_V \\
0 \\
0 \\
0 \\
0
\end{bmatrix},
$$

$$
U = \nabla\xi \cdot \vec{v}, \qquad V = \nabla\eta \cdot \vec{v}, \qquad W = \nabla\zeta \cdot \vec{v}.
$$

Here, (U, V, W) are the so-called contravariant components of velocity. For convenience, the following notation is used:

$$
(U, V, W) = (V_1, V_2, V_3) = \vec{V} \qquad \text{and} \qquad (\hat{F}, \hat{G}, \hat{H}) = (\hat{F}_1, \hat{F}_2, \hat{F}_3).
$$

Then,

$$
V_i = \sum_{j=1}^{3} v_j \frac{\partial \xi_i}{\partial x_j}, \qquad
\hat{F}_i = \mathcal{J}^{-1} \sum_{j=1}^{3} F_j \frac{\partial \xi_i}{\partial x_j}, \qquad 1 \leq i \leq 3. \tag{E-2}
$$

Now, a particular nozzle coordinate system is introduced. Let the Cartesian coordinates x, y, and z be situated so that the x-axis is aligned with the central axis of the nozzle. Then, let the curvilinear coordinates be defined so that ξ varies only along the length of the nozzle, i.e., it depends only on x. Also, within a transverse planar section, let ζ be a radial coordinate and η an azimuthal angle. In particular, note that the nozzle surface is not a $\zeta = $ constant surface. Specifically,

$$
\xi = \xi(x), \qquad \eta = -\tan^{-1}(z/y), \qquad \zeta = \sqrt{y^2 + z^2}
$$

$$
y = \zeta \cos\eta, \qquad z = -\zeta \sin\eta
$$

113

and

$$
\mathcal{J} = \det \begin{bmatrix} \dfrac{\partial \xi}{\partial x} & \dfrac{\partial \xi}{\partial y} & \dfrac{\partial \xi}{\partial z} \\[6pt] \dfrac{\partial \eta}{\partial x} & \dfrac{\partial \eta}{\partial y} & \dfrac{\partial \eta}{\partial z} \\[6pt] \dfrac{\partial \zeta}{\partial x} & \dfrac{\partial \zeta}{\partial y} & \dfrac{\partial \zeta}{\partial z} \end{bmatrix} = \det \begin{bmatrix} \xi_x & 0 & 0 \\ 0 & -\zeta^{-1}\sin\eta & -\zeta^{-1}\cos\eta \\ 0 & \cos\eta & -\sin\eta \end{bmatrix} = \xi_x \zeta^{-1}.
$$
(E-3)

The quasi-one-dimensional equations are derived by integrating the three-dimensional equations over a cross-sectional volume, V, defined by:

$$
\mathcal{V} \equiv \{(\xi,\eta,\zeta): \quad \xi_0 \le \xi \le \xi_0 + \Delta\xi, \quad 0 \le \eta \le 2\pi, \quad 0 \le \zeta \le r(\xi)\},
$$

where $\zeta = r(\xi)$ defines the nozzle surface. This leads to

$$
\int_0^{2\pi} \int_{\xi_0}^{\xi_0+\Delta\xi} \int_0^{r(\xi)} \left[\hat{Q}_t + \hat{F}_\xi + \hat{G}_\eta + \hat{H}_\zeta - \hat{\Omega} \right] d\zeta d\xi d\eta = 0.
$$
(E-4)

Now using Eqs. (E-2) and (E-3) and the lack of azimuthal variation in each F_j,

$$
\hat{G}_\eta = \frac{\partial}{\partial\eta}\left[\mathcal{J}^{-1} \sum_{j=1}^{3} F_j \frac{\partial\eta}{\partial x_j} \right] = \frac{\zeta}{\xi_x} \sum_{j=1}^{3} F_j \frac{\partial}{\partial x_j}\left(\frac{\partial\eta}{\partial\eta} \right) = 0.
$$
(E-5)

Next, for fixed η, the following is an integration over an area, say A, in a meridian plane of the nozzle. Green's theorem in the plane gives:

$$
\int_{\xi_0}^{\xi_0+\Delta\xi} \int_0^{r(\xi)} \left[\hat{F}_\xi + \hat{H}_\zeta \right] d\zeta d\xi = \int_{\partial A} \langle -\hat{H}, \hat{F} \rangle \cdot \hat{\tau} d\tau
$$
(E-6)

where ∂A denotes the boundary of the area, A, $\hat{\tau}$ denotes a unit vector tangent to ∂A with A to the left of τ, and $d\tau$ denotes an infinitesimal line element. On the edges:

$$
\xi = \xi_0 + \Delta\xi, \quad \hat{\tau} = \langle 0, 1 \rangle. \quad d\tau = d\zeta; \qquad \xi = \xi_0, \quad \hat{\tau} = \langle 0, -1 \rangle, \quad d\tau = -d\zeta;
$$

$$
\zeta = r(\xi), \quad \hat{\tau} = \frac{\langle -1, -r_\xi \rangle}{\sqrt{1+(r_\xi)^2}}. \quad d\tau = -\sqrt{1+(r_\xi)^2}d\xi; \qquad \zeta = 0, \quad \hat{\tau} = \langle 1, 0 \rangle, \quad d\tau = d\xi.
$$

Thus,

$$
\int_{\partial A} \langle -\hat{H}, \hat{F} \rangle \cdot \vec{r} \, d\tau \;=\; \int_0^{r(\xi_0+\Delta\xi)} \langle -\hat{H}, \hat{F} \rangle \Big|_{\xi=\xi_0+\Delta\xi} \cdot \langle 0,1 \rangle d\zeta + \int_{\xi_0+\Delta\xi}^{\xi_0} \langle -\hat{H}, \hat{F} \rangle \Big|_{\zeta=r(\xi)} \cdot \langle 1, r_\xi \rangle d\xi
$$

$$
+ \int_{r(\xi_0)}^0 \langle -\hat{H}, \hat{F} \rangle \Big|_{\xi=\xi_0} \cdot \langle 0,1 \rangle d\zeta + \int_{\xi_0}^{\xi_0+\Delta\xi} \langle -\hat{H}, \hat{F} \rangle \Big|_{\zeta=0} \cdot \langle 1,0 \rangle d\xi
$$

$$
= \int_0^{r(\xi_0+\Delta\xi)} \hat{F} \Big|_{\xi=\xi_0+\Delta\xi} d\zeta + \int_{\xi_0}^{\xi_0+\Delta\xi} \left[-r_\xi \hat{F} + \hat{H} \right] \Big|_{\zeta=r(\xi)} d\xi
$$

$$
- \int_0^{r(\xi_0)} \hat{F} \Big|_{\xi=\xi_0} d\zeta - \int_{\xi_0}^{\xi_0+\Delta\xi} \hat{H} \Big|_{\zeta=0} d\xi. \tag{E-7}
$$

The last term vanishes since by Eq. (E-3),

$$
\hat{H} \Big|_{\zeta=0} = \mathcal{J}^{-1} \sum_{j=1}^3 F_j \frac{\partial \zeta}{\partial x_j} \Big|_{\zeta=0} = \frac{\zeta}{\xi_x} \sum_{j=1}^3 F_j \frac{\partial \zeta}{\partial x_j} \Big|_{\zeta=0} = 0. \tag{E-8}
$$

Next, for the second term on the right side of Eq. (E-7), it will be shown that

$$
-r_\xi \hat{F} + \hat{H} \Big|_{\zeta=r} = \frac{\zeta}{\xi_x}
\begin{bmatrix}
\rho_1(-r_\xi U + W) \\
\vdots \\
\rho_{ns}(-r_\xi U + W) \\
E_V(-r_\xi U + W) \\
\rho u(-r_\xi U + W) - p r_\xi \xi_x \\
\rho v(-r_\xi U + W) + p \cos \eta \\
\rho w(-r_\xi U + W) - p \sin \eta \\
(E+p)(-r_\xi U + W)
\end{bmatrix}_{\zeta=r}
=
\begin{bmatrix}
0 \\
\vdots \\
0 \\
0 \\
-r p r_\xi \\
r \xi_x^{-1} p \cos \eta \\
-r \xi_x^{-1} p \sin \eta \\
0
\end{bmatrix}. \tag{E-9}
$$

The first equality here follows from Eq. (E-3) and the definition of $\hat{F}$ and $\hat{H}$. Also, the fact that $(-r_\xi U + W)$ is zero at the nozzle surface, where $\zeta = r(\xi)$, can be determined by applying a tangent flow boundary condition. For this, note that the nozzle surface is represented by $f = \zeta - r(\xi) = 0$. Therefore, the outwardly directed unit normal is:

$$
\hat{n} = \frac{\nabla f}{\|\nabla f\|} = \frac{\langle -r_\xi \xi_x, \cos \eta, -\sin \eta \rangle}{\sqrt{(r_\xi \xi_x)^2 + 1}}.
$$

Also, the contravariant velocity components are given by

$$
\begin{aligned}
U &= \vec{v} \cdot \nabla \xi &&= u\xi_x \\
V &= \vec{v} \cdot \nabla \eta &&= -\zeta^{-1}(v \sin \eta + w \cos \eta) \\
W &= \vec{v} \cdot \nabla \zeta &&= v \cos \eta - w \sin \eta.
\end{aligned}
$$

Thus, the vanishing of the normal component of velocity at the nozzle surface means that:

$$
0 = \vec{v} \cdot \hat{n} = \frac{-u r_\xi \xi_x + v \cos \eta - w \sin \eta}{\sqrt{(r_\xi \xi_x)^2 + 1}} = \frac{-r_\xi U + W}{\sqrt{(r_\xi \xi_x)^2 + 1}} = 0.
$$

Now Eq. (E-9) follows from this formula. Finally, for the first and third terms in Eq. (E-7), note that by Eq. (E-3) and the fact that ξ is a function only of x,

$$
\hat{F} = \mathcal{J}^{-1} \sum_{j=1}^{3} F_j \frac{\partial \xi}{\partial x_j} = \frac{\zeta}{\xi_x} F \xi_x = \zeta F. \tag{E-10}
$$

Combining Eqs. (E-4) – (E-10) and making use of Eq. (E-3) gives:

$$
0 = \int_0^{2\pi} \left\{ \int_{\xi_0}^{\xi_0 + \Delta\xi} \left[\int_0^{r(\xi)} \frac{\zeta}{\xi_x} [Q_t - \Omega] d\zeta \right] d\xi + \int_0^{r(\xi_0 + \Delta\xi)} \zeta \, F|_{\xi = \xi_0 + \Delta\xi} \, d\zeta \right.
$$

$$
\left. - \int_0^{r(\xi_0)} \zeta \, F|_{\xi = \xi_0} \, d\zeta + \int_{\xi_0}^{\xi_0 + \Delta\xi} \begin{bmatrix} 0 \\ \vdots \\ 0 \\ 0 \\ -r p r_\xi \\ r \xi_x^{-1} p \cos \eta \\ -r \xi_x^{-1} p \sin \eta \\ 0 \end{bmatrix} d\xi \right\} d\eta.
$$

According to the azimuthal independence of Q, F and Ω,

$$
0 = 2\pi \int_{\xi_0}^{\xi_0 + \Delta\xi} \left[\int_0^{r(\xi)} \frac{\zeta}{\xi_x} [Q_t - \Omega] d\zeta \right] d\xi + 2\pi \int_0^{r(\xi_0 + \Delta\xi)} \zeta \, F|_{\xi = \xi_0 + \Delta\xi} \, d\zeta
$$

$$
- 2\pi \int_0^{r(\xi_0)} \zeta \, F|_{\xi = \xi_0} \, d\zeta + 2\pi \int_{\xi_0}^{\xi_0 + \Delta\xi} \begin{bmatrix} 0 \\ \vdots \\ 0 \\ 0 \\ -r p r_\xi \\ 0 \\ 0 \\ 0 \end{bmatrix} d\xi.
$$

Observe that certain components vanish in the last term since $\int_0^{2\pi} \cos \eta \, d\eta = \int_0^{2\pi} \sin \eta \, d\eta = 0$. Next, this equation is transformed by applying the following mean-value theorem (Ref. 73). Suppose that f and g are integrable on a set, S, where $g \geq 0$. Then, there is an average value, $\bar{f}$, between $\min_S f$ and $\max_S f$, such that

$$\int_S f(\zeta) g(\zeta) d\zeta = \bar{f} \int_S g(\zeta) d\zeta.$$

This result can be applied to the above equation componentwise. For this, define the area function,

$$A(\xi) = 2\pi \int_0^{r(\xi)} \zeta \, d\zeta \quad \text{so that} \quad A_\xi = 2\pi r r_\xi.$$

Letting $A(\xi)$ play the role of $\int g(\zeta) d\zeta$ in the above mean-value theorem gives:

$$0 = \int_{\xi_0}^{\xi_0 + \Delta \xi} \left[\left(\frac{A}{\xi_x} \bar{Q} \right)_t - \left(\frac{A}{\xi_r} \bar{\Omega} \right) \right] d\xi + (A\bar{F})|_{\xi = \xi_0 + \Delta \xi} - (A\bar{F})|_{\xi = \xi_0} + \int_{\xi_0}^{\xi_0 + \Delta \xi} \begin{bmatrix} 0 \\ \vdots \\ 0 \\ 0 \\ -A_\xi p \\ 0 \\ 0 \\ 0 \end{bmatrix} d\xi$$

where $\bar{Q}$, $\bar{F}$ and $\bar{\Omega}$ here represent average values over a given cross section. Dividing by $\Delta \xi$, and taking the limit as $\Delta \xi \to 0$ leads to:

$$\left(\xi_x^{-1} A \bar{Q} \right)_t + (A\bar{F})_\xi = \left(\xi_x^{-1} A \bar{\Omega} \right) + \begin{bmatrix} 0 \\ \vdots \\ 0 \\ 0 \\ A_\xi p \\ 0 \\ 0 \\ 0 \end{bmatrix}.$$

117

Since the equations involving ρv and ρw are decoupled from the others, the nozzle flow equations are taken as

$$
\left(AJ^{-1} \begin{bmatrix} \rho_1 \\ \vdots \\ \rho_{ns} \\ E_V \\ \rho u \\ E \end{bmatrix} \right)_t + \left(AJ^{-1} \begin{bmatrix} \rho_1 u\xi_x \\ \vdots \\ \rho_{ns} u\xi_x \\ E_V u\xi_x \\ (\rho u^2 + p)\xi_x \\ (E + p)u\xi_r \end{bmatrix} \right)_\xi = \begin{bmatrix} AJ^{-1}\dot{w}_1 \\ \vdots \\ AJ^{-1}\dot{w}_{ns} \\ AJ^{-1}\dot{w}_V \\ A_\xi p \\ 0 \end{bmatrix}
$$

where $J = \xi_x$ is the Jacobian of the transformation $x \to \xi$. Observe that by using the fact, $J^{-1}\xi_x = 1$, certain terms above can be cancelled. However, this form is retained to parallel the three-dimensional case in Eq. (E-1). The finite–volume form of the equations is easily obtained by taking $J^{-1}A$ as the volume of the corresponding cell (Ref. 37). Finally, note that setting $A = 1$ here gives the equation set for a shock-tube problem.

118

APPENDIX F
THE NONEQUILIBRIUM SOURCE JACOBIAN

F-1.0 DEFINITION OF SOURCE JACOBIAN

The numerical scheme is based on the linearization of the nonequilibrium flux vector. The vector of conserved variables, Q, and the nonequilibrium source vector, Ω, for the NEDANA flow solver are defined as follows

$$Q = \begin{pmatrix} \rho_1 \\ \vdots \\ \rho_{ns} \\ E_{N1} \\ \vdots \\ E_{Nne} \\ \rho u \\ \rho v \\ \rho u' \\ E \end{pmatrix}, \quad \Omega = \begin{pmatrix} \omega_1 \\ \vdots \\ \omega_{ns} \\ \omega_{N1} \\ \vdots \\ \omega_{Nne} \\ 0 \\ 0 \\ 0 \\ 0 \end{pmatrix}. \tag{F-1}$$

The chemical source terms, ω_r, are the production of species s in units $kg/(m^3 s)$. The nonequilibrium energy sources, ω_{N_i}, are the production of energy i in units $J/(m^3 s)$. The nonequilibrium source vector is linearized as follows:

$$\Omega^{n+1} = \Omega^n + Z^n (\delta Q^n) + O(\Delta t^2), \tag{F-2}$$

where Z^n is the Jacobian of Ω^n with respect to Q^n, and $\delta Q^n = Q^{n+1} - Q^n$. The matrix, Z, has the form

$$Z = \frac{\partial \Omega}{\partial Q} =$$

$$\begin{pmatrix}
\frac{\partial \omega_1}{\partial \rho_1} & \cdots & \frac{\partial \omega_1}{\partial \rho_{ns}} & \frac{\partial \omega_1}{\partial E_{N1}} & \cdots & \frac{\partial \omega_1}{\partial E_{Nne}} & \frac{\partial \omega_1}{\partial (\rho u)} & \frac{\partial \omega_1}{\partial (\rho v)} & \frac{\partial \omega_1}{\partial (\rho w)} & \frac{\partial \omega_1}{\partial E} \\
\vdots & \ddots & \vdots & \vdots & \ddots & \vdots & \vdots & \vdots & \vdots & \vdots \\
\frac{\partial \omega_{ns}}{\partial \rho_1} & \cdots & \frac{\partial \omega_{ns}}{\partial \rho_{ne}} & \frac{\partial \omega_{ns}}{\partial E_{N1}} & \cdots & \frac{\partial \omega_{ns}}{\partial E_{Nne}} & \frac{\partial \omega_{ns}}{\partial (\rho u)} & \frac{\partial \omega_{ns}}{\partial (\rho v)} & \frac{\partial \omega_{ns}}{\partial (\rho w)} & \frac{\partial \omega_{ns}}{\partial E} \\
\frac{\partial \omega_{N1}}{\partial \rho_1} & \cdots & \frac{\partial \omega_{N1}}{\partial \rho_{ns}} & \frac{\partial \omega_{N1}}{\partial E_{N1}} & \cdots & \frac{\partial \omega_{N1}}{\partial E_{Nne}} & \frac{\partial \omega_{N1}}{\partial (\rho u)} & \frac{\partial \omega_{N1}}{\partial (\rho v)} & \frac{\partial \omega_{N1}}{\partial (\rho w)} & \frac{\partial \omega_{N1}}{\partial E} \\
\vdots & \ddots & \vdots & \vdots & \ddots & \vdots & \vdots & \vdots & \vdots & \vdots \\
\frac{\partial \omega_{Nne}}{\partial \rho_1} & \cdots & \frac{\partial \omega_{Nne}}{\partial \rho_{n-}} & \frac{\partial \omega_{Nne}}{\partial E_{N1}} & \cdots & \frac{\partial \omega_{Nne}}{\partial E_{Nne}} & \frac{\partial \omega_{Nne}}{\partial (\rho u)} & \frac{\partial \omega_{Nne}}{\partial (\rho v)} & \frac{\partial \omega_{Nne}}{\partial (\rho w)} & \frac{\partial \omega_{Nne}}{\partial E} \\
0 & \cdots & 0 & 0 & \cdots & 0 & 0 & 0 & 0 & 0 \\
0 & \cdots & 0 & 0 & \cdots & 0 & 0 & 0 & 0 & 0 \\
0 & \cdots & 0 & 0 & \cdots & 0 & 0 & 0 & 0 & 0 \\
0 & \cdots & 0 & 0 & \cdots & 0 & 0 & 0 & 0 & 0
\end{pmatrix}. \tag{F-3}$$

The scope of the current flow solver is to use full finite-rate chemistry with a two-temperature thermal model. In this model, the translational and rotational energies are assumed to be in equilibrium with one another at the temperature, T. The vibrational energy is allowed to be characterized by a separate temperature T_v. In the case of ionization or electronic excitation, the electron temperature, T_e, is assumed to be in equilibrium with the vibrational temperature at the temperature, T_v. The nonequilibrium energy modes of all species are characterized by a single temperature. Therefore, the current scheme has only one nonequilibrium energy, E_V. This energy contains the vibrational, electron, and electronic energies of all species. The NEDANA flow solver employs NEQPAK to provide the nonequilibrium source terms and their derivatives. The adaptation of NEQPAK to the development of the sources and their derivatives will now be discussed.

F-2.0 DERIVATION OF CHEMICAL JACOBIANS

Define:

$$\gamma_s = \frac{\rho_s}{\mathcal{M}_s},$$ (F-4)

$$\gamma = \sum_{s=1}^{ns} \frac{\rho_s}{\mathcal{M}_s}.$$ (F-5)

$$\rho = \sum_{s=1}^{ns} \rho_s,$$ (F-6)

$$\mathcal{M} = \sum_{s=1}^{ns} \frac{\gamma_s}{\gamma} \mathcal{M}_s.$$ (F-7)

$$Y_s = \frac{\rho_s}{\rho},$$ (F-8)

$$C_{v,tr} = \sum_{s=1}^{ns} Y_s C_{v,tr}^s,$$ (F-9)

$$C_{v,V} = \sum_{s=1}^{ns} Y_s C_{v,V}^s,$$ (F-10)

where γ_s is the concentration of species s in $kgmole/m^3$; γ is the concentration of the mixture in $kgmole/m^3$; ρ_s is the density of species s in kg/m^3; ρ is the mixture of the density in kg/m^3; $\mathcal{M}_s$ is the molecular weight of species s in $kg/kgmole$; $\mathcal{M}$ is the molecular weight of the mixture in $kg/kmole$, and Y_s is the mass fraction of species s. $C_{v,tr}$ is the specific heat at constant volume dependent on T. $C_{v,V}$ is the specific heat at constant volume dependent on T_V. Also, define a general temperature array such that

$$T_m = T_m(T, T_V), \quad m = 1, ntype.$$ (F-11)

For example, with *ntype* = 2,

$$T_1 = T$$
$$T_2 = T^{1-\alpha} T_V^\alpha$$ (F-12)

where $0 \le \alpha \le 1$.

NEQPAK provides $\bar{w}_s$ ($kmole/m^3/sec$) which is a function of γ_i and T_m. NEQPAK also provides $\frac{\partial \bar{w}_i}{\partial \gamma_j}\big|_{\gamma_s \neq j, T_m}$, and $\frac{\partial \bar{w}_i}{\partial T_m}\big|_{\gamma_s, T_n \neq m}$, where the vertical bars denote the partial derivatives are evaluated holding the subscripted quantites constant. The task now is to write these quantities in terms that the NEDANA flow solver requires. The chemical sources become

$$w_i = \mathcal{M}_i \bar{w}_i.$$ (F-13)

The total derivative of w_i becomes

$$
\begin{aligned}
dw_i &= \mathcal{M}_i \, d\bar{w}_i \\
&= \mathcal{M}_i \Bigg\{ \sum_{j=1}^{ns} \frac{\partial \bar{w}_i}{\partial \gamma_j}\bigg|_{\gamma_s \neq j, T_m} d\gamma_j \\
&\quad + \sum_{m=1}^{ntype} \frac{\partial \bar{w}_i}{\partial T_m}\bigg|_{\gamma_s, T_n \neq m} \frac{\partial T_m}{\partial T}\bigg|_{T_V} dT \\
&\quad + \sum_{m=1}^{ntype} \frac{\partial \bar{w}_i}{\partial T_m}\bigg|_{\gamma_s, T_n \neq m} \frac{\partial T_m}{\partial T_V}\bigg|_T dT_V \Bigg\}.
\end{aligned}
$$ (F-14)

The total derivatives $d\gamma_j$, dT, and dT_V must now be expressed in terms of the conservative variables, Q. First,

$$d\gamma_j = \frac{1}{\mathcal{M}_j} d\rho_j.$$ (F-15)

Now, consider dT. The total energy of the mixture is

$$E = \frac{1}{2}\rho(u^2 + v^2 + w^2) + E_I + E_V.$$ (F-16)

The internal energy dependent on T is

$$E_I = \rho e_I,$$ (F-17)

121

where

$$\epsilon_I = \sum_{i=1}^{ns} Y_i\, e_{I,i} \tag{F-18}$$

and

$$e_{I,i} = \int_{T_{ref}}^{T} C_{v,tr}^i (T')dT' + e_i^0, \tag{F-19}$$

where $C_{v,tr}^i$ and e_i^0 are the specific heat at constant volume of species i due to T, and the energy of formation of species i, respectively. Then,

$$de_I = \sum_{i=1}^{ns} dY_i\, e_{I,i} + \sum_{i=1}^{ns} Y_i\, de_{I,i}, \tag{F-20}$$

where

$$de_{I,i} = C_{v,tr}^i\, dT \tag{F-21}$$

Thus,

$$dT = \frac{de_I - \sum_{i=1}^{ns} dY_i\, e_{I,i}}{\sum_{i=1}^{ns} Y_i\, C_{v,tr}^i} = \frac{de_I - \sum_{i=1}^{ns} dY_i\, e_{I,i}}{C_{v,tr}}. \tag{F-22}$$

Now,

$$dY_i = \frac{d\rho_i - Y_i\, d\rho}{\rho}. \tag{F-23}$$

and

$$d\rho = \sum_{i=1}^{ns} d\rho_i. \tag{F-24}$$

Now, writing E in terms of Q,

$$E = \frac{(\rho u)^2 + (\rho v)^2 + (\rho w)^2}{2\rho} + E_I + E_V, \tag{F-25}$$

and

$$dE = u\,d(\rho u) + v\,d(\rho v) + w\,d(\rho w) + \rho de_I + d(E_V)$$
$$+ [e_I - \frac{1}{2}(u^2 + v^2 + w^2)]d\rho. \tag{F-26}$$

122

Using the fact that

$$e_I = e - \frac{1}{2}(u^2 + v^2 + w^2) - e_V,$$ (F-27)

substitution gives

$$dE = ud(\rho u) + vd(\rho v) + wd(\rho w) + \rho de_I + d(E_V)$$
$$+ [e - (u^2 + v^2 + w^2) - e_V]d\rho.$$ (F-28)

Rearranging,

$$de_I = \frac{1}{\rho}\Big\{ d(E) - ud(\rho u) - vd(\rho v) - wd(\rho w) - d(E_V)$$
$$- [e - (u^2 + v^2 + w^2) - e_V]d\rho \Big\}.$$ (F-29)

Now,

$$dT = \frac{1}{\rho C_{v,tr}}\Big\{ d(E) - ud(\rho u) - vd(\rho v) - wd(\rho w) - d(E_V)$$
$$- [e - (u^2 + v^2 + w^2) - e_V]d\rho - \sum_{i=1}^{ns} e_{I,i}[d\rho_i - Y_i d\rho] \Big\}$$ (F-30)

leading to

$$dT = \frac{1}{\rho C_{v,tr}}\Big\{ d(E) - ud(\rho u) - vd(\rho v) - wd(\rho w) - d(E_V)$$
$$+ \sum_{i=1}^{ns}[\frac{1}{2}(u^2 + v^2 + w^2) - e_{I,i}]d\rho_i \Big\}$$ (F-31)

Now, to express dT_V in terms of the conservative variables Q. The vibrational/electronic energy is

$$E_V = \rho e_V,$$ (F-32)

where

$$e_V = \sum_{i=1}^{ns} Y_i e_{V,i}$$ (F-33)

and

$$e_{V,i} = \int_{T_{ref}}^{T_V} C_{v,V}^i(T')dT'.$$ (F-34)

where $C_{v,V}^i$ is the specific heat at constant volume of species i due to T_V. Then,

$$dc_V = \sum_{i=1}^{ns} dY_i \, e_{V,i} + \sum_{i=1}^{ns} Y_i \, de_{V,i}. \tag{F-35}$$

Thus,

$$dT_V = \frac{de_V - \sum_{i=1}^{ns} dY_i \, e_{V,i}}{\sum_{i=1}^{ns} Y_i C_{v,V}^i} = \frac{de_V - \sum_{i=1}^{ns} dY_i \, e_{V,i}}{C_{v,V}}. \tag{F-36}$$

But also,

$$d(e_V) = \frac{dE_V - e_V \, d\rho}{\rho}. \tag{F-37}$$

Therefore,

$$dT_V = \frac{1}{\rho C_{v,V}} \left\{ d(E_V) - \sum_{i=1}^{ns} e_{V,i} \, d\rho_i \right\}. \tag{F-38}$$

Now, define

$$\left. \frac{\partial \tilde{\omega}_i}{\partial T} \right|_{\gamma, T_V} = \sum_{m=1}^{ntype} \left. \frac{\partial \tilde{\omega}_i}{\partial T_m} \right|_{\gamma_s, T_n \neq m} \left. \frac{\partial T_m}{\partial T} \right|_{T_V}$$

$$\left. \frac{\partial \tilde{\omega}_i}{\partial T_V} \right|_{\gamma, T} = \sum_{m=1}^{ntype} \left. \frac{\partial \tilde{\omega}_i}{\partial T_m} \right|_{\gamma_s, T_n \neq m} \left. \frac{\partial T_m}{\partial T_V} \right|_{T}. \tag{F-39}$$

Employing Eqs. (F-15), (F-31), and (F-38), Eq. (F-14) can now be written in terms of derivatives of the conservative variables.

$$dw_i = \frac{\mathcal{M}_i}{\rho C_{v,tr}} \left. \frac{\partial \tilde{\omega}_i}{\partial T} \right|_{\gamma, T_V} [d(E) - u\,d(\rho u) - v\,d(\rho v) - w\,d(\rho w)]$$

$$+ \left[\frac{\mathcal{M}_i}{\rho C_{v,V}} \left. \frac{\partial \tilde{\omega}_i}{\partial T_V} \right|_{\gamma, T} - \frac{\mathcal{M}_i}{\rho C_{v,tr}} \left. \frac{\partial \tilde{\omega}_i}{\partial T} \right|_{\gamma, T_V} \right] d(E_V)$$

$$+ \sum_{j=1}^{ns} \Bigg\{ \left. \frac{\partial \tilde{\omega}_i}{\partial \gamma_j} \right|_{\gamma_s \neq j, T_m} \frac{\mathcal{M}_i}{\mathcal{M}_j}$$

$$+ \frac{\mathcal{M}_i}{\rho C_{v,tr}} \left[\frac{1}{2}(u^2 + v^2 + w^2) - e_{I,j} \right] \left. \frac{\partial \tilde{\omega}_i}{\partial T} \right|_{\gamma, T_V} - \frac{\mathcal{M}_i}{\rho C_{v,V}} e_{V,j} \left. \frac{\partial \tilde{\omega}_i}{\partial T_V} \right|_{\gamma, T} \Bigg\} d\rho_j \tag{F-40}$$

The chemical source Jacobians can now be obtained by taking partial derivatives of the above equation.

$$\left. \frac{\partial \omega_i}{\partial \rho_j} \right|_{\rho_{k \neq j}, \rho u, \rho v, \rho w, E_V, E} = + \frac{\mathcal{M}_i}{\mathcal{M}_j} \left. \frac{\partial \tilde{\omega}_i}{\partial \gamma_j} \right|_{\gamma_s \neq j, T_m}$$

$$+ \frac{\mathcal{M}_i}{\rho C_{v,tr}} \left[\frac{1}{2}(u^2 + v^2 + w^2) - e_{I,j} \right] \left. \frac{\partial \tilde{\omega}_i}{\partial T} \right|_{\gamma, T_V}$$

$$- \frac{\mathcal{M}_i}{\rho C_{v,V}} e_{V,j} \left. \frac{\partial \tilde{\omega}_i}{\partial T_V} \right|_{\gamma, T} \tag{F-41}$$

$$\left.\frac{\partial \omega_i}{\partial E_V}\right|_{\rho,\rho u,\rho v,\rho w,E} = -\frac{\mathcal{M}_i}{\rho C_{v,tr}}\left.\frac{\partial \tilde{\omega}_i}{\partial T}\right|_{\gamma,T_V}$$
$$+\frac{\mathcal{M}_i}{\rho C_v,V}\left.\frac{\partial \tilde{\omega}_i}{\partial T_V}\right|_{\gamma,T} \tag{F-42}$$

$$\left.\frac{\partial \omega_i}{\partial(\rho u)}\right|_{\rho,\rho v,\rho w,E_V,E} = -u\frac{\mathcal{M}_i}{\rho C_{v,tr}}\left.\frac{\partial \tilde{\omega}_i}{\partial T}\right|_{\gamma,T_V} \tag{F-43}$$

$$\left.\frac{\partial \omega_i}{\partial(\rho v)}\right|_{\rho,\rho u,\rho w,E_V,E} = -v\frac{\mathcal{M}_i}{\rho C_{v,tr}}\left.\frac{\partial \tilde{\omega}_i}{\partial T}\right|_{\gamma,T_V} \tag{F-44}$$

$$\left.\frac{\partial \omega_i}{\partial(\rho w)}\right|_{\rho,\rho u,\rho v,E_V,E} = -w\frac{\mathcal{M}_i}{\rho C_{v,tr}}\left.\frac{\partial \tilde{\omega}_i}{\partial T}\right|_{\gamma,T_V} \tag{F-45}$$

$$\left.\frac{\partial \omega_i}{\partial E}\right|_{\rho,\rho u,\rho v,\rho w,E_V} = +\frac{\mathcal{M}_i}{\rho C_{v,tr}}\left.\frac{\partial \tilde{\omega}_i}{\partial T}\right|_{\gamma,T_V} \tag{F-46}$$

F-3.0 DERIVATION OF VIBRATIONAL/ELECTRONIC JACOBIANS

The vibrational/electronic source term for the two-temperature model where $T_V = T_v = T_e$ has the form

$$\omega_V = \omega_{V_r} + \omega_{V_c} + \omega_{V_e} - p_e \, \tilde{\nabla} \cdot \vec{u}. \tag{F-47}$$

The first term, ω_{V_r}, is the Landau-Teller relaxation term between T and T_v. NEQPAK returns this term in $J/m^3/s$, as well as the following derivatives: $\left.\frac{\partial \omega_{V_r}}{\partial \eta_j}\right|_{\gamma_s \neq j, T, T_V}$; $\left.\frac{\partial \omega_{V_r}}{\partial T}\right|_{\gamma,T_V}$; $\left.\frac{\partial \omega_{V_r}}{\partial T_V}\right|_{\gamma,T}$. The third term, ω_{V_e}, is the relaxation term between T and T_e. NEQPAK provides this term in $J/(m^3 s)$, as well as the following derivatives: $\left.\frac{\partial \omega_{V_e}}{\partial \eta_j}\right|_{\gamma_s \neq j, T, T_V}$; $\left.\frac{\partial \omega_{V_e}}{\partial T}\right|_{\gamma,T_V}$; $\left.\frac{\partial \omega_{V_e}}{\partial T_V}\right|_{\gamma,T}$. The fourth term, $p_e \vec{\nabla} \cdot \vec{u}$, is the electron pressure gradient term. This term is not provided by NEQPAK. This term is treated as a viscous term and does not appear in the Jacobian formulation. The second term, ω_{V_c}, is the production or destruction of E_V due to chemical reactions. This term is currently not provided by NEQPAK. Instead, due to its simple form, it is developed in the NEDANA flow solver. The non-preferential form is

$$\omega_{V_c} = \sum_{i=1}^{ns} \tilde{\omega}_i \tilde{e}_{V,i}. \tag{F-48}$$

or

$$\omega_{V_c} = \sum_{i=1}^{ns} \omega_i e_{V,i}.$$

(F-49)

Using Eq. (F-39), the derivatives are easily formed to yield

$$\left.\frac{\partial \omega_{V_c}}{\partial \gamma_j}\right|_{\gamma_s \neq j, T, T_V} = \sum_{i=1}^{ns} \left.\frac{\partial \tilde{\omega}_i}{\partial \gamma_j}\right|_{\gamma_s \neq j, T_m} \tilde{e}_{V,i}$$

(F-50)

$$\left.\frac{\partial \omega_{V_c}}{\partial T}\right|_{\gamma, T_V} = \sum_{i=1}^{ns} \left.\frac{\partial \tilde{\omega}_i}{\partial T}\right|_{\gamma, T_V} \tilde{e}_{V,i}$$

(F-51)

$$\left.\frac{\partial \omega_{V_c}}{\partial T_V}\right|_{\gamma, T} = \sum_{i=1}^{ns} \left[\left.\frac{\partial \tilde{\omega}_i}{\partial T_V}\right|_{\gamma, T} \tilde{e}_{V,i} + \omega_i C_{v,V}^i \right].$$

(F-52)

The derivatives of the total source term can now be formed by combining the individual terms to yield

$$\left.\frac{\partial \omega_V}{\partial \gamma_j}\right|_{\gamma_s \neq j, T, T_V} = \left.\frac{\partial \omega_{V_v}}{\partial \gamma_j}\right|_{\gamma_s \neq j, T, T_V} + \left.\frac{\partial \omega_{V_e}}{\partial \gamma_j}\right|_{\gamma_s \neq j, T, T_V} + \left.\frac{\partial \omega_{V_c}}{\partial \gamma_j}\right|_{\gamma_s \neq j, T, T_V}$$

(F-53)

$$\left.\frac{\partial \omega_V}{\partial T}\right|_{\gamma, T_V} = \left.\frac{\partial \omega_{V_v}}{\partial T}\right|_{\gamma, T_V} + \left.\frac{\partial \omega_{V_e}}{\partial T}\right|_{\gamma, T_V} + \left.\frac{\partial \omega_{V_c}}{\partial T}\right|_{\gamma, T_V}$$

(F-54)

$$\left.\frac{\partial \omega_V}{\partial T_V}\right|_{\gamma, T} = \left.\frac{\partial \omega_{V_e}}{\partial T_V}\right|_{\gamma, T} + \left.\frac{\partial \omega_{V_c}}{\partial T_V}\right|_{\gamma, T} + \left.\frac{\partial \omega_{V_v}}{\partial T_V}\right|_{\gamma, T}.$$

(F-55)

The total derivative of ω_V becomes

$$d\omega_V = \sum_{j=1}^{ns} \left.\frac{\partial \omega_V}{\partial \gamma_j}\right|_{\gamma_s \neq j, T, T_V} d\gamma_j + \left.\frac{\partial \omega_V}{\partial T}\right|_{\gamma, T_V} dT$$
$$+ \left.\frac{\partial \omega_V}{\partial T_V}\right|_{\gamma, T} dT_V$$

(F-56)

The total derivatives $d\gamma$, dT, and dT_V were defined in Eqs. (F-15), (F-31), and (F-38), respectively. Using these definitions of the total derivatives, Eq. (F-56) becomes

$$dw_V = \frac{1}{\rho C_{v,tr}} \left. \frac{\partial \omega_V}{\partial T} \right|_{\gamma,T_V} \left[d(E) - u d(\rho u) - v d(\rho v) - w d(\rho w) \right]$$

$$+ \left[\frac{1}{\rho C_{v,V}} \left. \frac{\partial \omega_V}{\partial T_V} \right|_{\gamma,T} - \frac{1}{\rho C_{v,tr}} \left. \frac{\partial \omega_V}{\partial T} \right|_{\gamma,T_V} \right] d(E_V)$$

$$+ \sum_{j=1}^{ns} \left\{ \frac{1}{\mathcal{M}_j} \left. \frac{\partial \omega_V}{\partial \gamma_j} \right|_{\gamma_i \neq j, T, T_V} \right.$$

$$\left. + \frac{1}{\rho C_{v,tr}} \left[\frac{1}{2}(u^2 + v^2 + w^2) - e_{I,j} \right] \left. \frac{\partial \omega_V}{\partial T} \right|_{\gamma,T_V} - \frac{e_{V,j}}{\rho C_{v,V}} \left. \frac{\partial \omega_V}{\partial T_V} \right|_{\gamma,T} \right\} d\rho_j \quad \text{(F-57)}$$

The vibrational/electronic source Jacobians can now be obtained by taking partial derivatives of the above equation.

$$\left. \frac{\partial \omega_V}{\partial \rho_j} \right|_{\rho_{k \neq j}, \rho u, \rho v, \rho w, E_V, E} = + \frac{1}{\mathcal{M}_j} \left. \frac{\partial \omega_V}{\partial \gamma_j} \right|_{\gamma_i \neq j, T, T_V}$$

$$+ \frac{1}{\rho C_{v,tr}} \left[\frac{1}{2}(u^2 + v^2 + w^2) - e_{I,j} \right] \left. \frac{\partial \omega_V}{\partial T} \right|_{\gamma,T_V}$$

$$- \frac{e_{V,j}}{\rho C_{v,V}} \left. \frac{\partial \omega_V}{\partial T_V} \right|_{\gamma,T} \quad \text{(F-58)}$$

$$\left. \frac{\partial \omega_V}{\partial E_V} \right|_{\rho, \rho u, \rho v, \rho w, E} = - \frac{1}{\rho C_{v,tr}} \left. \frac{\partial \omega_V}{\partial T} \right|_{\gamma,T_V}$$

$$+ \frac{1}{\rho C_{v,V}} \left. \frac{\partial \omega_V}{\partial T_V} \right|_{\gamma,T} \quad \text{(F-59)}$$

$$\left. \frac{\partial \omega_V}{\partial (\rho u)} \right|_{\rho, \rho v, \rho w, E_V, E} = \frac{-u}{\rho C_{v,tr}} \left. \frac{\partial \omega_V}{\partial T} \right|_{\gamma,T_V} \quad \text{(F-60)}$$

$$\left. \frac{\partial \omega_V}{\partial (\rho v)} \right|_{\rho, \rho u, \rho w, E_V, E} = \frac{-v}{\rho C_{v,tr}} \left. \frac{\partial \omega_V}{\partial T} \right|_{\gamma,T_V} \quad \text{(F-61)}$$

$$\left. \frac{\partial \omega_V}{\partial (\rho w)} \right|_{\rho, \rho u, \rho v, E_V, E} = \frac{-w}{\rho C_{v,tr}} \left. \frac{\partial \omega_V}{\partial T} \right|_{\gamma,T_V} \quad \text{(F-62)}$$

$$\left. \frac{\partial \omega_V}{\partial E} \right|_{\rho, \rho u, \rho v, \rho w, E_V} = + \frac{1}{\rho C_{v,tr}} \left. \frac{\partial \omega_V}{\partial T} \right|_{\gamma,T_V} \quad \text{(F-63)}$$

NOMENCLATURE

a	Frozen speed of sound, m/s
a	Coefficient in Eq. (13)
a	Scalar flux Jacobian
A	One-dimensional nozzle area, m^2
A	Matrix flux Jacobian
$A_{s,r}$	Millikan and White coefficient
A_r	Arrhenius coefficient, Eq. (30)
b	Diagonal matrix, $1/s$
b	Coefficient in Eq. (20)
B	Iteration matrix
B_1	Block iteration matrix
B_2	Scalar iteration matrix
B	Viscous term coefficient
B_r	Arrhenius coefficient, Eq. (30)
c	Scalar dissipation, m^3/s
C	Park's correction
C_r	Arrhenius coefficient, Eq. (30)
C_p	Specific heat at constant pressure, $J/kg\ K$
C_v	Specific heat at constant volume, $J/kg\ K$
CFL	Courant-Friedrichs-Lewy number
d	Coefficient in Eq. (23)
D	Effective diffusion coefficient, m²/s
$\mathcal{D}$	Binary diffusion coefficient, m²/s
e	Specific energy, J/kg
E	Energy per unit volume, J/m^3
f	Scalar flux function
$\vec{F}$	Numerical flux function
ΔF	Change in free energy, $J/kmole$
$\bar{F}, \bar{G}, \bar{H}$	Cartesian flux vectors

$\tilde{F}, \tilde{G}, \tilde{H} F$	Computational flux vectors
g_l	Degeneracy of lth electronic level
G	Gibbs free energy, $J/kmole$
G	Rate of gain, $kmole/m^3 s$
h	Planck constant, J/s
h	Enthalpy per unit mass, J/kg
h_s^0	Species heat of formation, J/kg
$\hat{i}_x, \hat{i}_y, \hat{i}_z$	Cartesian unit vectors
I	Identity matrix
j,k,l	Computational indices
J	Jacobian of transformation
k	Boltzmann constant, J/K
k^f	Forward reaction coefficient, $m^3/kmole$
k^r	Reverse reaction coefficient, $m^3/kmole$ or $m^6/kmole^2$
K^c	Equilibrium constant
L	Characteristic length, m
$\mathcal{L}$	Rate of loss, $kmole/m^3 s$
M	Generic molecule
M	Mach number
$\mathcal{M}$	Molecular weight, $kg/kmol$
N_A	Avogadro's number
ne	Number of nonequilibrium energies
nel	Number of electronic energy levels
nq	Number of conserved variables
nr	Number of reactions
ns	Number of species
p	Pressure, N/m^2
q	Heat conduction, W/m^2
q	Scalar conservation variable
Q	Vector of conserved variables
r	Position vector, m

r	Ratio of differences
R	Gas constant, $J/kg\ K$
Re	Reynolds number
Rn	Nose radius, m
$\mathcal{R}$	Universal gas constant, $J/kmole\ K$
R	Residual
s	Generic differences
S	Surface area, m^2
S	Matrix of eigenvectors
T	Temperature, K
T'	Integration variable, K
TV	Total variation
TVD	Total variation diminishing
$\mathcal{T}$	ln T
t	Time, s
t_{char}	Characteristic flow time, s
$\vec{u}$	Velocity vector
$\vec{u}^{d}$	Diffusion velocity vector
u,v,w	Cartesian velocities, m/s
u^d,v^d,w^d	Diffusion velocities, m/s
V	Cell volume, m^3
ω	Chemical source term, $kg/m^3/sec$
$\tilde{\omega}$	Chemical source term, $kmole/m^3/sec$
ω_N	Generic nonequilibrium energy source term, $J/m^3/sec$
x, y, z	Cartesian coordinates, m
y^+	$y\frac{\rho}{\mu}\sqrt{\frac{\mu}{\rho}\frac{\partial u}{\partial y}}$, nondimensional viscous spacing
Y	Mass fraction
Z	Partition function
α	Exponent in Park's TT_v model
α_v	Viscous relaxation parameter
β	$\partial p/\partial E$

130

γ	Concentration, $kmole/m^3$
γ_f	Frozen ratio of specific heats
ϵ	Dissipation parameter
ϵ_l	Energy of electronic state, J/kmole
ξ, η, ζ	Computational coordinates
θ	Characteristic temperature, K
κ	Thermal conductivity, $J/ms\ K$
κ_2, κ_4	Dissipation parameter
λ	Spectral radius, m^3/s
Λ	Diagonal matrix of eigenvalues
μ	Viscosity of mixture, kg/ms
$\mu_{s,r}$	Reduced mass
μ_ξ, ν_ξ	Pressure smoothness sensors
ν	Stoichiometric coefficients
ν_t	Characteristic vibrational frequency
Ω	Source vector
ρ	Density, kg/m^3
σ	Collision cross section, m^2
$\vec{\sigma}$	Directed surface area at cell face
$\overline{\vec{\sigma}}$	Directed surface area at cell center
τ	Relaxation time, s
τ_{ij}	Shear stress tensor
Φ	Flux limiter
ϕ	Flux limiter
χ	Mole fraction
ψ	Flux limiter
ψ	Dimensionless electronic energy
ω_s	Mass source of species s, $kg/m^3/s$
ω_v	Vibrational/electronic source term, $J/m^3/s$
d	Total derivative
∂	Partial derivative

$\vec{\nabla}$ | Del operator

$\nabla_x(\bullet)_j^n$ | $(\bullet)_j^n - (\bullet)_{j-1}^n$

δ | Kronecker delta

δ^r | Change in mole number

$\delta_x(\bullet)_j^n$ | $(\bullet)_{j+1/2}^n - (\bullet)_{j-1/2}^n$

$\Delta_t(\bullet)_j^n$ | $(\bullet)_j^{n+1} - (\bullet)_j^n$

$\Delta_x(\bullet)_j^n$ | $(\bullet)_{j+1}^n - (\bullet)_j^n$

Δn | Iinitial viscous spacing, m

δQ | Implicit time change in vector of conserved quantities

ΔQ | Explicit time change in vector of conserved quantities

Δt | Time step, s

$\Delta_\xi, \Delta_\eta, \Delta_\zeta$ | Differences in computational coordinates

Subscripts:

e | Electronic

f | Frozen

I | Inviscid

i, j, k | Index notation

I | Internal mode

L, R | Left, right

n, m | Summation/iteration index

0 | Stagnation/total condition

o, e | Odd/even indices

q | Generic temperature, K

r, s | Species/reaction index

r | Rotational

t | Translational

tr | Translational–rotational

v | Viscous

v | Vibrational

V | Vibrational–electronic

$v - c$	Vibration–chemistry
$v - T$	Vibration–translational
∞	Free–stream condition

Superscripts:

atm	Standard atmosphere
f	Forward rate
H	Higher order approximation
L	Lower order approximation
L, R	Left, right
n	Time level
o, e	Odd/even indices
m	Iteration level
r	Reverse rate
s	Denotes species value
v	Vibrational
*	Equilibrium, nozzle inlet, or latest value